MONITORING SUSPENDED PARTICULATE MATTER BASED ON SATELLITE-IMAGERY AND GROUND OBSERVATION

YAN XING

Ph.D

The Hong Kong Polytechnic University

2017

The Hong Kong Polytechnic University
Department of Land Surveying and Geo-Informatics

Monitoring Suspended Particulate Matter Based on Satellite-imagery and Ground Observation

Yan Xing

A thesis submitted in partial fulfilment of the requirements for the degree of Doctor of Philosophy

May 2016

CERTIFICATE OF ORIGINALITY

I hereby declare that this thesis is my own work and that, to the best of my knowledge and belief, it reproduces no material previously published or written, nor material that has been accepted for the award of any other degree or diploma, except where due acknowledgement has been made in the text.

____________________ (Signed)

Yan Xing (Name of student)

Abstract

In recent years, due to the rapid urbanization all over the world, air pollution has become a serious problem in many countries. Especially in China, rapid industrialization associated with more fossil fuel consumption has caused serious suspended particulate matter pollution, and resulted in more frequent haze days. At present, many studies have been indicating that the size and the formation mechanism have a close relationship with public health. Therefore, a good understanding of the distribution of air suspended particles with different diameters is necessary. However, there are still some limitations for different size distributions of air suspended particles retrieval by remote sensing. Thus, this thesis firstly put forward a reliable method for monitoring dust distribution (diameter less than 1 mm) with the aid of ground-based plant leaf spectral data. A back propagation (BP) neutral network model was generated using spectral response functions and integrated remote sensing data to estimate dustfall weight in the city of Beijing. Compared with actual dustfall weight, validation of the results showed a satisfactory accuracy with a low RMSE of 3.6 g/m^2. Secondly, an algorithm was developed which incorporates haze monitoring and haze aerosol optical thickness (HAOT, particulate size between 0.001μm to 10 μm) retrieval based on MODIS data. From the comparison, this method can effectively make up for MODIS AOT products deficiency about missing data under haze weather condition. Then, the fine mode fraction (FMF) is a useful tool to separate the fine mode aerosol from the total aerosol. However, the spatial view of the FMF is still limited. Therefore, a lookup table-based spectral deconvolution algorithm (LUT-SDA) was proposed. This method was validated with ground-based data and had a high accuracy compared

to the Aerosol Robotic Network (AERONET) FMF. Finally, assistant by LUT-SDA, a ground-level PM2.5 retrieval model was developed. This model had been applied to retrieval surface PM2.5 concentration over Beijing from December 2013 to June 2015 in cloud free day. The derived results ware compared with the monitoring values with $R^2 = 0.64$ and RMSE = 18.9 $\mu g/m^3$ (N = 921). This validation demonstrated that the developed model exhibits a good performance with a high accuracy.

List of publications

Journal

1. **Yan X.**, Shi W.*, Luo N., Zhao W., 2016. A new method of satellite-based haze aerosol monitoring over the North China Plain and a comparison with MODIS Collection 6 aerosol products. *Atmospheric Research*, 171:31-40.

2. **Yan X.**, Shi W.*, Zhao W., Luo N., 2015. Mapping dustfall distribution in urban areas using remote sensing and ground spectral data. *Science of the Total Environment*, 506:604-612.

3. **Yan X.**, Shi W.*, Zhao W., Luo N., 2014. Impact of aerosols and atmospheric particles on plant leaf proteins. *Atmospheric Environment*, 88:115-122.

4. **Yan X.**, Shi W.*, Zhao W., Luo N., 2014. Estimation of Protein Content in Plant Leaves using Spectral Reflectance: A Case Study in Euonymus japonica. *Analytical Letters*, 47:517-530.

5. **Yan X.**, Shi W.*, Zhao W., Luo N., 2014. Estimation of Atmospheric Dust on Plant Leaves Based on Spectral Features. *Spectroscopy Letters*, 47:536-542.

Conference

6. Shi W.*,**Yan X.**, 2014.An optimized algorithm for retrieving aerosol optical thickness over urban areas from MODIS imagery. *International Symposium on Environment and Health*, Beijing,4-5 July, 2014.

Acknowledgements

I would like to express my gratitude to all those who helped me during the PhD study.

My deepest gratitude goes first and foremost to Chair Professor Wenzhong Shi, my supervisor, for his intellectual guidance and constant encouragement. It is known that as the head of the department, he has limited time. However, no matter how busy he is, we can have face-to-face discussions when I have problems in my research. Without his patient teaching, insightful comments and illuminating instruction, the completion of this thesis would not have been possible.

I also owe a special debt of gratitude to Professor Wenji Zhao of the Capital Normal University who helped me about collection of the ground-based data. Many thanks to let me have a chance to enjoy unforgettable and meaningful field experiments in Beijing.

I would like to express my heartfelt gratitude to Professor Zhanqing Li, who led me into the world of aerosol and climate. I am also greatly indebted to the teachers at the Department of ESSIC: Dr. Jianjun Liu, Ms. Maureen Cribb and Dr. Taixia Wu.

I would like to thank all of my friends in LSGI and PolyU: Zelang Miao, Bin Wang, Zhongbin Li, Qunming Wang, Anshu Zhang, Cheng Yang, Xiaolin Zhou, Wenzheng Fan and so on. In addition, I would like to thank Beijing field experiment members: Nana Luo, Qiulin Xiong, Fantao Chen, Xiaoxia Zheng, Haofei Wang, Qianzhong Zhang and so on, who helped me a lot in the past years.

Last but not least, I thank my parents and all the other family members

for their loving consideration and great confidence for all through these years.

Table of Contents

List of Tables

List of Figures

Chapter 1

Introduction

1.1 Background

Suspended particulate matters are widely considered as a major source of atmospheric pollution, especially in urban areas, of which the morphologic structure, the size and the formation mechanism have a close relationship with public health (Figure 1.1). Therefore, monitoring suspended particles is important to the environmental control and improvement, and a good understanding of the distribution of air suspended particles with different diameters is vital.

Suspended particulate matters have a wide range of sizes, varying from 0.001 μm to 1000 μm, and different residence time from minutes to hours. Generally, particles with a diameter larger than 50 μm would gravitate to the ground quickly. As we known, particles with different sizes would have different impacts on human health. For example, particles less than 10μm result in a greater damage than other particles, and especially 2-4 μm particles have the largest deposition rate in the bronchi and bronchioles. Particles less than 1 μm have a strong scattering effect on visible lights which would decrease the atmospheric visibility. So far, with the rapid development of remote sensing techniques, the acquisition of a large-scale distribution of the suspended particulate matters has been increasingly possible. Therefore, this study aims at monitoring the airborne particles of various sizes, i.e. dustfall, haze aerosol, fine mode aerosol and PM2.5, based on remote sensing, and illustrating the potential limitations and improvements in the current literature pool.

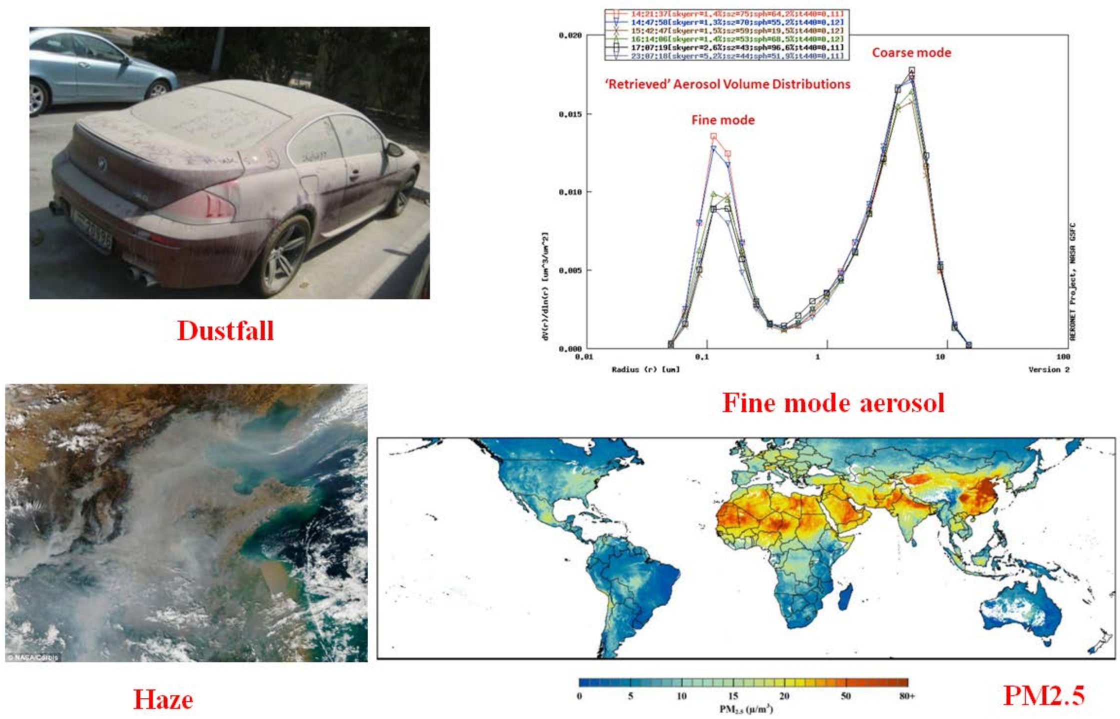

Figure 1.1: Suspended particulate matter pollution

1.1.1 Dustfall

Urban atmospheric dust contains high concentration of heavy metals and particulate matters, which are thought to be the most harmful pollution component (Rai, 2013). In addition, dust accumulation on plant leaves can impair their growth. A significant negative correlation was found between dust load and pigment content (Prusty, Mishra, and Azeez, 2005). Thus, mitigation of air pollution has become a crucial challenge for environmental management agencies in urban areas. In this context, the sources and spatial distribution of dust particles are of particular concern. Some studies were performed to map air pollution by sampling particulates around city (Shu et al., 2001; Likuku, Gaboutloeloe, and Mmolawa, 2013). However, air samplers are time consuming, and high density of sampling points is also of high cost.

Recent studies have revealed that dust deposited over the plant leaves can be used as a valuable indicator for monitoring air pollution (Yang et al., 2011; Yang et al., 2011). Based on airborne pollutants accumulated on pine needles, Urbat, Lehndorff, and Schwark (2004) found that the main source for air pollution in Cologne was motor vehicle traffic. Due to wide distribution of vegetation in the urban areas, plant leaves can also be used to investigate the spatial distribution of atmospheric dust (Lu, Zheng, and Bai, 2008).

Satellites-based solution has been widely applied in the field of air pollution monitoring in recent years. Many studies used satellite image to obtain aerosol optical thickness (AOT) in a large spatial and temporal coverage (Chu et al., 2003; Gupta et al., 2006; Luo, Zhao, and Yan, 2014). However, only few researchers have applied satellite to monitor urban dust (Lue et al., 2010). Recent studies have indicated that there is a significant relationship between dust and near-infrared band region (Luo, Zhao, and Yan, 2013). The dust can increase spectral reflectance in the visible band while decrease it in the near infrared band (Peng et al., 2013). Yan et al. (2014a) used near-infrared band to estimate the amount of dust deposition on plant leaves and the results showed a good accuracy. Chudnovsky, Ben-Dor, and Saaroni (2007) developed a new spectral based method for estimating indoor settled dust weight. Ong et al. (2001) applied visible, near infrared and short wave infrared regions spectroscopy to quantify dust loads on mangroves by high spectral resolution imaging sensors. Thus, remote sensing can be used as a new way to investigate dust pollution in the urban.

1.1.2 Haze

Haze is defined as a weather phenomenon in which air has a relative humidity of $< 80\%$ and atmospheric visibility of 10 km (World Meteorological Organization, WMO). Thick haze is detrimental to the environment and public health (Hoek et al., 2010). In recent years, due to rapid worldwide urbanization, haze has become a serious problem in many countries. In China in particular (Figure 1.2), increased industrialization and fossil-fuel consumption have caused serious haze pollution. The increase in haze has been associated with mortality and morbidity from respiratory diseases and cardiovascular problems (Ram et al., 2014). Haze can contain high concentrations of heavy metals and PM, which are thought to be the most harmful pollution components (Huang et al., 2011a). Thus, mitigation of haze pollution has become a crucial challenge for environmental management agencies in urban areas. In this context, the sources and spatial distribution of haze are of particular concern.

Figure 1.2: Haze pollution in China

Many studies have been performed to analyze the physical and chemical characteristics of haze (Sun et al., 2006; Che et al., 2009). However, most studies have been based on ground and point measurements, which lack spatial coverage and may not elucidate the sources contributing to the formation of haze in widespread areas (Tao et al., 2012). To overcome this limitation, satellite remote sensing can be used to monitor and describe the spatial variability of regional haze. In recent studies, the Moderate Resolution Imaging Spectroradiometer (MODIS) has been widely applied in the field of haze analysis due to its large spatial and temporal coverage (Lee et al., 2006; Noh et al., 2009; Tao et al., 2014). For example, Tao et al. (2012) provided large-scale and long-term insights into regional haze over the North China Plain of Eastern China using MODIS data, and Han et al.

(2013) proposed an enhanced dust index for Asian dust detection.

Using satellite imagery to monitor haze aerosol optical thickness is also an effective way to assess air pollution levels. The MODIS atmospheric Level 2 aerosol product has been widely used and shown a high accuracy. It has three aerosol retrieval algorithms: dark-target (DT) land algorithm, DT ocean algorithm and deep-blue (DB) algorithm. However, the aerosol model on hazy days is very different from that on less-polluted days, the default aerosol model in the DT land algorithm of MODIS Aerosol Optical Thickness (AOT) products may be not suitable. In addition, hazy weather conditions are always accompanied by a thick aerosol layer, which causes uncertainty in the relationship between the visible (VIS) and the short-wave infrared (SWIR) bands, but it is still used in the DT land algorithm of the MODIS AOT products. Lee et al. (2006) also found that using the MODIS SWIR-to-VIS ratio to determine surface reflectance over Northeast Asia could lead to errors in aerosol retrieval. In order to monitor haze distribution, Li et al. (2013) presented an AOT retrieval method for heavy haze events based on a lookup table (LUT) method; however, the maximum retrieval of AOT by this method is 3.0, while in Beijing the AOT will be more than 5.0 on some hazy days, such as on July 6, 2014. Thus, accurate AOT retrieval is still a difficult task under hazy weather conditions. In addition, although many current aerosol retrievals make use of the LUT, it is time consuming when building it (Li et al., 2005; Wong, Nichol, and Lee, 2011; Zha et al., 2011). Tang et al. (2005) used the synergy of Terra and Aqua MODIS data (SYNTEM) to obtain AOT in China without an LUT, but the results tended to be poor when there was an obvious difference in weather conditions between two observation passes. Luo et al. (2015) proposed an improved aerosol retrieval algorithm with fast calculation and reliable outcomes; however, the method is based on Landsat images and intended for urban-scale studies, and is not suitable for haze aerosol monitoring of larger areas.

1.1.3 Fine mode aerosol

Fine mode aerosol optical thickness (FM-AOT) is a powerful and independent measure of anthropogenic aerosol emission (Lee and Chung, 2013). Bellouin et al. (2005) indicated that the fine mode fraction (FMF) can be a useful tool to separate natural from man-made aerosols. However, at present, our understanding of FM-AOT derived by FMF in a spatial perspective is still limited.

Currently, there are two easy ways to obtain the FMF; one is from the MODIS MOD04 aerosol product and the other is from the Aerosol Robotic Network (AERONET). Levy et al. (2010) reported that the MODIS-retrieved FMF over land is still an experimental product, and found that it has little physical validity. This is because MODIS retrieval algorithms have to separate the aerosol signal from the land surface signal, and there is great uncertainty in surface reflectance (Diner et al., 2005; Hauser et al., 2005; Kokhanovsky et al., 2010; Mishchenko and Geogdzhayev, 2007). Because of this, the FMF over land is much less accurate than over the ocean. However, the AERONET FMF is based on the Spectral Deconvolution Algorithm (SDA), which uses solar extinction data obtained directly from solar measurements; thus it is only slightly influenced by surface reflectance and is almost as accurate over the ocean as over land (O'Neill, Dubovik, and Eck, 2001; O'Neill et al., 2003). Gassó and O'Neill (2006) showed a good correlation between the fine mode aerosol optical thickness (AOT) from a sunphotometer and airborne in situ measurements using the SDA. However, the use of in situ samples is a limitation of the AERONET FMF because they only provide point-scale outcomes, while MODIS can provide spatial coverage of the FMF.

With atmospheric pollution worsening all over the world, researchers have used the FMF to assist in the estimation of surface PM2.5 concentration. The FMF is used to separate the contributions from smaller and larger particles in the AOT and to generate a fine mode AOT to PM conversion. Lin et al. (2015) proposed a ground-level PM2.5 model, which contains the FMF, humidity effect from hygroscopic growth, and mass extinction efficiency. Zhang and Li (2013) found that the relationship between fine mode AOT and PM2.5 was stronger than that of AOT and PM2.5 under hazy weather conditions in winter. Di Nicolantonio et al. (2007) reported a significant improvement in the correlation of this relationship when using fine mode AOT for PM2.5, with correlation coefficients (R) increasing from 0.59 to 0.74 in June. Generally, most studies have used ground-based data to develop statistical models to describe the AOT-PM2.5 relationship and then apply it to remote sensing data. Zhang and Li (2015) generated an expression between the FMF and volume-to-extinction ratio of fine particulates (VE_f) based on eight AERONET sites, and then applied it to the MODIS FMF. However, the AERONET and MODIS FMFs were derived using different methods. AERONET assumes a fine mode and coarse mode with no overlap, but MODIS uses bimodal lognormal models where the fine modes contain a coarse mode and vice versa. Additionally, the MODIS FMF is not determined as a continuous variable, but as 11 discrete values from 0 to 1. Levy et al. (2007) revealed that the MODIS FMF had essentially no correlation with the AERONET FMF. Jethva et al. (2010) compared the MODIS FMF with the AERONET FMF, and found that the root mean square difference between them was 0.61 (N = 651). Therefore, MODIS FMF may not suitable as an input parameter for the AERONET FMF-based model.

As described by O'Neill, Dubovik, and Eck (2001), it is still a challenge to apply the SDA to remote sensing data. The SDA requires multiband AOT when using a second-order polynomial fit to obtain the Angstrom exponent (AE) and AE derivative (O'Neill et al., 2003). However, most of the current satellite AOT retrieval methods only have two channels of AOT: a blue band and a red band (Zha et al., 2011; Wong, Nichol, and Lee, 2011; Luo et al., 2015; Bilal et al., 2013). If just two bands of AOT are available, the AE can be calculated by the Volz method (Soni et al., 2011), but the AE derivative cannot be obtained by a second-order polynomial fit.

1.1.4 PM2.5

Particulate matter with an aerodynamic diameter less than 2.5 μm (PM2.5, Figure 1.3) has serious adverseness to human health (Anderson, Thundiyil, and Stolbach, 2012). Many researches presented that PM2.5 is associated with mortality, respiratory system and lung cancer (Pope III et al., 2002; Brook et al., 2010; Itai et al., 2013). Particularly, a decrease of 10 μg/m^3 in the concentration of PM2.5 was associated with an estimated increase in life expectancy about six months (Pope III, Ezzati, and Dockery, 2009). Thus, it is imperative to assess accurately PM2.5 concentration distribution and exposures for making control measures to mitigate its health impacts

(Bell, Ebisu, and Peng, 2011; Luo, Zhao, and Yan, 2014).

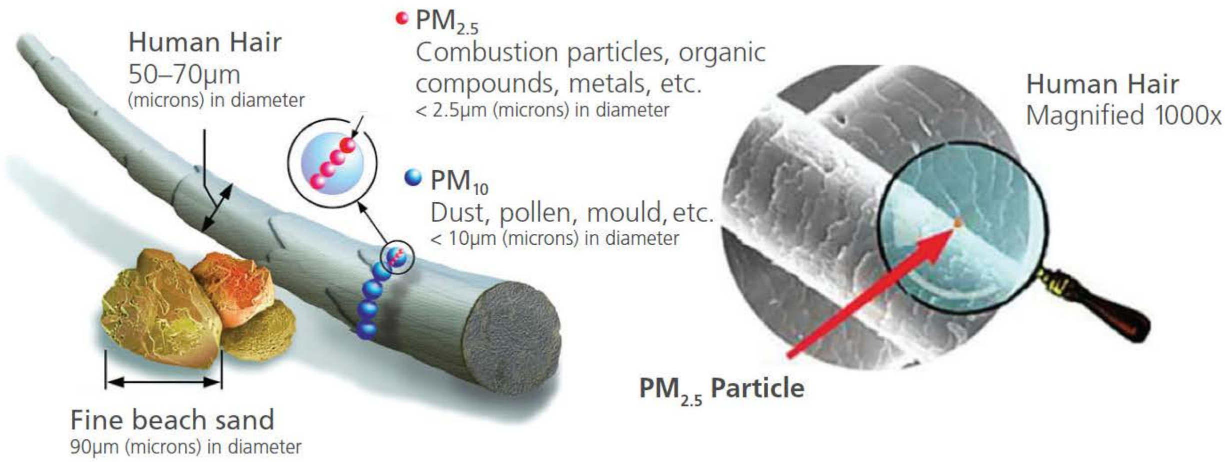

Figure 1.3: PM2.5 size in comparison to a human hair and beach sand (Image courtesy of Hazelwood Mine Inquiry Report)

Monitoring site measurement for ground-level PM2.5 is a traditional solution for pollution and health studies, but its spatial coverage is sparse and limited (Han et al., 2015). In order to obtain a large-scale PM2.5 distribution, satellite remote sensing has been used (Liu, Paciorek, and Koutrakis, 2009; Lee et al., 2011; Chudnovsky et al., 2014; Kloog et al., 2015). The common satellite product for estimating ground-level PM2.5 concentration is the AOT. Researchers have developed the relationship between AOT and PM2.5 in different methods, such as empirical statistical model (Engel-Cox et al., 2004; Gupta et al., 2006; Schaap et al., 2009; Guo et al., 2014), chemical transport model (Wang et al., 2010a; Van Donkelaar et al., 2010; Liu et al., 2011; Xu et al., 2013) and physical model (Kokhanovsky et al., 2009).

Despite promising progress has been made recently in surface PM2.5 estimation from satellite AOT, uncertainties still exist due to several factors. The planetary boundary layer height (PBLH) was reported to have significant impact on AOT-PM2.5 relationship (Gupta and Christopher, 2009). This is because the greater PBLH is more favorable to the dilution and diffusion of the pollutants, which decreases concentration of surface PM2.5 in spite of high AOT (Qu et al., 2016). The relative humidity (RH) was found to be another factor that could result in discrepancies between AOT and surface PM2.5 (Wang and Christopher, 2003; Paciorek et al., 2008). Wang et al. (2010b) indicated a significant improvement in surface PM2.5 estimation when relative humidity correction was performed (R^2 increased from 0.35 to 0.66). Furthermore, previous studies have always used the MODIS AOT products (MOD04) for PM2.5 monitoring, but its spatial resolution is 10 km, which is not appropriate for exposure estimates in urban areas (Jerrett et al., 2005). In addition, Chudnovsky et al. (2013) pointed out the spatial resolution of AOT affected PM2.5 accuracy, correlation between AOT and PM2.5 decreased significantly as AOT resolution degraded. Although MODIS has released 3 km AOT product recently, the accuracy assessment was less reliable than 10 km AOT's (Munchak et al., 2013; Yan et al., 2016).

Most of the previous studies using satellite AOT to derive PM2.5 focused on the total AOT (Eeftens et al., 2012; Lee et al., 2012; Luo, Zhao, and Yan, 2014). However, some researchers found that fine mode AOT (FM-AOT) can have a better correlation with ground-level PM2.5 (Di Nicolantonio et al., 2007; Zhang and Li, 2013). Van Donkelaar et al. (2011) applied FM-AOT for PM2.5 estimation in the Moscow and the results showed a high accuracy. Di Nicolantonio et al. (2007) presented an obvious improvement by using FM-AOT for PM2.5 in June. Although these studies showed the improvement by FM-AOT, the comparison between total AOT and FM-

AOT for PM2.5 is still limited.

On the other hand, as FM-AOT is involved in PM2.5 retrieval, the fine model fraction (FMF) that pertains the contributions of smaller and larger particles to the AOT is becoming a more and more important parameter. Zhang and Li (2015) proposed an expression between AERONET FMF and volume-to-extinction ratio of fine particulates (VE_f) for PM2.5 retrieval, and then applied it using MODIS FMF. Nevertheless, AERONET FMF has a very different calculation method from MODIS FMF (Gassó and O'Neill, 2006). Levy et al. (2007) revealed that MODIS FMF had a poor correlation with AERONET FMF, and Zhang and Li (2015) also showed the same phenomenon.

1.2 Research objectives

Based on the aforementioned issues, four objectives of this research have been identified as follow:

- To establish a reliable method for dust distribution with the aid of satellite images and plant leaf spectral data.
- To develop a new algorithm to obtain aerosol conditions; it includes haze identification and AOT retrieval not only on hazy days but also in normal weather.
- To propose a practical and effective method of FMF retrieval for fine mode aerosol.
- To design a ground-level PM2.5 retrieval model based on fine mode aerosol.

1.3 Dissertation outline

The outline of the dissertation is summarized as Figure 1.4, which is based on the particle size from large to small (Figure 1.5). Chapter 2 presents dustfall retrieval based on satellite and ground-based data. The enhanced haze aerosol retrieval algorithm for haze aerosol is introduced in Chapter 3. Then a Look up table based Spectral Deconvolution Algorithm for fine mode fraction is introduced by Chapter 4. Retrieval surface PM2.5 based on fine mode aerosol optical thickness is described in Chapter 5. Finally, Chapter 6 discusses the summary and conclusions of this study.

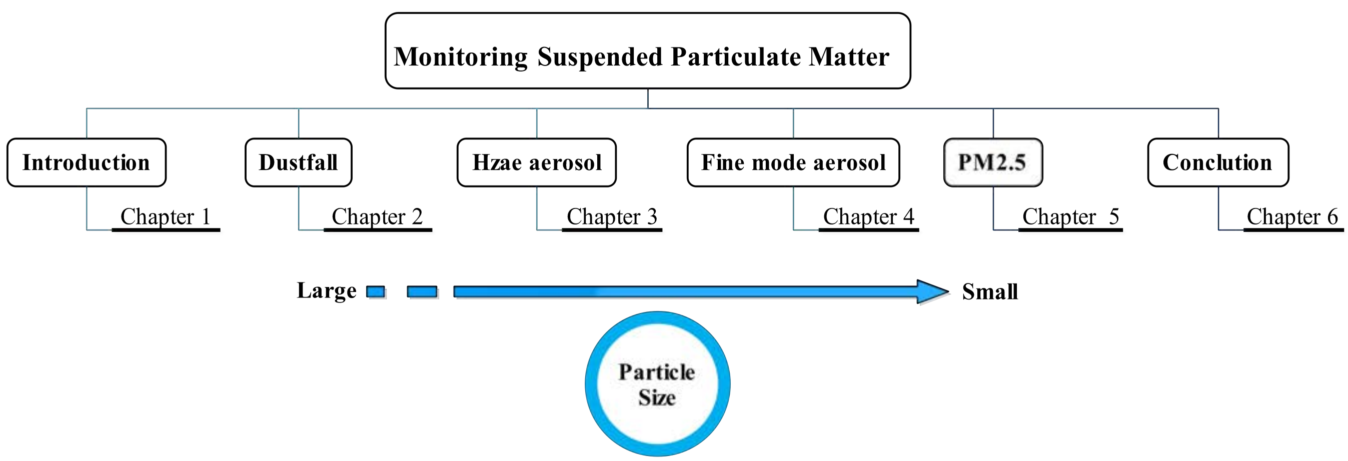

Figure 1.4: Outline of the dissertation

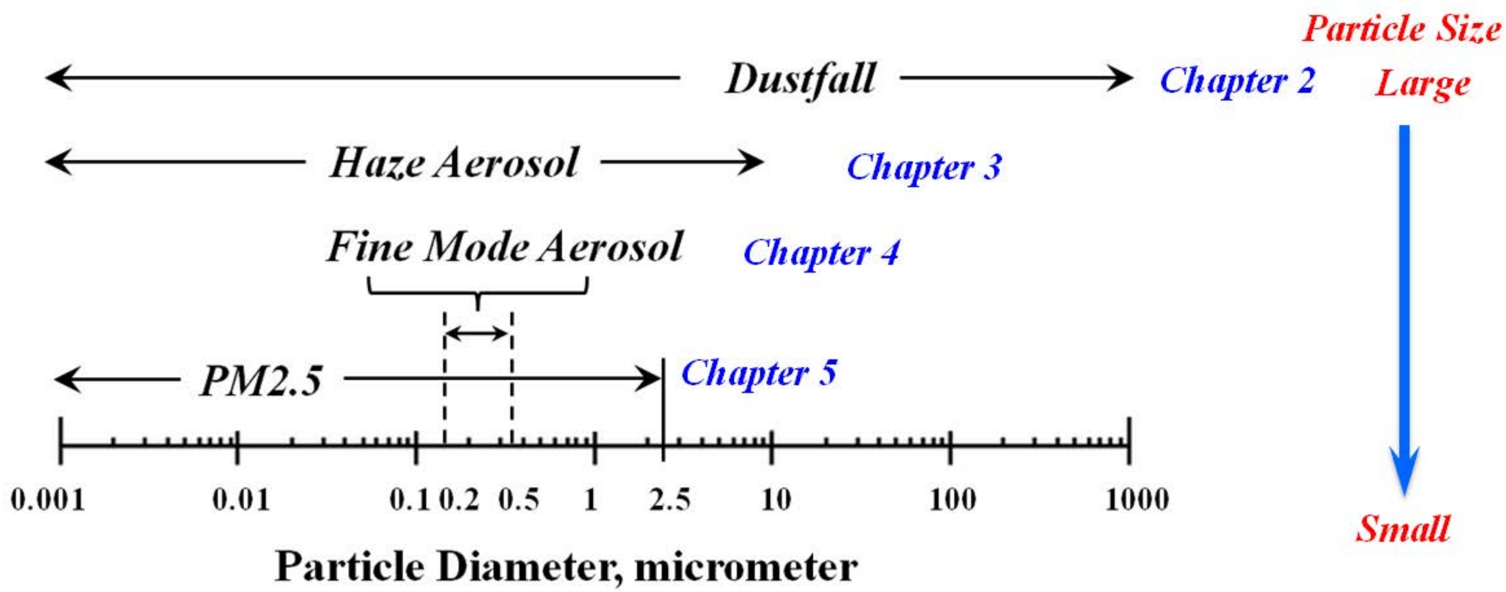

Figure 1.5: Particle size in the different Chapter

Chapter 2

Mapping Dustfall Distribution in Urban Areas

2.1 Introduction

Generally, dustfall is considered as the solid particulate matters with a diameter less than 1 mm and is widely distributed in the whole urban area. With the external dynamic effects, these particles will suspend again, which is an important pollutant in cities due to this reciprocal cycle of lifting and settling. Thus, it is necessary to obtain the spatial distribution of dustfall in the city and to know the pollution level. The purpose of this chapter is to establish a reliable method for monitoring dust distribution with the aid of satellite images and plant leaf spectral data. This research first analyzed the correlation between spectral reflectance and dust on plants. Based on this correlation, dust distribution is derived using a neutral network model. Finally, the sources of dust in urban areas are discussed as well. This chapter is based on Yan et al. (2015).

2.2 Materials and methods

2.2.1 Satellite data

MODIS Terra L1B data of the overpass at 10:30 am were obtained from NASAs Goddard Space Flight Center (http://modis.gsfc.nasa.gov). The MODIS L1B data contains calibrated and geolocated at-aperture radiances for 36 bands generated from MODIS Level 1A sensor counts (Bilal et al., 2013). This study used MODIS images acquired on July 2, August 3, and September 25 2013. Table 2.1[1] lists the weather information from the days when MODIS overpassed.

Table 2.1: Weather information during MODIS overpass

Date	**Wind direction**	**Wind Speed**	**Relative Humidity**	**AOT at 550 nm**
7/2/2013	290	5	49	0.11
8/3/2013	130	2	43	0.25
9/25/2013	290	4	18	0.06

2.2.2 Plants collection

In this study, Euonymus japonica L., Sophora japonica L., and Populustomentosa L. Carr. were selected as experimental plants. Euonymus japonica L. is one of the main shrub species in Beijing, while Sophora japonica L. and Populustomentosa L. Carr. are also common in this area (Yang et al., 2005; Yan et al., 2014b). The above plants have been widely used for landscaping around cities. Experimental leaf samples were collected from 44 sampling locations around Beijing, and their spatial distributions are shown in Figure 2.1.

[1]Unit:Wind direction is degree,Wind Speed is m/s, Relative Humidity is %

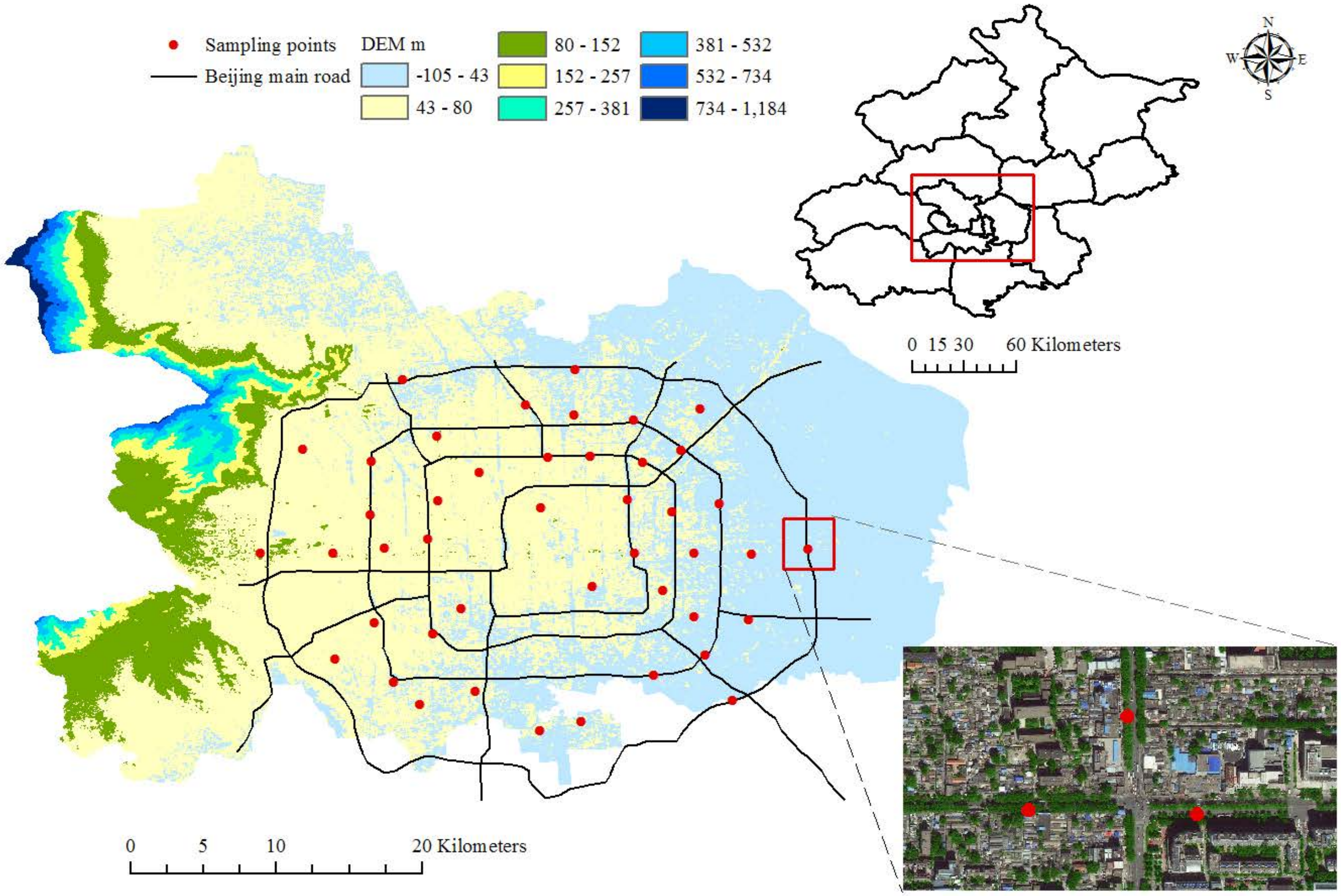

Figure 2.1: Plant sampling locations

2.2.3 Spectral measurements and processing

Initially, each plant leaf was weighed using an electronic analytic balance (1/10,000 g scale). Then, the spectral reflectances of the leaves were measured using a spectrometer (Analytical Spectral Devices FieldSpec Pro, ASD 2008) equipped with a Plant Probe (ASD auxiliary product, Halogen bulb light source type, Figure 2.2) and an ASD Leaf Clip (Figure 2.3). The ASD is a single-beam field spectroradiometer covering a range of 350-2,500 nm with a total of 2,100 spectral bands. The spectral measurements were repeated 10 times for each sample, and the mean value was taken to represent each leafs spectral reflectance (Hansen and Schjoerring, 2003; Haboudane et al., 2004). Subsequently, leaves were cleaned with ultra-pure water and dried by absorbent paper. The cleaned leaves were reweighed, and the reflectances were measured again. Although leaf reflectance is affected by many factors, such as chlorophyll, plant health, and water content, this research compared reflectance data between dust and clean leaves, which was referred to as a samples' self-comparison and, thus, neglected possible interfering factors.

Figure 2.2: The ASD Contact Probe

Figure 2.3: The Leaf Clip

Another issue was that, due to low spatial resolution of MODIS images and the limited study area, urban cities always contained mixed pixels, which made dustfall retrieval inaccurate. Thus, when collecting leaf samples, the selected locations needed to be widely covered by vegetation cover. In addition, in order to eliminate the interference of plant type on the retrieval result, mean spectral values for three plants at single site were calculated and used for final dustfall weight calculations.

In order to transfer ground-measured data to satellite images, a leafs narrow-band spectra was resampled at broad-band according to the relative spectral response function of MODIS. The MODIS spectral response function is as follows (Ghulam et al., 2008):

$$R_{MODIS}(\lambda) = \frac{\int_{\lambda_{\min}}^{\lambda_{\max}} R_{Leaf}(\lambda) f(\lambda) d\lambda}{\int_{\lambda_{\min}}^{\lambda_{\max}} f(\lambda) d\lambda} \tag{2.1}$$

where $R_{MODIS}(\lambda)$ refers to broad-band reflectance, $f(\lambda)$ refers to the MODIS spectral response function at a corresponding waveband, $\lambda_{\min}$ and $\lambda_{\max}$ refer to the lower and upper limit of band internal, and indicates the center wavelength (nm) in each band. Then, the ratio of the reflectance between dust and clean leaves was calculated by the following:

$$r(\lambda) = \frac{R_{MODIS}^{Dust}(\lambda)}{R_{MODIS}^{Clean}(\lambda)} \tag{2.2}$$

where $R_{MODIS}^{Dust}(\lambda)$ and $R_{MODIS}^{Clean}(\lambda)$ are dust and clean leafs reflectance corresponding to a specific band of MODIS.

2.2.4 Dustfall retrieval

The central idea of this retrieval method is to find out the relationship between spectral reflectance and dustfall weight and to sequentially use dust images and clean images as input parameters to calculate the whole dust distribution. Plant leaves can be cleaned by heavy continuous rain (Przybysz et al., 2014). Thus, based on Table 2.2, MODIS images from July 2 2013 were considered clean images, and images from August 3 and September 25 2013 were considered dust images.

Table 2.2: Weather information from June 28 to July 2, 2013

Date	**Weather Condition**	**Air temperature (day/night)**
6/28/2013	moderate to heavy rain	33/21°C
6/29/2013	showery rain	30 /22°C
6/30/2013	showery rain	28/22°C
7/1/2013	heavy rain	28/20°C
7/2/2013	sunny	34/23°C

As shown in Section 2.3.1, it could be existing nonlinear correlation between spectral reflectance and dustfall weight. The Back Propagation (BP) Neutral Network model is considered a generalization of the delta rule for nonlinear activation functions and has been successfully applied in many environmental studies (Tumbo, Wagner, and Heinemann, 2002; Pal et al., 2003; Şahin, 2012; Valipour, Banihabib, and Behbahani, 2012; Valipour, Banihabib, and Behbahani, 2013). Thus, it was used to retrieval dustfall weight in this research. For this BP model as showed in Figure 2.4, the training data were $r(\lambda)$ and dust weight per unit area ($Dustweight \div Leafarea$, N=180), and the simulation data were MODIS reflectance ratios between dust and clean images.

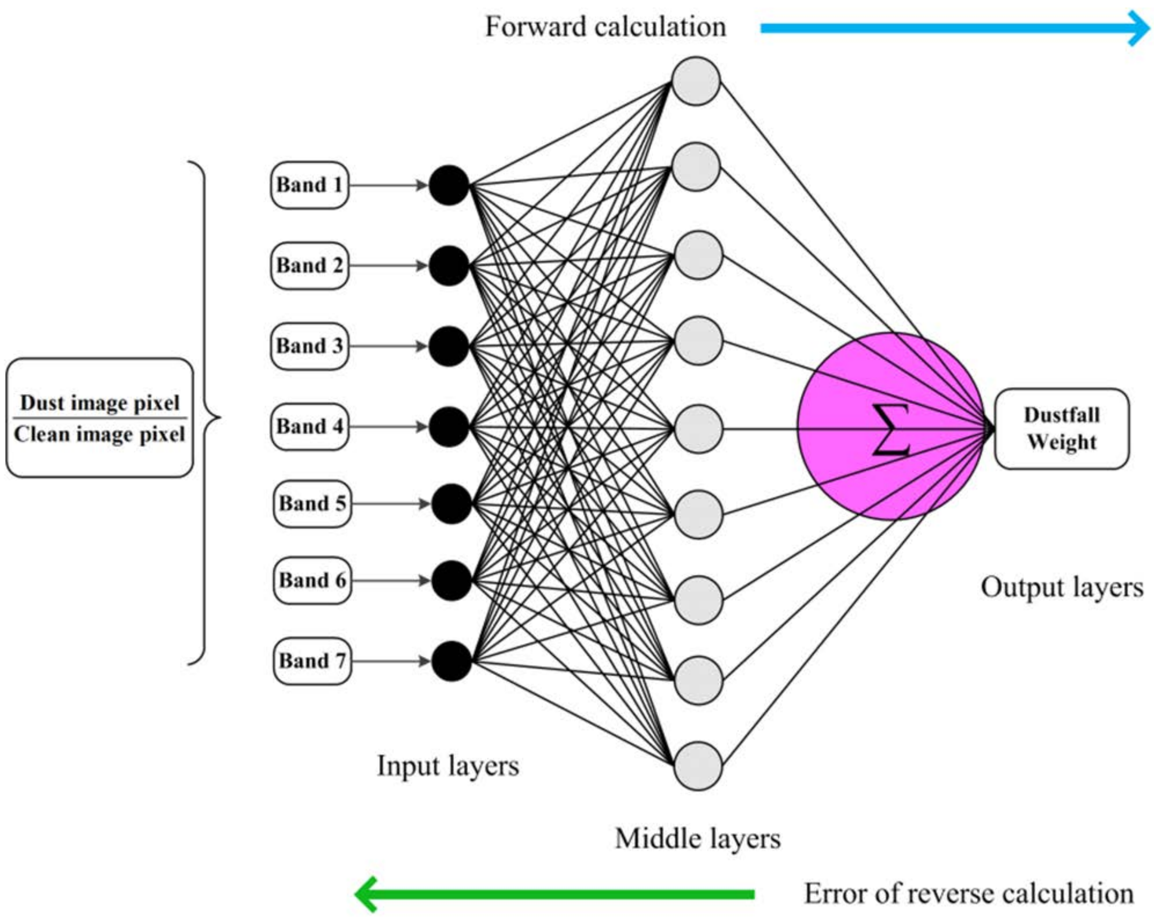

Figure 2.4: Back Propagation neural network flow-chart of dustfall retrieval

This model consisted of 15 nodes in the middle layer; tansig/tansig was chosen as the transfer function and trainlm as the train method. These parameters were determined by optimal mean squared error (MSE) and training time epochs as showed in Figure 2.5, Figure 2.6 and Figure 2.7.

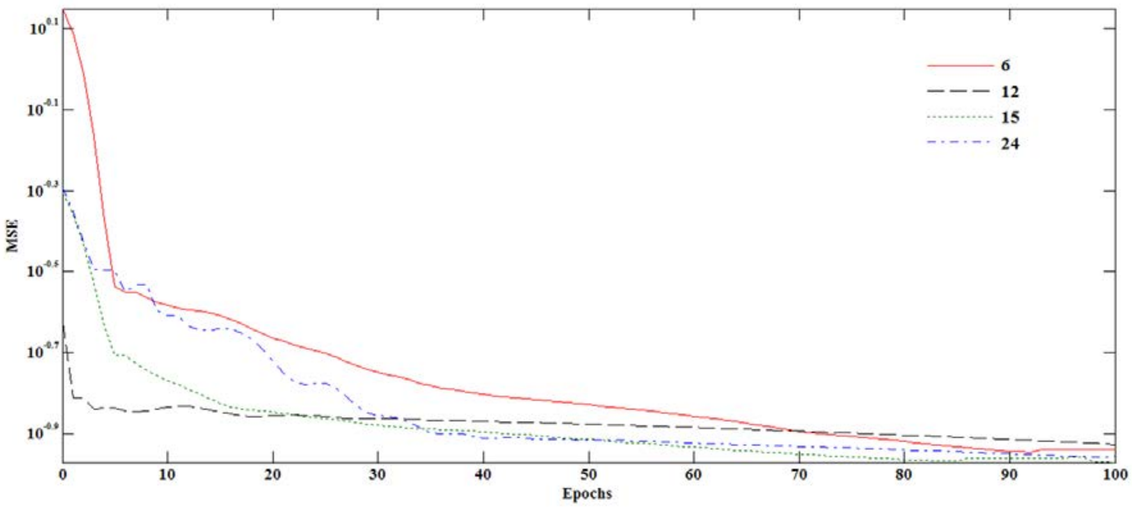

Figure 2.5: Selection of models nodes in the middle layer

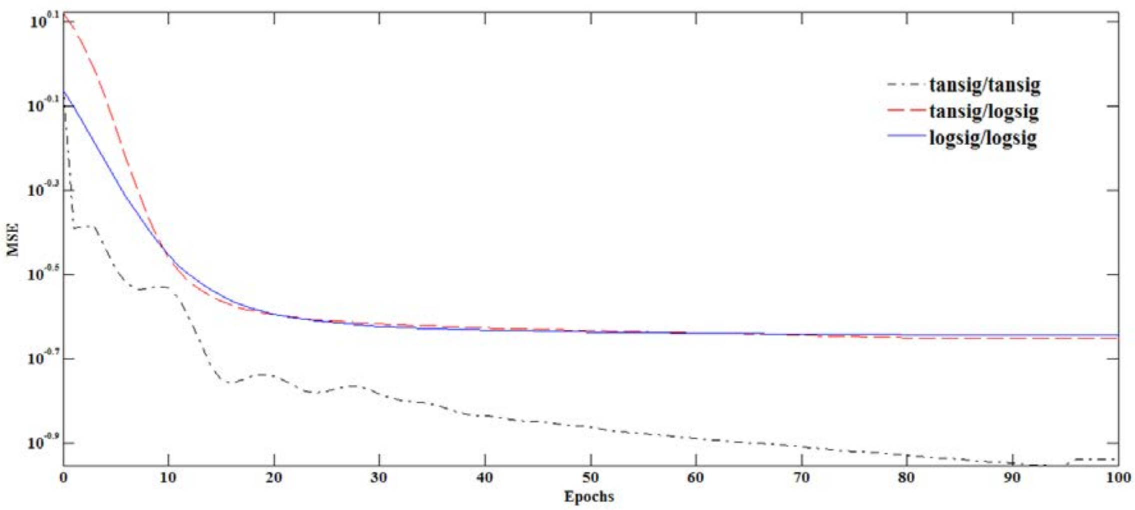

Figure 2.6: Selection of transfer functions

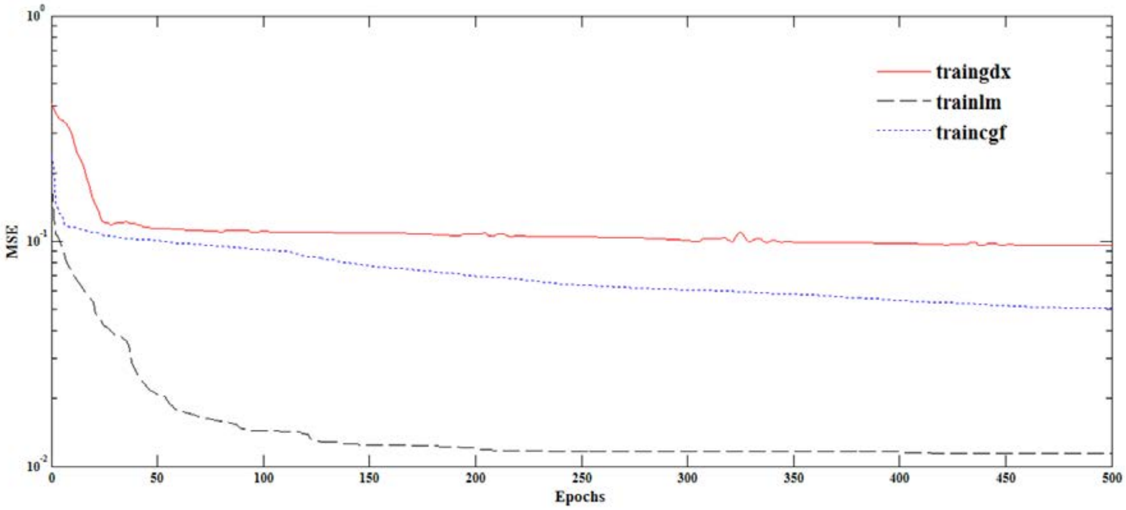

Figure 2.7: Selection of train methods

Figure 2.8 shows the workflow for dustfall retrieval. At first, MODIS data were processed by the Second Simulation of a Satellite Signal in the Solar Spectrum (6S) model to conduct atmospheric correction and calculate surface reflectance. Then, because Normalized Difference Vegetation Index (NDVI) values corresponding to sampling locations were always greater than 0.4, NDVI in these ranges were extracted. Finally, dustfall weights in these extracted regions were retrieved by a BP Neutral Network model, and Kriging interpolation was adopted to derive the whole dustfall distribution image.

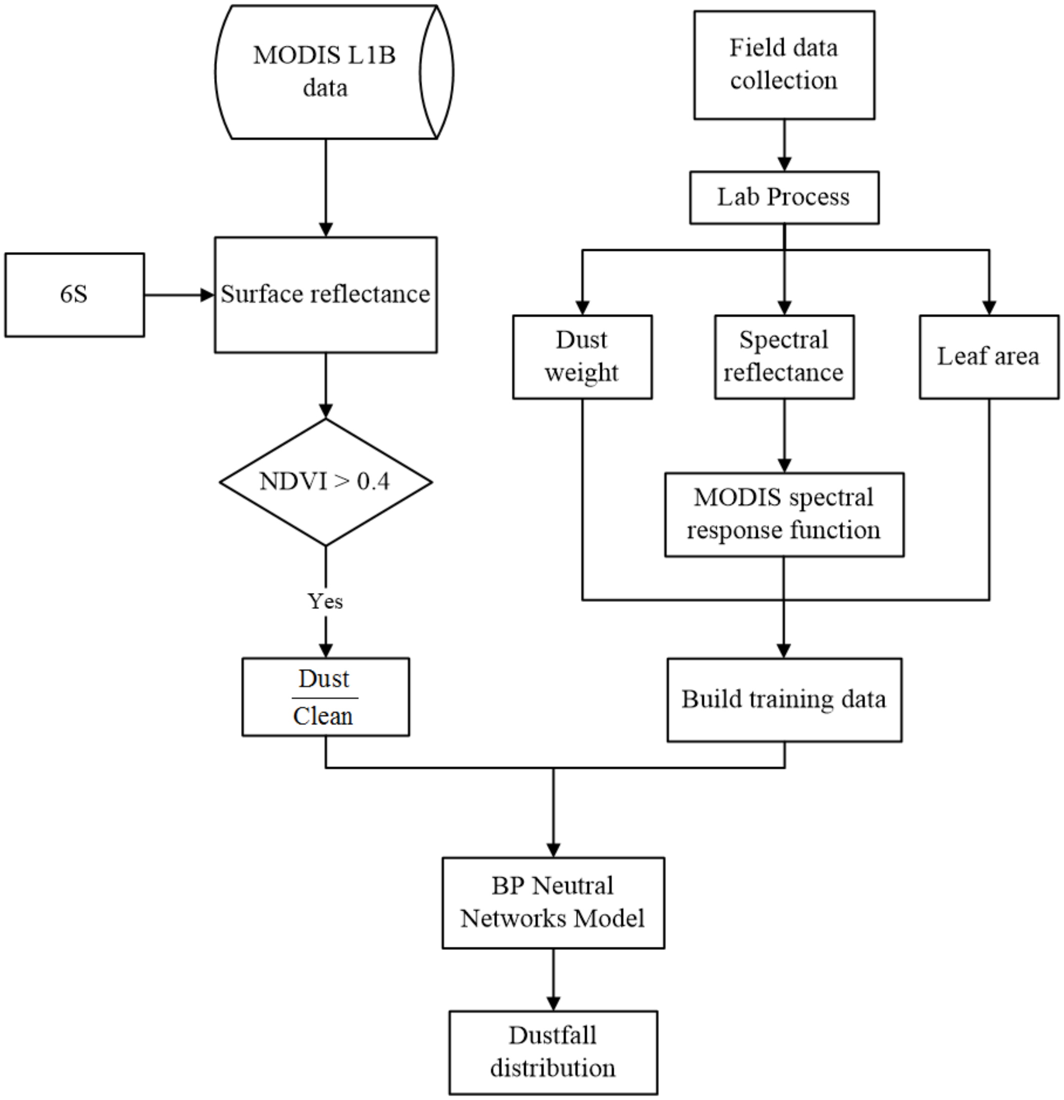

Figure 2.8: Schematic diagram of dustfall retrieval

2.2.5 Dustfall validation

This research used ground-measured dustfall weight to validate the retrieval results. As shown in Figure 2.9, empty bottles were numbered and weighed. Then, these bottles were hung on the pillars around Third Ring Road (Figure 2.10) in Beijing, resulting in a total of 14 sampling sites (Hua Yuan Qiao, Li ZeQiao, Wan Shou Si, Si Tong Qiao, Ji Men Qiao, Bei Tai Ping Qiao, Ma Dian Qiao, An Zhen Qiao West, An Zhen Qiao East, San Yuan Qiao, Liang Ma Qiao, ShuangJin, Pan Jia Yuan and Ba Yi Hu). The sampling time was from July 2 to August 1 2013.

Figure 2.9: Validation sampling locations

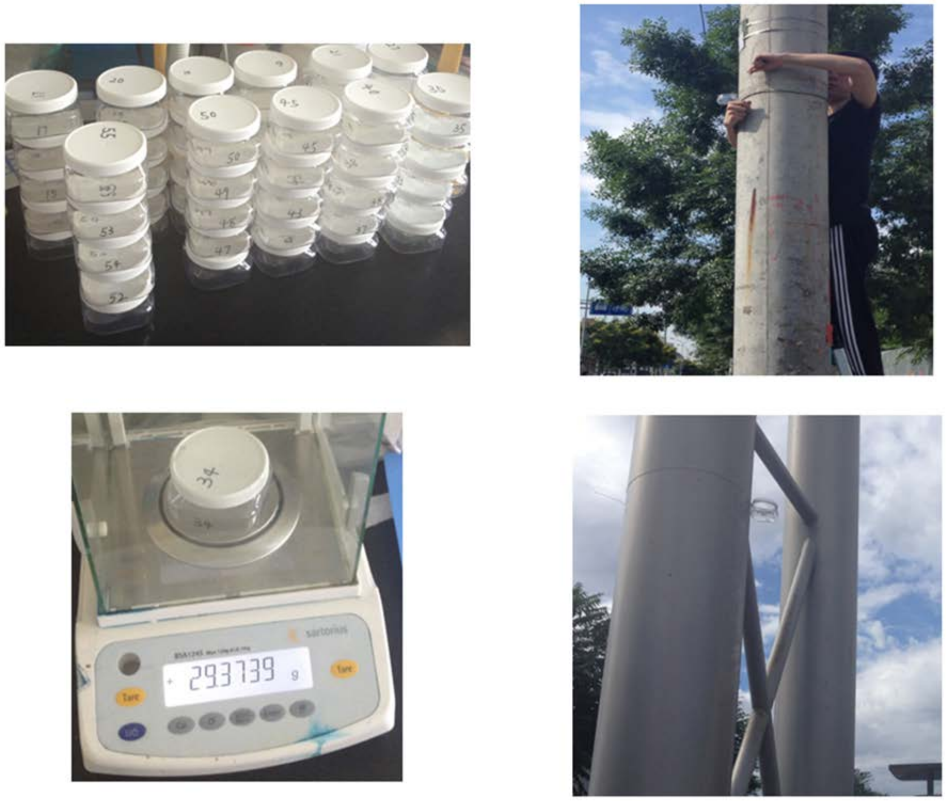

Figure 2.10: Sampling bottles for validation

2.3 Results

2.3.1 Influence of dustfall on plants spectral features

Figure 2.11 A, B and C show the difference in spectral reflectance values between dust and clean leaves for three kinds of plants. It is apparent that the trend in clean leaf reflectance is similar to dust, but their reflectances have significant differences for specific bands. Dust leaves have a higher reflectances than clean leaves at 350-700 nm, indicating that dustfall reflects energy over this interval, and at 780-1300 nm dust reflectance is obviously lower than clean leaf reflectance. Although there are fewer reflectance differences between dust and clean leaves at greater than 1300 nm, small amounts of dust sediment over this range can be effectively examined (Chudnovsky, Ben-Dor, and Saaroni, 2007). These features mentioned above are consistent with previous findings by Wang et al. (2012), Luo, Zhao, and Yan (2013) and Peng et al. (2013), which revealed that reflectance differences between dust and clean leaves indeed exist.

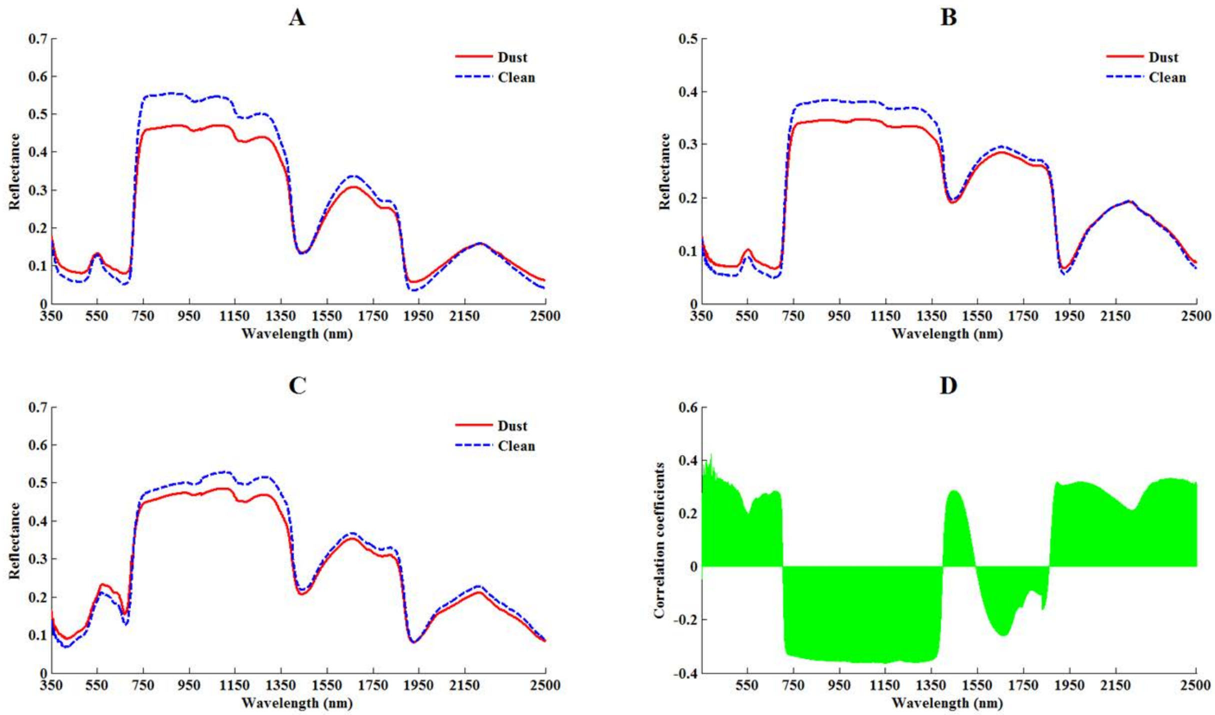

Figure 2.11: Impact of dust on spectral features: A) Euonymus japonica; B) Sophora japonica L.; C) Populustomentosa Carr.; D) correlation analysis between reflectance ratios (Dust/Clean) of the three types of plants and dustfall weight.

Figure 2.11 D shows the correlation coefficients between dustfall weight and leaf reflectance ratios (Dust/Clean). Generally, between 350-700 nm, 1400-1540 nm, and 1860-2500 nm positive correlations were present with dustfall, while 700-1400 nm and 1540-1860 nm showed negative relationships. Specifically, the 750-1350 nm interval contained a low point, reaching -0.38; 1350-1550 nm and 1950-2500 nm wavebands displayed a contrary positive relationship with dust weight, and the correlation value reached

0.4.

Further correlation analysis between resampled spectral data $r(\lambda)$ and dustfall weight was performed (Figure 2.12). The results showed that generally the correlation trend was consistent with Figure 2.11 D: r(865), r(1240), and r(1640) were strongly and negatively related to leaf dust, peaking at -0.47, -0.48, and -0.37, respectively. In addition, r(550) had the lowest positive relationship with dust (0.21). Correlation coefficients of r(470), r(660), and r(2130nm) ranged from 0.3 to 0.34. Similar to these results, Chudnovsky and Ben-Dor (2008) also found that spectrum correlated with dust content. Thus, they could be used to predict the dust weight.

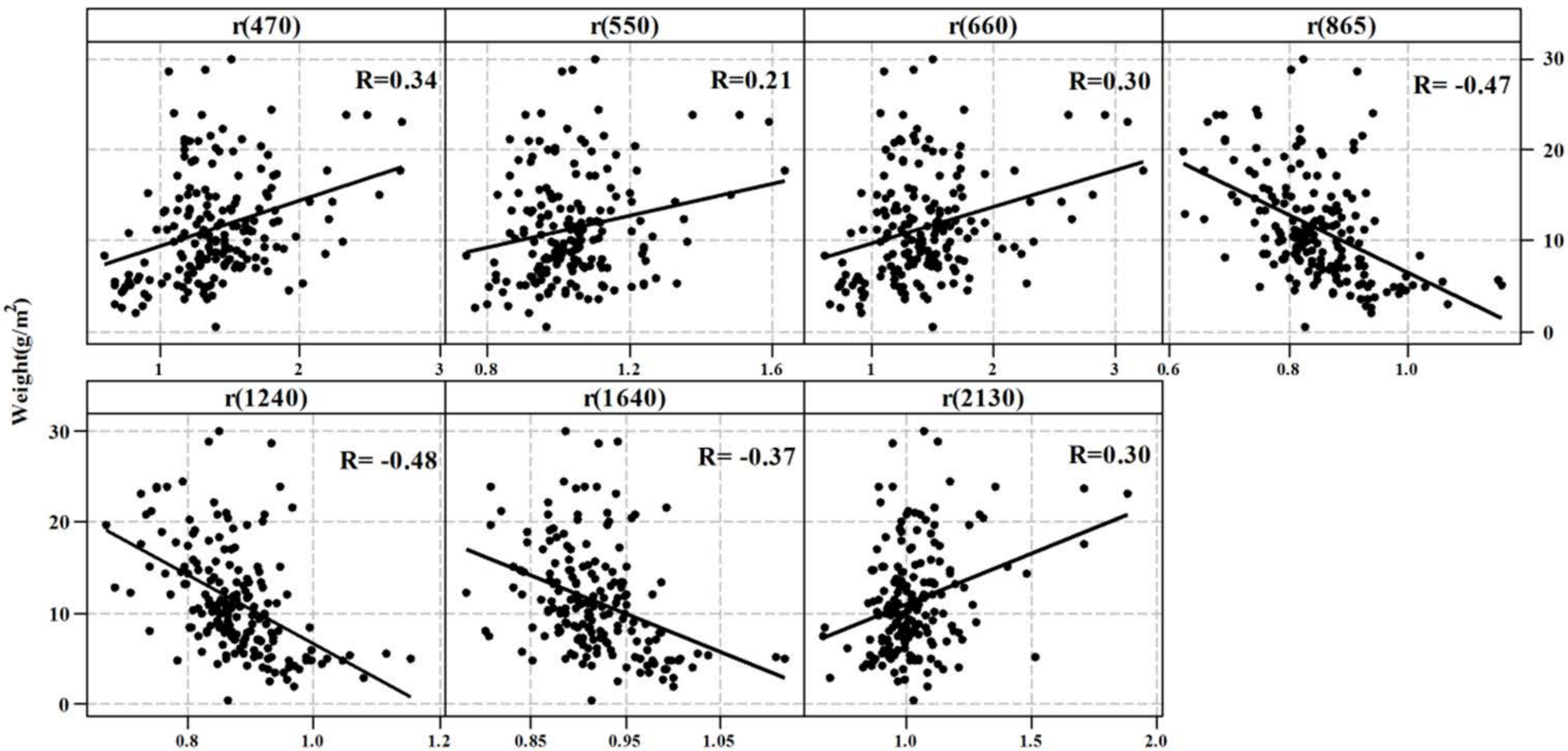

Figure 2.12: Correlation analysis between $r(\lambda)$ and dustfall weight (N=180)

2.3.2 Dustfall retrieval and validation

Figure 2.13 shows the results of dustfall retrieval in the Beijing urban area on August 3 and September 25 2013 based on BP Network. It is clear that the spatial and temporal variation of dustfall was significant during these periods. The results from August 3 reveal that high values concentrated at sampling locations in the northern corner of the city, such as Fang's Lane and An Ding Men. In addition, there were many hotspots located around the main roads with values ranging from 15 to 23 g/m^2. On September 25, dustfall levels increased and the hotspots continually extended. Southern areas of the city, such as the southeast of Second Ring Road and the southwest of Third Ring Road, experienced a rapid dustfall increase. To the north of the city, regions with elevated dustfall on September 25 were larger than those observed on August 3, particularly in Jian Xiang Qiao and An Hua Qiao. The dustfall histogram shown in Figure 2.14 also indicates that September 25 had a mean value of 12.36 g/m^2, which was higher than the value observed on August 3 (10.98 g/m^2). Additionally, the retrieved dustfall followed normal distribution with small standard deviations of 2.104 (September 25) and 2.046 (August 3).

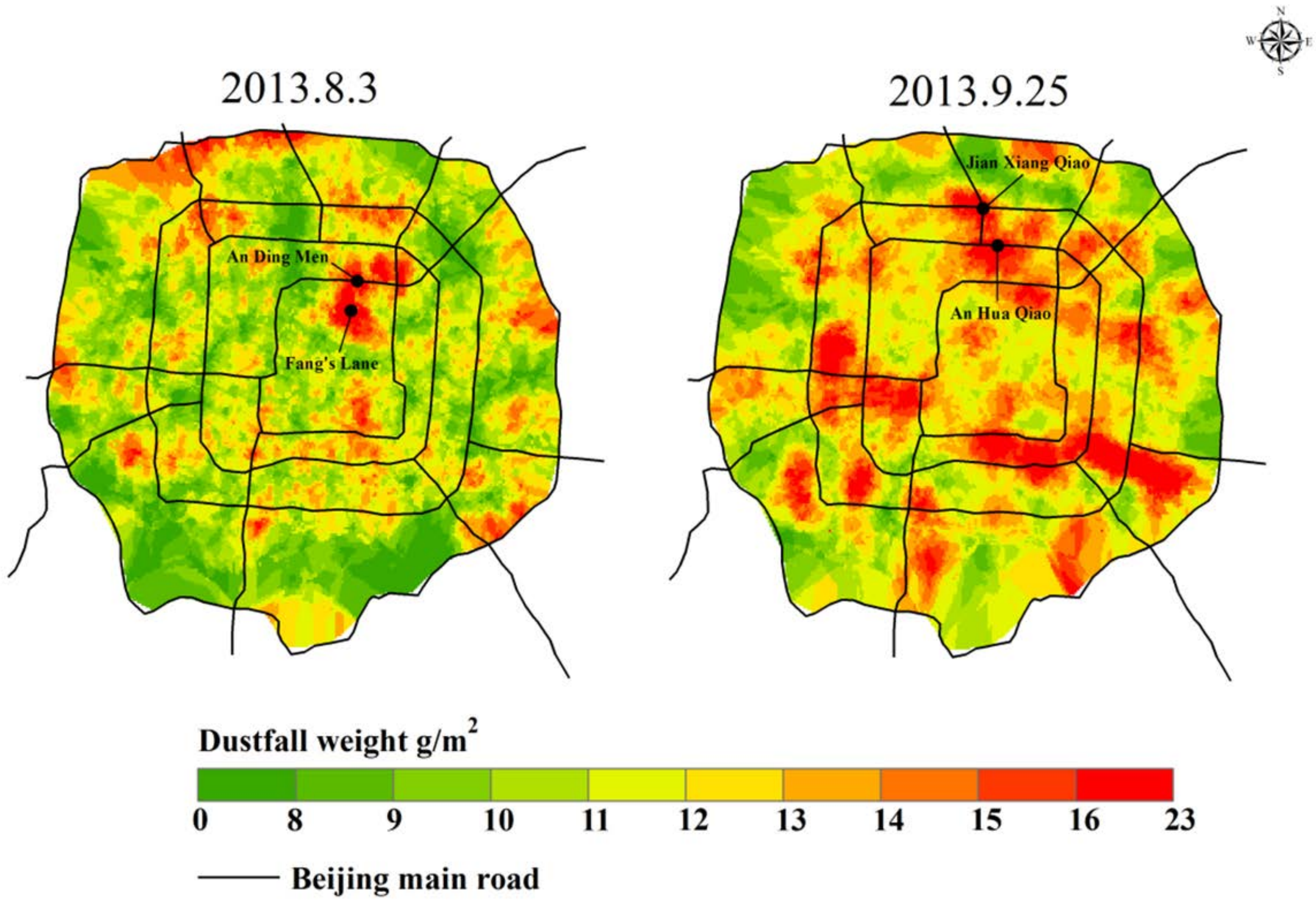

Figure 2.13: Derived dustfall distribution in the city of Beijing

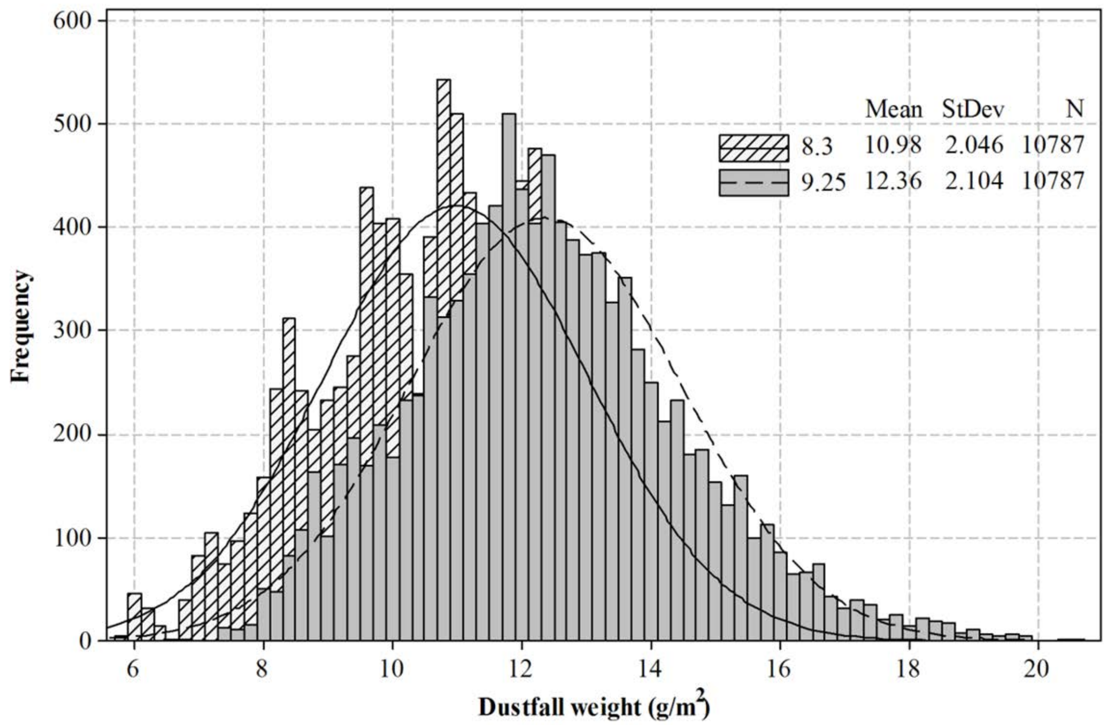

Figure 2.14: Histogram of derived dustfall on August 3 and September 25, 2013

To evaluate the performance of the retrieval results, derived dustfall was compared with validation bottle data (Figure 2.15). The comparison shows that the change trend of the retrieved results agrees well with bottle measurements, and a low Root Mean Square Error (RMSE) value of 3.6 indicates satisfactory estimation accuracy. However, the retrieved dustfall was slightly higher than the actual measurements, which may be related to the fact that satellite reflectance not only accounts for surface reflectance, but also contains noise, like Bidirectional Reflectance Distribution Function (BRDF) effects and surrounding noises. Although the 6S model was utilized to reduce these influences, there were still errors that could not be eliminated.

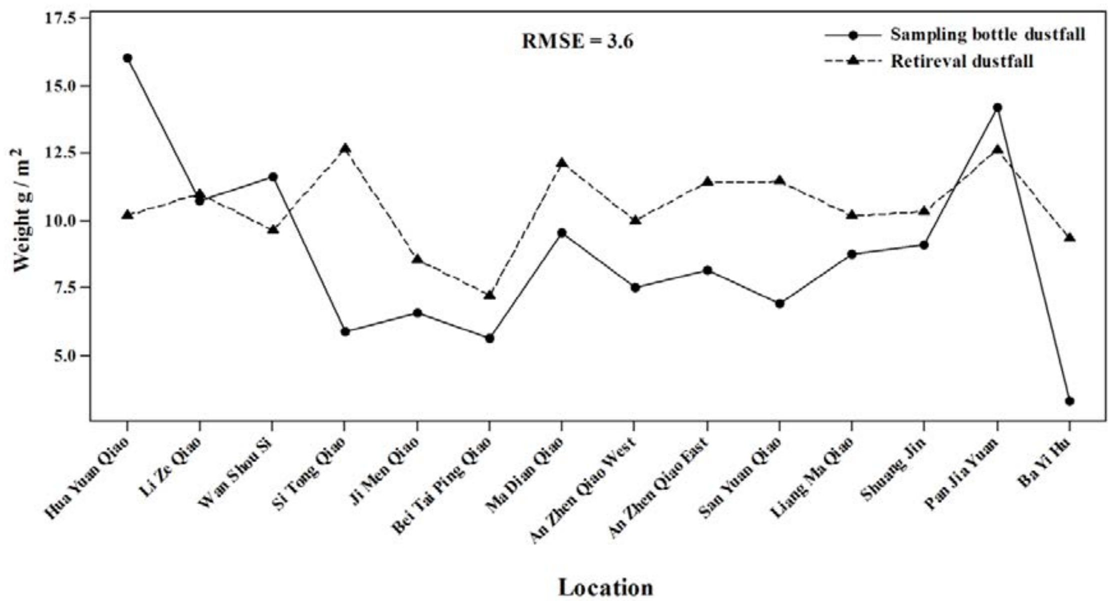

Figure 2.15: Retrieved dustfall validation with actual measurement data

2.3.3 Dustfall source analysis

The spatial distribution of dustfall is influenced by many factors related to land cover activities, such as building and population, air flushing rates, and the distribution of transportation networks. Figures 2.16 A and B show an under-construction subway station beside the Olympic Sports Center and a construction site for business activities, respectively. These construction projects are all in the high dustfall level regions and could be the main source of dust pollution (Tsang, 1996). Weng and Yang (2006) also indicated that construction sites contributed dust and particles and were prone to causing air pollution problems.

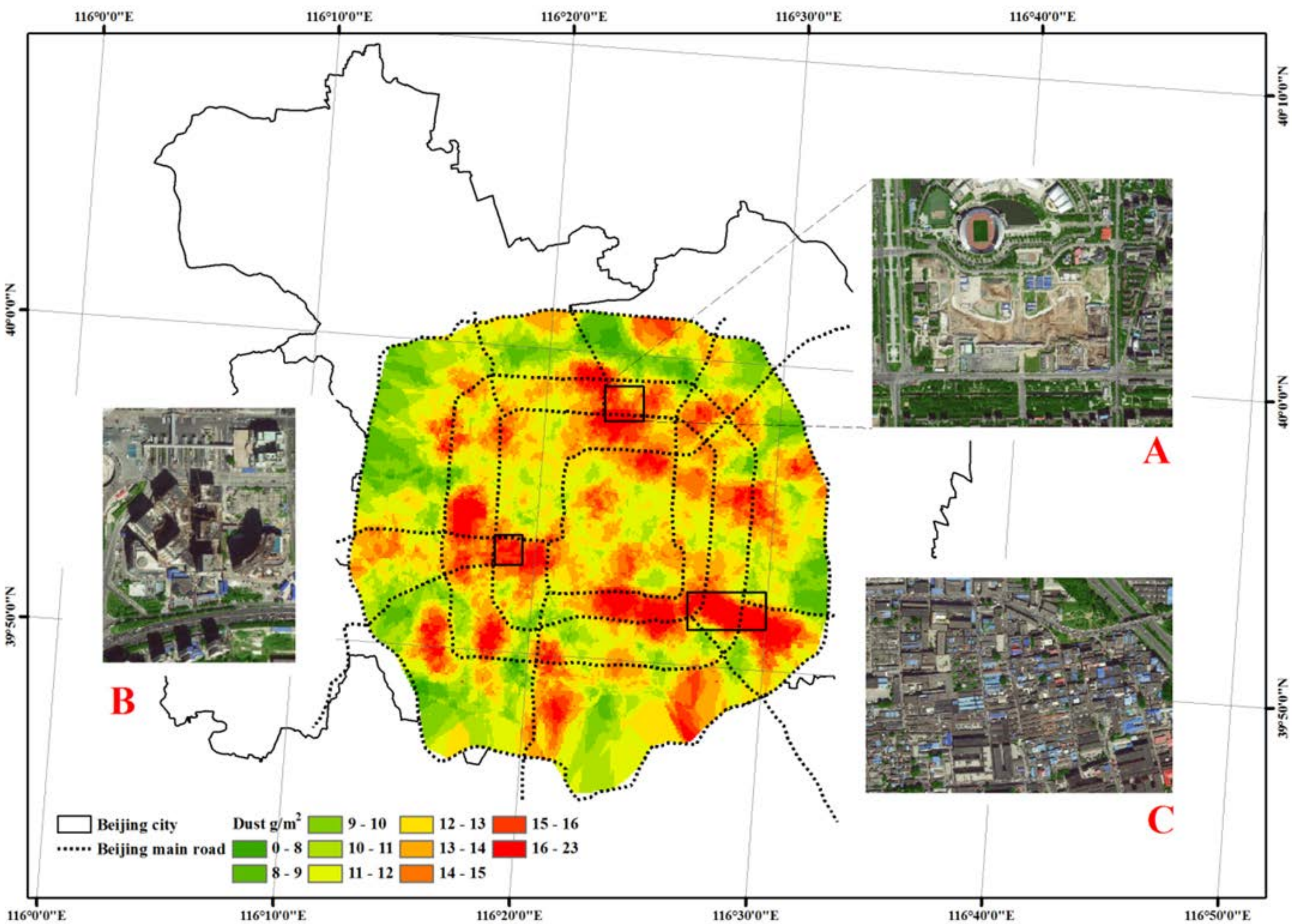

Figure 2.16: Analysis of Dustfall source: A) an under-construction subway station; B) a downtown business construction site; C) cottage areas.

Due to the old age of Beijing, some of the buildings in the studied area are low-rise and in dilapidated condition (Figure 2.16 C). They are closely packed along the road with little space between buildings (Figure 2.17). The lack of space between the buildings can easily trap air emissions, and dustfall would be serious in these air sheds with limited dispersive capacity. Homeowners might want to maximize the use of land, resulting in limited open spaces, which are necessary for air ventilation. In addition, transport related dust pollution could also be serious in these areas. Emissions from vehicles diffuse poorly due to the lack of space between old buildings.

Figure 2.17: Buildings in cottage areas

2.4 Discussion

Combined with ground sampling and spectrum measurement data, satellite can be used as a tool to map dustfall distribution over large areas. The method proposed in this research not only represents an original technique to observe air pollution by calculating the whole dust distribution, but also directly connects satellite data to observed values at a very low cost. Unfortunately, the low spatial resolution of MODIS cannot exactly match the sampling sites for leaf collection and, thus, a high accuracy retrieval result is not expected. To combat this limitation, this study selected sampling locations that were widely covered by vegetation and corresponded to satellite pixels as much as possible to reduce the influence of mixed pixels. Another issue of concern is that leaf reflectance can be altered by vegetation phenology. Liang, Zhong, and Fang (2006) indicated that, except for extreme weather impacts, surface properties do not change dramatically within a 3-month period. From the validation results, the trend of retrieved dustfall agrees well with real measurements, which illuminates the reliability of this method and demonstrates the utility of the results as a tool for curbing environmental pollution. Nevertheless, there are still errors between satellite and ground based data, and the retrieved results do not have a very high accuracy. Thus, techniques for further improving accuracy remain vital and require further study.

2.5 Summary

The aim of this chapter was to utilize remote sensing and ground-based spectral data to assess dustfall distribution in urban areas. The ground-based spectral data denoted that dust has a significant impact on spectral features. Dusty leaves have an obviously lower reflectance than clean leaves in the near-infrared bands (780-1,300 nm). The correlation analysis between dustfall weight and spectral reflectance showed that spectroscopy in the 350-2,500-nm region produced useful dust information and could assist in dust weight estimation. A back propagation (BP) neutral network model was generated using spectral response functions and integrated remote sensing data to assess dustfall weight in the city of Beijing. Compared with actual dustfall weight, validation of the results showed a satisfactory accuracy with a lower root mean square error (RMSE) of 3.6 g/m^2. The derived dustfall distribution in Beijing indicated that dustfall was easily accumulated and increased in the south of the city. In addition, the outcomes of this chapter showed that construction sites and low-rise buildings with inappropriate land use were two main sources of dust pollution. This chapter offers a low-cost and effective method for investigating detailed dustfall in an urban environment. Environmental authorities may use this method for deriving dustfall distribution maps and pinpointing the sources of pollutants in urban areas.

Chapter 3

Remote Sensing for Haze Aerosol Monitoring

3.1 Introduction

The particulate size of haze aerosol is much smaller than dustfall, which is between 0.001 μm to 10 μm (diameter) and its mean diameter is 1 μm to 2 μm. Along with rapid economic growth, haze has become one key environment issues in China. For example, extremely severe haze pollution happened in Beijing-Tianjing-Hebei region, with high level of PM2.5 affecting about 800 million people. Therefore, monitoring haze distribution is an urgent practical problem need to be resolved. The purpose of this chapter is to develop a new algorithm to obtain aerosol conditions; it includes haze identification, retrieval of AOT not only on hazy days but also in normal weather. A comprehensive discussion of the differences and limitations of this method compared with the C6 DT land algorithm is presented in this chapter as well. This chapter is based on Yan et al. (2016).

3.2 Data and methods

3.2.1 Study area

The North China Plain is the largest alluvial plain in China, with an area of 409,500 km^2, as shown in Figure 3.1. The region includes Beijing, Tianjin, and Hebei, whose gross domestic product accounted for 11.3% of China's GDP in 2007. With the development of urbanized construction, the land cover in the North China Plain has changed markedly. Many main roads and residential buildings have been built to accommodate the increase in motor vehicles and in population. Even though the government has made great efforts to improve the environment, urban air pollution problems have become increasingly serious. Particulate matter levels are severe around the cities and continuous air-pollution episodes such as haze events are more frequent than in the past (Li et al., 2013).

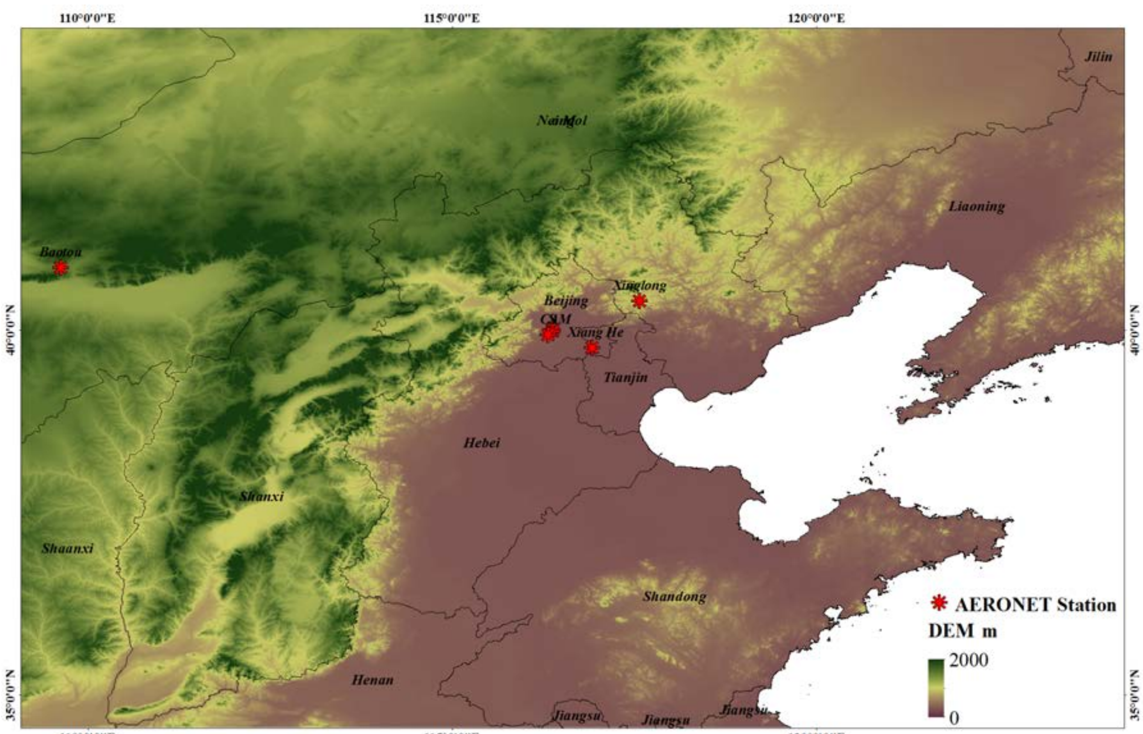

Figure 3.1: Study area of haze monitoring

3.2.2 Satellite data

Daytime MODIS TERRA satellite images were acquired[1] from December 2013 to June 2015, as shown in Table 3.1[2]. TERRA is a satellite launched in 1999 that passes from north to south over the study area every morning (ca. 10:30 a.m. local time); with 36 wavebands, it can be used for atmospheric, oceanic, and land studies at both global and local scales.

Collection 6 MODIS aerosol products (C6 MOD04) were obtained for this study, and C6 DT AOT with 10-km and 3-km resolution[3] were used as a comparison. In addition, MODIS C6 DB AOT with 10-km resolution[4] was also obtained for comparison, which was filtered by quality assurance (QA)(Hsu et al., 2013; Sayer et al., 2013). The C6 cloud mask data (Aerosol_Cldmsk_Land_Ocean) were extracted from MOD04 and used for cloud detection in our algorithm.

The MODIS Albedo product (MCD43) was also acquired. It provides data describing both directional hemispherical reflectance (black-sky albedo) and bi-hemispherical reflectance (white-sky albedo). The MCD43A1 Bidirectional Reflection Distribution Function (BRDF)/Albedo Model Parameters Product provides the weighting parameters associated with the Ross ThickLiSparse Reciprocal BRDF model. These three parameters (fiso, fvol, and fgeo) are provided for each of the MODIS spectral bands. In this study, fiso, fvol, and fgeo in Bands 1 and 3 were collected to calculate surface reflectance.

[1] https://ladsweb.nascom.nasa.gov/data/search.html

[2] BJ = Beijing AERONET station; BR = Beijing-RADI AERONET station; BC = Beijing−CAMS AERONET station; XL = Xinglong AERONET station; XH = Xiang He AERONET station; BT = AOE Baotou AERONET station

[3] Optical_Depth_Land_And_Ocean

[4] Deep_Blue_Aerosol_Optical_Depth_550_land_Best_Estimate

Table 3.1: The MODIS data used for haze monitoring

Date	Month	Year	AERONET Station	Date	Month	Year	AERONET Station
11	12	2013	BJ, BR,BC	16	10	2014	BR,XH
12	12	2013	BJ, BR	17	10	2014	BC,BR
14	12	2013	BJ,BR	18	10	2014	BJ,BC,BR,XH
26	12	2013	BJ,BR	25	10	2014	BC,BR,BT,XH
28	12	2013	BJ,BR	13	11	2014	BJ,BC,BR
30	12	2013	BJ,BR,BC	17	11	2014	BJ,BR,BC
1	1	2014	BJ,BR	22	11	2014	BJ,BR,BC
3	1	2014	BJ,BR,BC	26	11	2014	BJ,BC,BR,XH
13	1	2014	BJ,BR,BC	1	12	2014	BR,BC
22	1	2014	BJ,BR,BC	3	12	2014	BR,BC
3	2	2014	BJ,XH	17	12	2014	BJ,BR
4	2	2014	BJ,BR	24	12	2014	BJ,BR,BC
27	2	2014	BR,XH	31	12	2014	BJ,BR,BC
2	3	2014	BR,XH	2	1	2015	BJ,BR,BC
14	3	2014	BJ,BR	6	1	2015	BJ,BC
22	3	2014	BJ,XH	11	1	2015	BJ,BR,BC
7	4	2014	BJ,XH	27	1	2015	BJ,BC
2	5	2014	BJ,BC,XH	30	1	2015	BJ,BR,BC
7	5	2014	BJ,BC,XH	5	2	2015	BJ,BR,BC
16	5	2014	BJ,XH	17	2	2015	BJ,BR,BC
18	5	2014	BJ,XH	26	2	2015	BJ,BR,BC
3	6	2014	BJ,BC	3	3	2015	BJ,BR,BC
12	6	2014	BJ,BC	11	3	2015	BR,BC
27	6	2014	BJ,BC	21	3	2015	BJ,BC
28	6	2014	BJ,XH	23	3	2015	BC,XH
5	7	2014	BJ,BC,XH	21	4	2015	BC,XH
6	7	2014	BJ,BC,XH	22	4	2015	BC,XH
10	7	2014	BJ,BC	24	4	2015	BJ,BR,BC
12	7	2014	BJ,BC	26	4	2015	BR,BC
15	8	2014	BJ,BC	4	5	2015	BJ,BR,BC
25	8	2014	BC,XH	7	5	2015	BJ,BR,BC
3	9	2014	BR,BC	19	5	2015	BJ,BR,BC
8	9	2014	BJ,BR,BC	26	5	2015	BJ,BR,BC
9	9	2014	BJ,BR	2	6	2015	BR,BC
15	9	2014	BJ,BR	8	6	2015	BJ,BC
9	10	2014	BC,BR,BT,XH	18	6	2015	BJ,BR,BC
10	10	2014	BC,BR,BT,XH				

3.2.3 Enhanced haze aerosol retrieval algorithm (EHARA)

A new method is described here for haze monitoring and AOT retrieval based on MODIS data. This algorithm is designed for application in large areas characterized by the complex land surfaces of cities or dense vegetation. A schematic diagram of this method is shown in Figure 3.2. The central idea of this algorithm is dependent on the spectral characteristics received by a satellite to detect haze, and it then uses an aerosol model to calculate AOT. In this method, haze detection rules of MODIS image is based on Table 1 in Li et al. (2013).

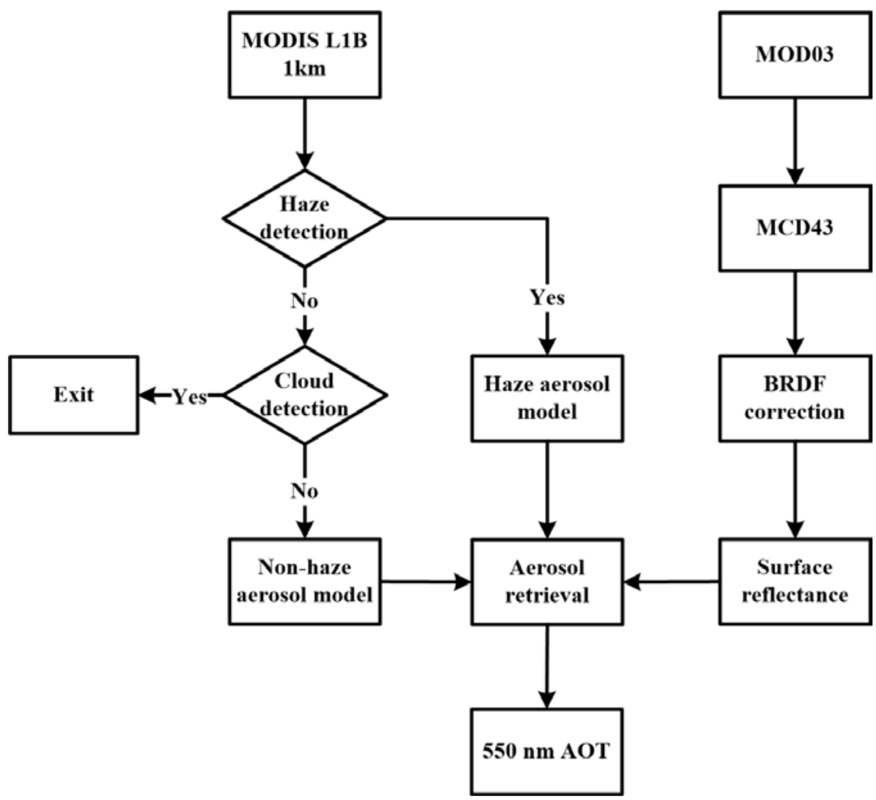

Figure 3.2: Schematic diagram for the EHARA

Initially MODIS L1B data have a gas-absorption correction, as does the latest C6 method, based on Appendix A in Levy et al. (2013). The EHARA is described as follows. The MODIS−measured TOA spectral reflectance can be estimated by (Drury et al., 2008):

$$\rho_{TOA(\lambda)}(\theta_0, \theta, \phi) = \rho_{Aer}(\theta_0, \theta, \phi) + \rho_{Ray}(\theta_0, \theta, \phi) + \frac{T_{(\theta_0)} T_{(\theta)} \rho_s(\theta_0, \theta, \phi)}{1 - \rho_s(\theta_0, \theta, \phi) S_{(\lambda)}} \quad (3.1)$$

where θ_0 is the solar zenith, θ is the sensor view zenith, and ϕ is the relative azimuth angle, $\rho_{Aer}(\theta_0, \theta, \phi)$ is the aerosol reflectance, $\rho_{Ray}(\theta_0, \theta, \phi)$ is the Rayleigh reflectance for molecules, $T_{(\theta_0)}$ and $T_{(\theta)}$ are the downward and upward total scattering transmittances, and $S_{(\lambda)}$ is the atmospheric backscattering ratio. $T_{(\theta_0)}$ and $T_{(\theta)}$ are defined by:

$$\left.\begin{aligned} T_{(\theta_0)} &= \exp\left[\tfrac{-(\tau_R + \tau_a)}{\mu_s}\right] + t_d(\mu_s) \\ T_{(\theta)} &= \exp\left[\tfrac{-(\tau_R + \tau_a)}{\mu_v}\right] + t_d(\mu_v) \end{aligned}\right\} \quad (3.2)$$

where μ_s is the cosine of the solar zenith angle, μ_v is the cosine of the sensor zenith angle and τ_a is the AOT. τ_R is the Rayleigh optical depth, which can be calculated as follows:

$$\tau_R = 0.00864 \lambda^{-(3.916 + 0.074\lambda + \frac{0.05}{\lambda})} \quad (3.3)$$

where $t_d(\mu)$ is the diffuse transmittance and can be well approximated by (Liu and Liu, 2009; Tanré et al., 1979):

$$t_d(\mu) = \exp(-(\tau_R + \tau_a)/\mu)\{\exp[(0.52\tau_R + \tau_a(1+g)/2)/\mu] - 1\} \tag{3.4}$$

For the atmospheric backscattering ratio $S_{(\lambda)}$, it can be approximated by:

$$S_\lambda = (0.92\tau_R + (1-g)\tau_a) \exp\left[-(\tau_R + \tau_a)\right] \tag{3.5}$$

in which g is the asymmetry factor (AF).

$\rho_{Aer}(\theta_0, \theta, \phi)$ is the aerosol reflectance in the absence of air molecules, which results from single scattering; it can be approximated by (Antoine and Morel, 1998):

$$\rho_{Aer}(\theta_0, \theta, \phi) = \frac{\omega_0 \tau_a P_a(\theta_0, \theta, \phi)}{4\mu_s \mu_v} \tag{3.6}$$

where ω_0 is the single scattering albedo (SSA), $P_a(\theta_0, \theta, \phi)$ is the aerosol scattering phase function as (Rahman, Pinty, and Verstraete, 1993):

$$P_a(\theta_0, \theta, \phi) = \frac{1 - g^2}{[1 + g^2 - 2g\cos(\pi - \Theta)]^{\frac{3}{2}}} \tag{3.7}$$

Then, the Rayleigh reflectance for molecules $\rho_{Ray}(\theta_0, \theta, \phi)$ can be approximated by:

$$\rho_{Ray}(\theta_0, \theta, \phi) = \frac{\omega_R \tau_R P_R(\theta_0, \theta, \phi)}{4\mu_s \mu_v} \tag{3.8}$$

where ω_R is the Rayleigh single-scattering albedo; in this study, $\omega_R \approx 1$.

$P_R(\theta_0, \theta, \phi)$ is the Rayleigh scattering phase function as (Levy et al., 2007):

$$P_R(\theta_0, \theta, \phi) = \frac{3}{4}(1 + \cos^2(\Theta)) \tag{3.9}$$

with

$$\Theta = \cos^{-1}(-\cos(\theta_0)\cos(\theta) + \sin(\theta_0)\sin(\theta)\cos(\phi)) \tag{3.10}$$

Thus, AOT (τ_a) can be calculated by:

$$\tau_a = \frac{4\mu_s \mu_v \left\{ \rho_{TOA(\lambda)} - \frac{\omega_R \tau_R P_R}{4\mu_s \mu_v} - \frac{T_{(\theta)} T_{(\theta_0)} \rho_s}{1 - \rho_s [0.92\tau_R + (1-g)\tau_a] exp[-(\tau_R + \tau_a)]} \right\}}{\omega_0 P_a} \tag{3.11}$$

In Equation 3.11, the surface reflectance (ρ_s) is a key parameter in the aerosol retrieval algorithm. In this study, surface reflectance was calculated by MCD43 at corresponding MODIS L1b data angles (Roujean, Leroy, and Deschamps, 1992). In EHARA, we used the single-scatter approximation for aerosol reflectance as Equation 3.6 and Equation 3.7 and a BRDF assumption for surface reflectance. Then EHARA combined these with a multiple-scattered light equation over a Lambertian surface as Equation 3.1.

However, it should be noted that the physical assumptions in EHARA are not as self-consistent as DB and DT which with a full radiative transfer model.

3.2.4 Aerosol model

The aerosol model varies significantly in different areas and seasons. The SSA and the asymmetry factor (AF) are two key parameters in determining aerosol physical properties. The SSA and AF may differ for each pixel in MODIS data due to large coverage (Drury et al., 2008). Thus, in this study, we determined the SSA and AF values for each pixel from the nearest AERONET station (Table 3.1). If the nearest AERONET station's measurements were under hazy conditions, the non-hazy areas used empirical SSA and AF values based on last years mean value in the corresponding season. On the other hand, if the nearest AERONET station's measurements were under non-hazy conditions, the hazy areas were assigned empirical SSA and AF values, as will be discussed in detail in 3.3.1.

3.3 Results

3.3.1 Haze aerosol model

To obtain empirical SSA and AF values for haze aerosol retrieval, 12−yr (2002−2014) AERONET data for hazy days in Beijing were collected. Figure 3.3 shows SSA values at 440 nm and 675 nm under hazy conditions. It is evident that 675-nm SSA values are always higher than 440-nm SSA values, which means that aerosol particles are more strongly scattered at

675 nm on hazy days. From 2002 to 2006, SSA was low in these two wavelengths. Lee, Kim, and Kim (2006) also found that the haze aerosol had a large absorption (SSA = 0.88) with black carbon particles in October 2004. After 2007, the SSA values at 675 nm (total mean SSA at 675 nm) were generally above 0.90, with the highest mean value of 0.95 in 2012, which approximates to the dust model in the MODIS retrieval algorithm (Levy et al., 2010). The mean SSA value at 440 nm in these years was always between 0.89 and 0.91, which was a little higher than the total mean value of 0.89. The SSA values increase when the haze aerosol displays more scattering and the secondary aerosols include both sulfate and nitrate (Yan et al., 2008). Thus, the empirical SSAs for the haze aerosol model in this study were 0.9 (blue band) and 0.92 (red band), values that are consistent with the results of previous studies (Noh et al., 2009; Tao et al., 2013; Tao et al., 2014). It is interesting that SSA has been higher over Beijing area in recent years. Yu et al. (2012) found that from 2002 to 2008, the mean values of haze SSA were 0.91 (675 nm) and 0.89 (440 nm). And in the normal days, Bergin et al. (2001) indicated that SSA over Beijing in 1999 was 0.81 and Mao and Li (2006) showed that the mean SSA was 0.79 in 2003.

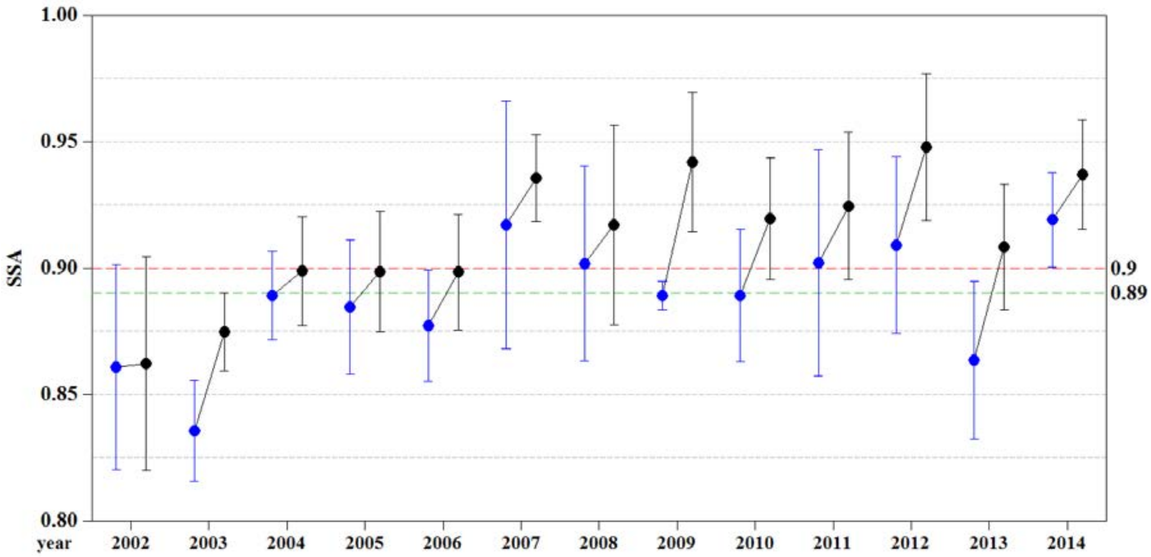

Figure 3.3: Interval plot of haze SSA from 2002 to 2014 (95% confidence interval; the black points are SSA at 675 nm wavelength; the blue points are SSA at 440 nm wavelength; the red dashed line is the mean SSA at 675 nm over the 12 years, and the green dashed line is the mean SSA value at 440 nm over the 12 years)

Figure 3.4 shows the AF variation at 440 nm and 675 nm, clearly showing that AF values were higher at 440 nm than at 675 nm, and always ranged from 0.69 to 0.71, which approximates to the total mean value of 0.7. AF mean values were always between 0.65 and 0.66, similar to the 12-yr mean value of 0.66. Therefore, the empirical AF in this study was 0.71 for the blue band and 0.67 for the red band (Tanré et al., 1979).

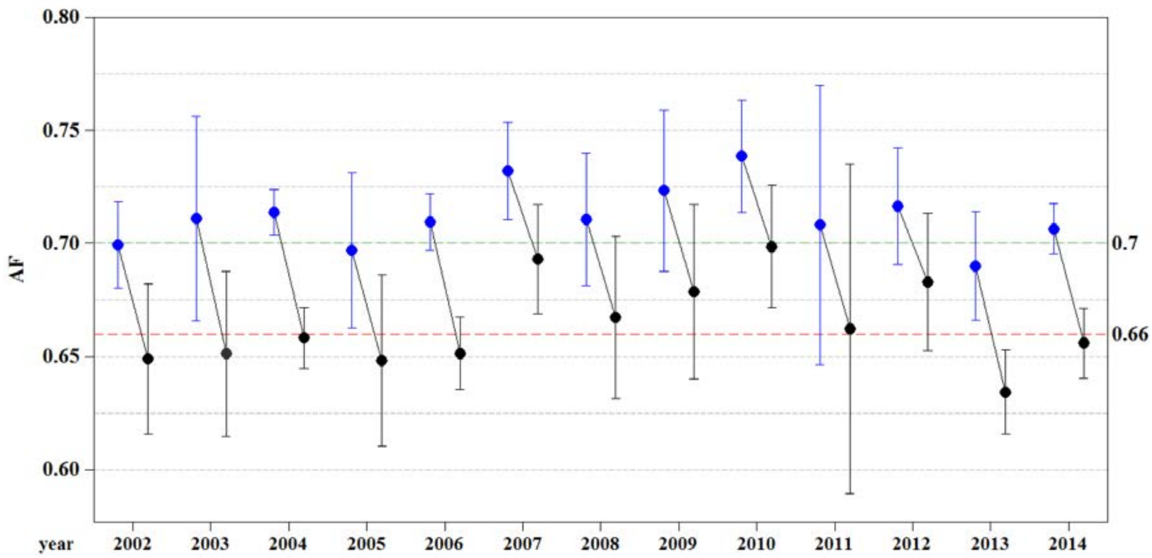

Figure 3.4: Interval plot of haze AF values from 2002 to 2014 (95% confidence interval; the black points are AF at 675 nm wavelength; the blue points are AF at 440 nm wavelength; the red dashed line is the mean AF value at 675 nm over the 12 years, and the green dashed line is the mean AF value at 440 nm over the 12 years)

3.3.2 Haze aerosol optical thickness retrieval

To illustrate the outcomes of the EHARA, we use three retrieval results as examples. The first case is under heavy haze conditions. Figure 3.5A is a true-color satellite image taken on 9 October 2014, which shows significantly different colors that distinguish heavy haze and cloud. Generally, clouds are white and haze appears gray. The haze mark based on Li et al. (2013) is shown in Figure 3.5B with extensive coverage over Beijing, Hebei, and Shanxi. Figure 3.5F presents the EHARA 1-km AOT spatial distribution for the same day, revealing a high haze aerosol-loading event over the North China Plain. High AOT values (2.5-3) are evident between Beijing and Hebei due to the local topography, which forms a bowl ringed by mountainous terrain (Yanshan and Taihang mountains) in the west (Lee, Kim, and Kim, 2006). When the atmospheric structure is stable, air masses are easily blocked by these mountains, which leads to haze accumulation.

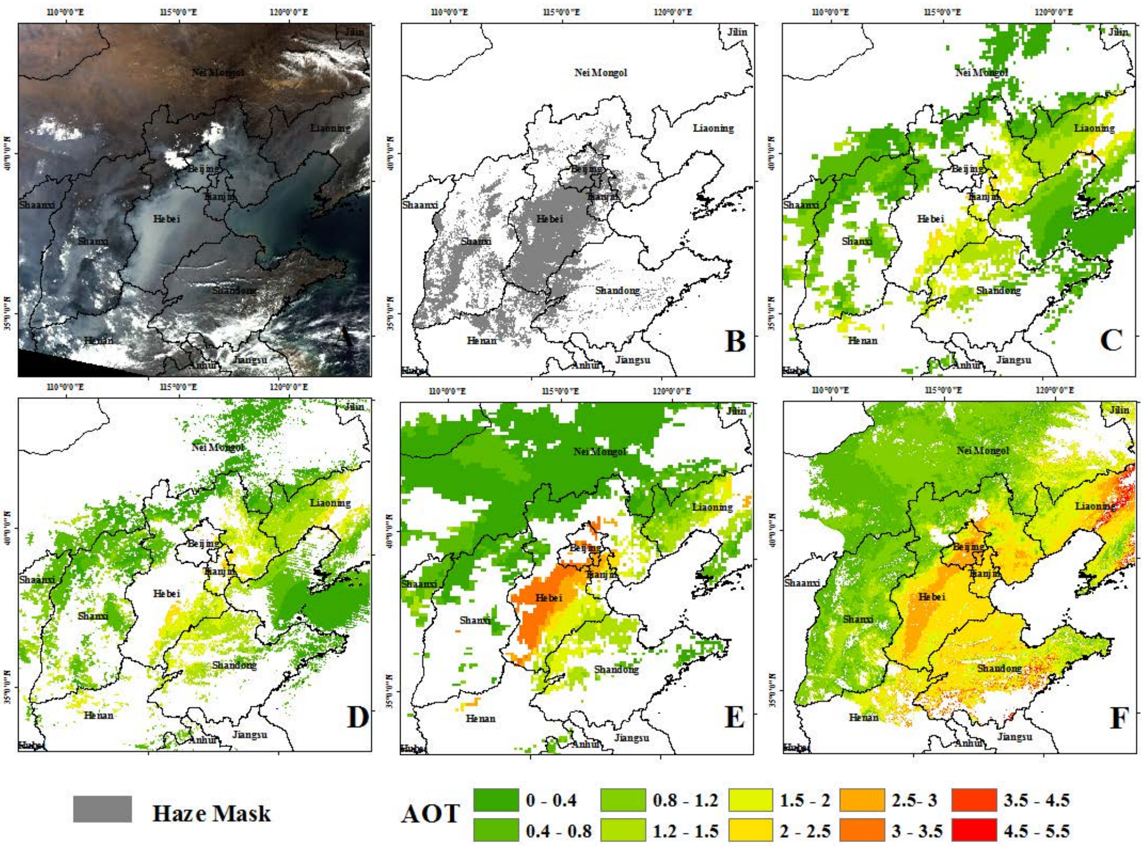

Figure 3.5: (A) True-color MODIS image taken on 9 October 2014. (B) Result of haze identification. (C) MODIS C6 DT 10-km AOT. (D) MODIS C6 3-km AOT. (E) MODIS C6 DB 10-km AOT. (F) EHARA 1-km AOT.

The second case is a hazy day with cloud. Figure 3.6A shows cloudy weather conditions over the North China Plain on 5 July 2014. Haze detection revealed scattered haze pixels that covered a wide, area including Beijing, Tianjin, Hebei, Shanxi, Henan, and Shandong (Figure 3.6B). Figure 3.6F shows the high aerosol values (AOT: 4-5.5) over the Beijing, Liaoning, Hebei, and Shandong regions, where values were much higher than in the northwestern areas (AOT: 0.2-0.4).

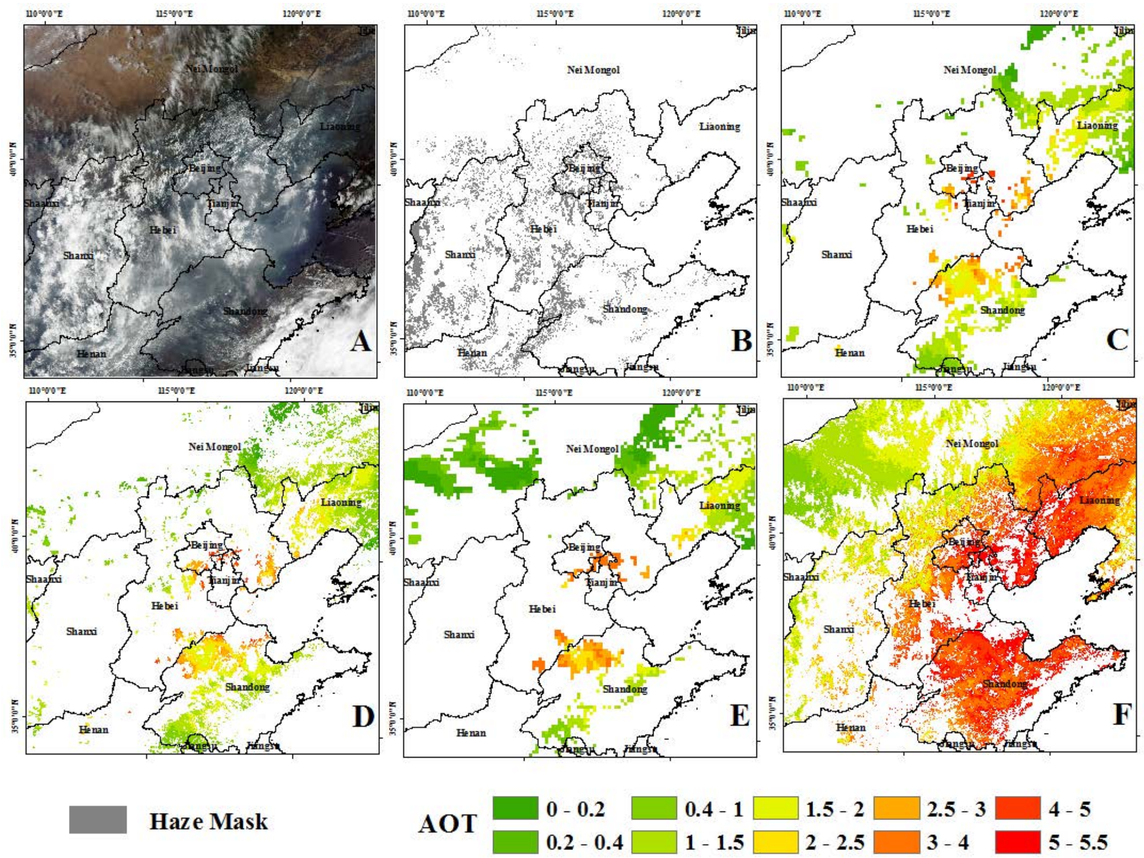

Figure 3.6: (A) True-color MODIS image on 5 July 2014. (B) Result of haze identification. (C) MODIS C6 DT 10-km AOT. (D) MODIS C6 3-km AOT. (E) MODIS C6 DB 10-km AOT. (F) EHARA 1-km AOT.

The third case is under normal weather condition on 16 October 2014. The true-color satellite image shows a fine and cloud-free day on the North China Plain (Figure 3.7A). No haze pixels were detected, indicating good weather conditions (Figure 3.7B). Figure 3.7F shows that high AOT values were observed in southeastern areas with high population densities, with low AOT values in the western region with high elevations and dense vegetation. These AOT spatial characteristics are consistent with previous research (Guo et al., 2012; Luo et al., 2015).

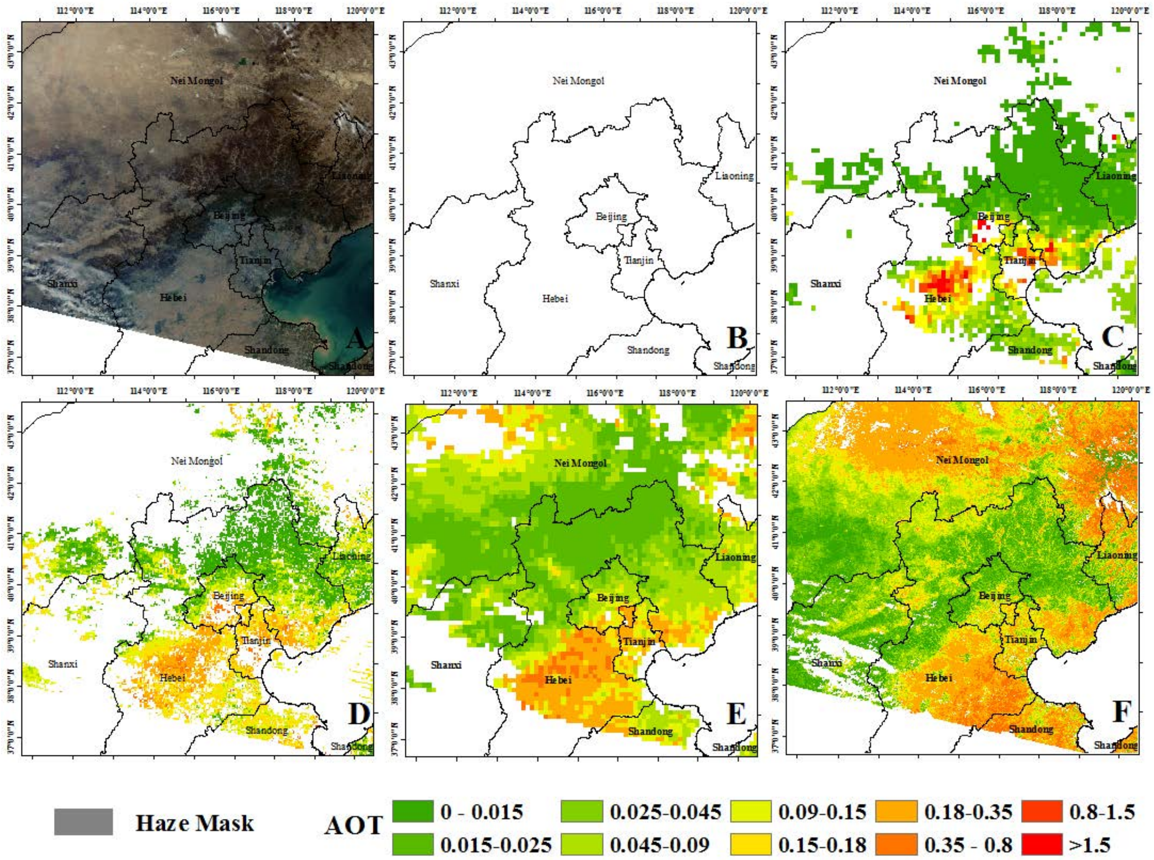

Figure 3.7: (A) True-color MODIS image on 16 October 2014. (B) Results of haze identification. (C) MODIS C6 10-km AOT. (D) MODIS C6 3-km AOT. (E) MODIS C6 DB 10-km AOT. (F) EHARA 1-km AOT.

3.3.3 Validation

Figure 3.8 presents the validation result of EHARA AOT, MODIS C6 DB 10-km AOT, MODIS C6 DT 10-km AOT, and MODIS C6 DT 3-km AOT with AERONET AOT. 88 AERONET measurements at 550 nm AOT (interpolated by 675 nm and 440 nm) from 2 AERONET stations Beijing and Xianghe with Level 2 data were collected over the course of ± 2 to 30 min when satellite overpasses. The dotted red line is the estimated error envelope line $\pm(0.05 + 0.15_{AERONETAOT})$, and the solid red line is the 1:1 line. Figure 3.8A compares EHARA AOT with AERONET measurements, showing the close correspondence between them. The EHARA AOT misses 3.4% of data, and the majority of the observations (73%) are within the error range $\pm(0.05 + 0.15_{AERONET\,AOT})$, which indicates that the retrieved AOT values are of good quality. Good agreement was also observed for the MODIS C6 DB AOT as most of data points lie close to the 1:1 line (Figure 3.8C). It has 68% data within the error range and 9% data is missed. However, for the DT AOT products, 43% of 10-km AOT and 38% of 3-km AOT are missed in this study. In the MODIS DT 3-km AOT, only 53% of the data are within the error range line, while the 10-km AOT is 66%. Remer et al. (2013) also found that the 3-km AOT product matches AERONET less well than the 10-km product. Furthermore, Munchak et al. (2013) indicated that the performance of the 3-km AOT product is poor especially over urban surfaces, which clearly suggests a limitation for air quality applications as well.

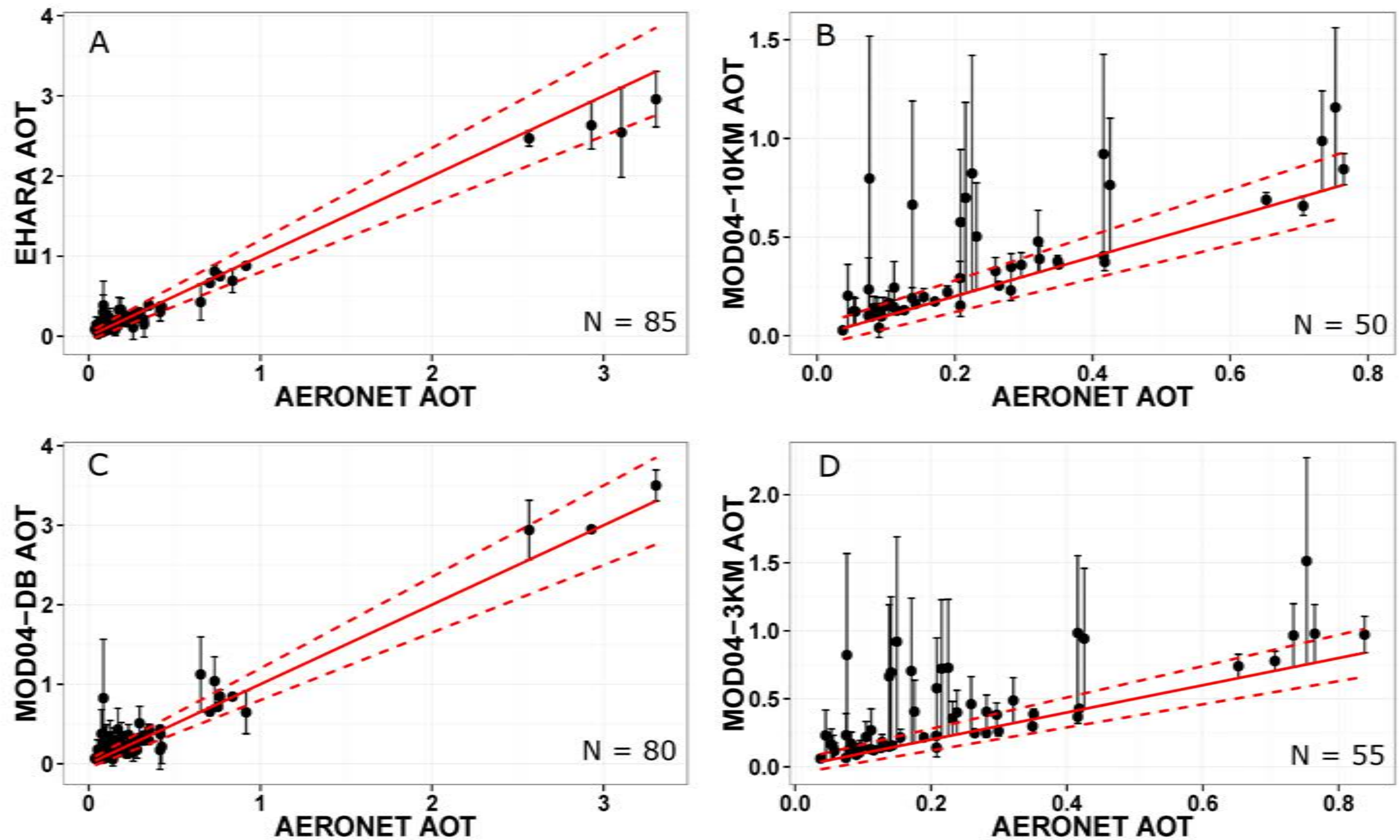

Figure 3.8: Validation of AOT against AERONET (A: EHARA 1-km AOT, B: C6 DT 10-km AOT, C: C6 DB 10-km AOT, D: C6 DT 3-km AOT. Two error lines are y=1.15x+0.05 and y= 0.85x−0.05, which correspond to the error $\Delta\tau = \pm\,(0.05 + 0.15_{AERONET\,AOT})$

3.4 Comparison and discussion

As shown in Figure 3.5 and Figure 3.6, the EHARA AOT had better spatial coverage than the MOD04 DT AOT products. Especially under hazy conditions, the MODIS DT aerosol products missed most values. Tao et al. (2012) found that the MODIS DT AOT could not provide a full retrieval due to haze clouds over the North China Plain, which led to an underestimation of the haze aerosol loading. Because in Section 3.3.3 the MODIS DB AOT also shows a good performance, thus we only focus on the comparison between the EHARA and MODIS DT AOT.

3.4.1 Surface reflectance assumptions

The C6 updates of the DT algorithm include refinements and code bug fixes, but they are based on the same principles as the C5 version (Sayer et al., 2014). The C6 still uses the VISvs2.1 surface reflectance parameterization with NDVIswir dependence (Levy et al., 2013), which is described in Levy et al. (2007). However, hazy days with thick aerosols make the VISvs2.1 surface reflectance relationship inappropriate (Wang et al., 2010a). From Figure 3.9, the NDVIswir for hazy days has a mean value of 0.381, which is significantly higher than that for non-hazy days (0.325). As presented in Equation (8) to (10) in Levy et al. (2007), NDVIswir is the most important parameter for the calculation of surface reflectance. In hazy weather, overestimation of NDVIswir can lead to large errors in estimates of the surface reflectance of hazy pixels. Kaufman et al. (1997) indicated that an error of 0.01 in surface reflectance can lead to an error of 0.1 in retrieved AOT values. Thus, the EHARA uses MCD43 BRDF parameters to calculate surface reflectance. As shown in Figure 3.1, most elevations in the North China Plain are of less than 50 m, resulting in a low BRDF effect in the majority of urban areas. Li et al. (2013) showed that between March and September, both mountain and urban areas have low surface reflectance and show small non-Lambertian behavior in the North China Plain; thus, errors in surface reflectance using MCD43 are likely to be less than 0.03.

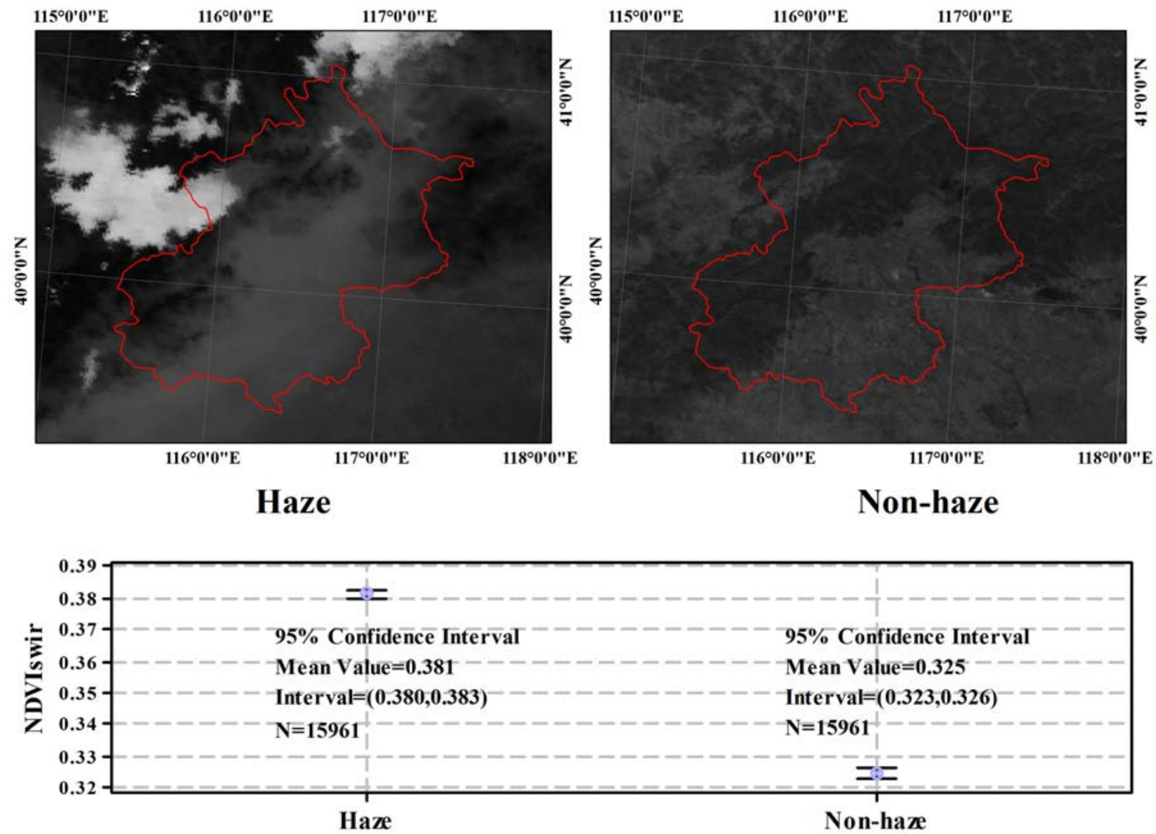

Figure 3.9: NDVIswir on hazy and non-hazy days.

3.4.2 Null data pixels

There are null data in almost every MODIS AOT image, which limit the inversion of ground-based air data like PM2.5 and PM10 values. Here some brief reasons are presented for the C6 DT land algorithm to illustrate why the significant Null Data problem exists. A big reason for data gaps is cloud and snow cover. Second, in the C6 DT land algorithm, dark pixels are first selected based on 2.13-μm reflectance; fine- and coarse-mode aerosol-type LUTs are built and corrected for elevation. The LUT simulations are indexed by seven values at 550 nm AOT, which are 0.0, 0.25, 0.5, 1.0, 2.0, 3.0, and 5.0 (Levy et al., 2010). Then the inversion is conducted at 2.12-, 0.66-, and 0.47-μm wavelengths: the path and surface reflectance are a function of $\tau(0.55\ \mu\text{m})$, and this part of the algorithm attempts to find the surface reflectance at 2.12 μm and the value of τ. Although this should match the 0.47-μm band, the 0.66-μm band may have errors. Thus, the solution is found when the error at 0.66 μm is minimized. The exact procedure is shown as Equation 3.12, Equation 3.13 and Equation 3.14. The calculated error evaluates the AOT retrieval result and an indicator (quality assessment, QA) is set from 0 to 3. For example, if ε is more than 0.25, QA confidence will be set at 0. As for some pixels in hazy conditions, integrated using Equation 3.12 and Equation 3.14, Equation 3.13 is solved and an extremely low ${\rho^*}_{0.66}$ value is obtained compared with ${\rho^m}_{0.66}$, which causes ε to exceed the limitation (0.25), and MOD04 of Optical_Depth_Land_And_Ocean only presents data of specific quality (QA confidence flag= 3).

$$ {\rho^{\mathrm{m}}}_{0.47} - {\rho^*}_{0.47} = 0 \tag{3.12} $$

$$ {\rho^{\mathrm{m}}}_{0.66} - {\rho^*}_{0.66} = \varepsilon \tag{3.13} $$

$$ {\rho^{\mathrm{m}}}_{2.12} - {\rho^*}_{2.12} = 0 \tag{3.14} $$

where ${\rho^*}_{0.47}$, ${\rho^*}_{0.66}$ and ${\rho^*}_{2.12}$ are the calculated spectral total reflectance values at the top of the atmosphere, which are the weighted sums of the spectral reflectance from fine- and coarse-dominated models; ${\rho^m}_{0.47}$, ${\rho^{\mathrm{m}}}_{0.66}$ and ${\rho^m}_{2.12}$ are the MODIS measured reflectance values. Third, the C6 DT algorithm includes a thin-cirrus test to determine clouds which may lead to aerosol contamination. Pixels with $\rho_{1.38} > 0.01$ are deemed to be thin cirrus and the QA confidence of these pixels is then reduced to zero. The C6 also updates the code such that AOT values close to a cloudy area are not retrieved. For example, as shown in Figure 3.6A and Figure 3.6B, hazy weather is usually accompanied by clouds; thus, C6 may miss haze aerosol retrieval in areas of thin cirrus or close to clouds.

Several null data AOT pixels may be acquired using the EHARA method, as shown in Figure 3.10B. The reason is that aerosol ($\rho_{Aer}(\theta_0, \theta, \phi)$) and Rayleigh reflectance ($\rho_{Ray}(\theta_0, \theta, \phi)$) are obtained by experience formulas Equation 3.6 and Equation 3.8, which may lead to the equation[5] < 0 in some pixels. This may be related to the influence of weather and viewing angle. Nevertheless, this phenomenon is significantly less evident than in MODIS DT aerosol products, as shown in Figure 3.10B and Figure 3.10D

[5] $\rho_{_{TOA(\lambda)}}(\theta_0, \theta, \phi) - \rho_{Aer}(\theta_0, \theta, \phi) - \rho_{Ray}(\theta_0, \theta, \phi)$

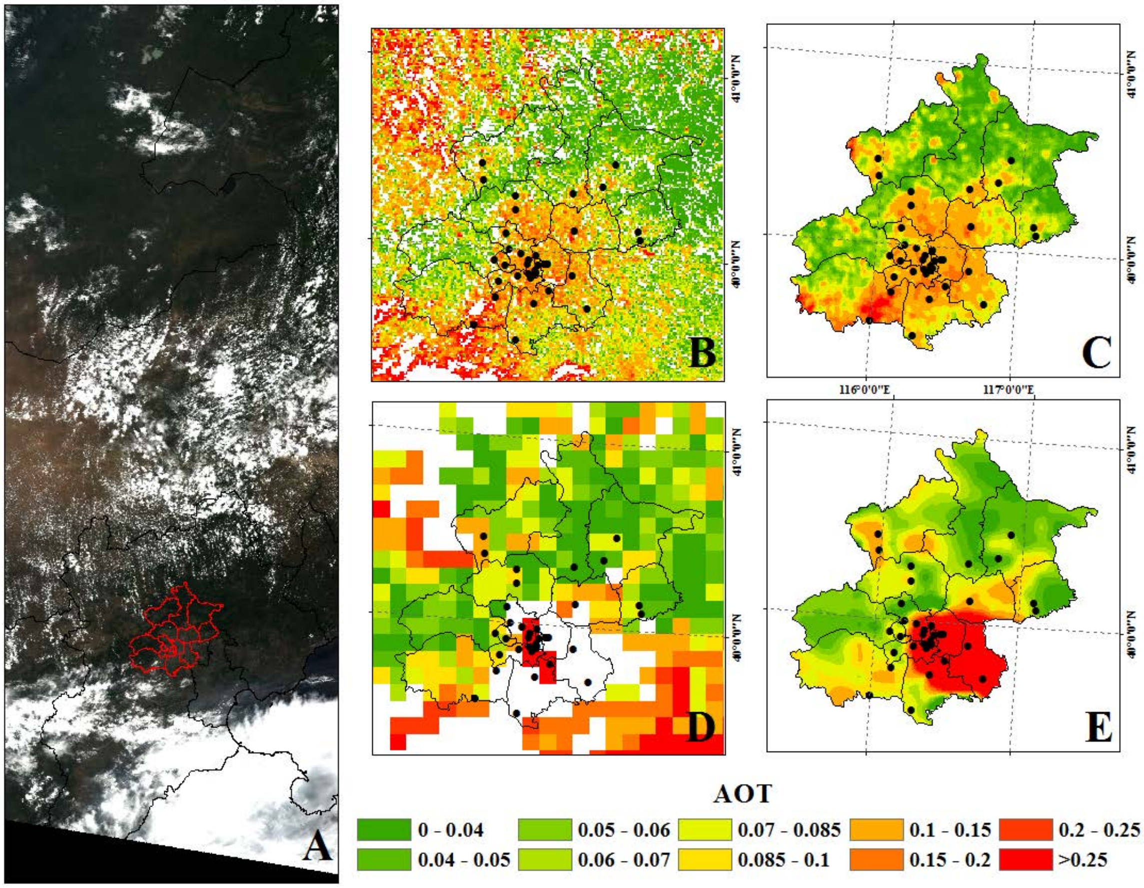

Figure 3.10: (A) True-color MODIS image on 12 July 2014. (B) EHARA AOT values. (C) Interpolation of EHARA AOT and (D) MODIS C6 DT 10-km AOT values. (E) Interpolation of MODIS C6 DT 10-km AOT values (black dots are Beijing environmental monitoring stations).

3.4.3 Differences in Aerosol Models

The C6 aerosol products have been updated with new aerosol type selections; however, their overall spatial distribution remains the same as defined for the C5 version (Levy et al., 2013). The weakly absorbing (SSA = 0.95) and the moderately absorbing (SSA = 0.91) aerosol models in C6 are generally adopted for the North China Plain (Levy et al., 2010). However, the EHARA uses intraday AERONET SSA to retrieve AOT. Another issue for the MODIS DT land retrieval algorithm is that it often selects the dust aerosol model over land areas where dust is unlikely to be found. This is especially likely when AOT values are small (Mielonen et al., 2011).

3.4.4 Application to air quality assessment

To assess air pollution levels at large scales, the relationship between satellite-based AOT values and ground-based air-pollution data, including air quality index (AQI) PM2.5 and PM10 values, is useful. However, as shown in Figure 3.10D, the C6 aerosol products omit a number of the Beijing environmental monitoring stations, which obstructs the spatial assessment of air pollution and the mapping of air quality. To solve this problem, interpolation is conducted, as shown in Figure 3.10E. Nevertheless, it is clear that the resulting AOT spatial distribution differs from that in Figure 3.10C. The inappropriate interpolation is due to the large number of missing values southeast of Beijing. Thus, the null data limit the application of the C6 aerosol products for air quality assessment. Additionally, the contrast between Figures 3.10B and 3.10D indicates that EHARA AOT values are more spatially complete than the C6 AOT values. Figure 3.10B and Figure 3.10C show that using interpolation for the null EHARA AOT data results in almost the same spatial distribution as the original data. Moreover, most importantly, the EHARA can provide better performance for AOT values on hazy days and result in more appropriate air quality assessment. Another problem for the C6 AOT application is that of output of negative values. It should be noted that the MODIS retrieval algorithm permits negative AOT values, and negative retrieval results are especially common on days with low-AOT values (Hyer, Reid, and Zhang, 2011).

3.5 Summary

In this chapter, MODIS measurements were used to develop an enhanced haze aerosol retrieval algorithm. This method can work not only on hazy days but also on normal weather days. Based on 12-year (2002-2014) AERONET aerosol property data, empirical single scattering albedo (SSA) and asymmetry factor (AF) values were chosen to assist haze aerosol retrieval. For validation, EHARA AOT values, along with MODIS Collection 6 dark-pixel and deep blue aerosol products, were compared with AERONET data. The results show that the EHARA can achieve greater AOT spatial coverage under hazy conditions with a high accuracy (73% within error range) and work a higher resolution (1-km). Additionally, this chapter presents a comprehensive discussion of the differences between and limitations of the EHARA and the MODIS C6 DT land algorithms.

Chapter 4

Fine mode aerosol-algorithm for determining the fine mode fraction

4.1 Introduction

Atmospheric aerosols generally have a bimodal distribution and the smaller particles are referred to as the fine mode aerosols, these aerosols are also known as fine particles. These particles have diameter between 0.2 and 0.5 microns. The larger particles comprise the coarse mode. Through previous research, from 2000 to 2010, the pollution of fine mode aerosol is worsening in central and eastern China (Wang et al., 2013). However, at present, FMF as a key parameter to calculate FM-AOT is still difficult to obtain by satellite data. Thus, the objectives of this chapter are to determine the possibility of simultaneously retrieving the FMF using MODIS images and to characterize their temporal and spatial distributions. This chapter proposes a method, the lookup table-based SDA (LUT-SDA), which is designed for satellite images based on only two wavelengths of AOT to solve the FMF problem.

4.2 Data and methods

4.2.1 Study area

This study was conducted in Beijing and the surrounding area. The city's elevation decreases gradually from west to east due to the distribution of mountains and plains (Figure 4.1). With the development of the capital city, including large areas of new construction, the land coverage in Beijing has changed markedly. Many main roads and residential buildings have been built to accommodate the increase in population, with a consequent increase in the number of motor vehicles. Even though the Beijing city government has made great efforts to improve the environment, urban air pollution problems have become increasingly serious.

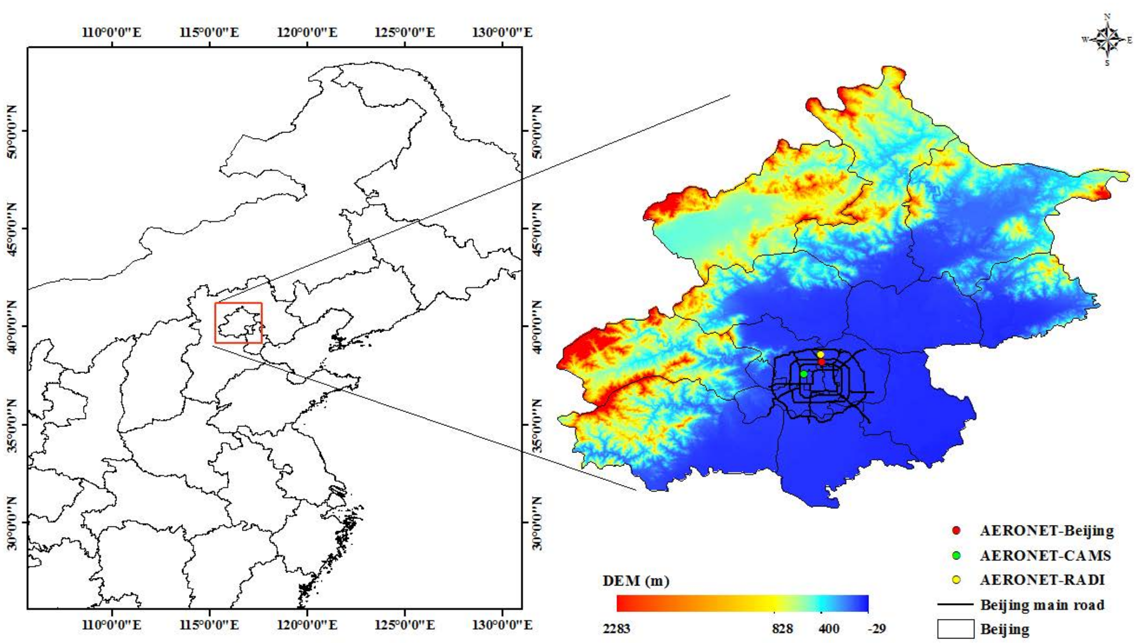

Figure 4.1: Study area

4.2.2 LUT-SDA

As showed in SDA (O'Neill, Dubovik, and Eck, 2001), it was developed as a simple and efficient method for calculating fine and coarse mode based on total AOT spectrum. The basic idea is that:

$$\tau_a = \tau_f + \tau_c \tag{4.1}$$

Where τ_a is total aerosol optical depth at a reference wavelength, τ_f is fine mode optical depth, τ_c is coarse mode optical depth. Angstrom exponent (AE) can be written as:

$$\alpha = -\frac{d \ln \tau_a}{d \ln \lambda} = \frac{\alpha_f \tau_f + \alpha_c \tau_c}{\tau_a} \tag{4.2}$$

Where Equation 4.2 is defined as a weighted function including fine and coarse mode terms. α is total Angstrom exponent at the wavelength of λ, α_f and α_c are fine and coarse mode Angstrom exponent.
The FMF (η) can be calculated by:

$$\eta = \frac{\tau_f}{\tau_a} \tag{4.3}$$

Applying Equation 4.3 to Equation 4.2:

$$\alpha = \alpha_f \eta + \alpha_c (1 - \eta) \tag{4.4}$$

Thus:

$$\eta = \frac{\alpha - \alpha_c}{\alpha_f - \alpha_c} \tag{4.5}$$

Defining t as a parameter:

$$t = \alpha - \alpha_c - \frac{\alpha' - {\alpha_c}'}{\alpha - \alpha_c} \tag{4.6}$$

Where α' is AE derivative, and ${\alpha_c}'$ is Angstrom exponent derivative of α_c. α_f can be using a simple expression:

$$\alpha_f = \frac{1}{2(1-\mathrm{a})}(\mathrm{t} + \mathrm{b}* + \mathrm{D}) + \alpha_c \tag{4.7}$$

Where

$$\left.\begin{aligned} \mathrm{D} &= \sqrt{(\mathrm{t} + \mathrm{b}*)^2 + 4(1-\mathrm{a})\mathrm{c}*} \\ \mathrm{b}* &= \mathrm{b} + 2\alpha_\mathrm{c}\mathrm{a} \\ \mathrm{c}* &= \mathrm{c} + (\mathrm{b} + \mathrm{a}\alpha_\mathrm{c})\alpha_\mathrm{c} - {\alpha_\mathrm{c}}' \end{aligned}\right\} \tag{4.8}$$

with

$$\left.\begin{aligned} a &= \left(a_{lower} + a_{upper}\right)/2 \\ b &= \left(b_{lower} + b_{upper}\right)/2 \\ c &= \left(c_{lower} + c_{upper}\right)/2 \end{aligned}\right\} \tag{4.9}$$

Where $a_{upper} = -0.22$, $a_{lower} = -0.3$, $b_{upper} = 10^{-0.2388}\lambda^{1.0275}$, $c_{upper} =$

$10^{0.2633}\lambda^{-0.4683}$, $c_{lower} = 0.63$.

In SDA, $\alpha_{\mathrm{c}} = -0.15$, ${\alpha_{\mathrm{c}}}' = 0$, τ_a, τ and α' can be derived from a second-order polynomial fit that $\ln \tau_a$ versus $\ln \lambda$ applied to each measured τ_a spectrum (at least 3 wavelength AOT), then η can be obtained. However, AOT retrieval by remote sensing image is always in blue and red band, which only has 2 wavelength AOT values. Thus, in order to use 2 wavelength AOT for FMF calculation, AE can be calculated by:

$$\alpha = -\frac{\ln(\frac{\tau_1}{\tau_2})}{\ln(\frac{\lambda_2}{\lambda_1})} \tag{4.10}$$

Embedded Equation 4.8 to Equation 4.7, then Equation 4.7 can be written as:

$$\begin{aligned}\alpha_{f1} = \tfrac{1}{2(1-\mathrm{a})}\{(\alpha - \alpha_c - \tfrac{\alpha' - {\alpha_c}'}{\alpha - \alpha_c} + \mathrm{b}*) + [(\alpha - \alpha_c - \tfrac{\alpha' - {\alpha_c}'}{\alpha - \alpha_c} + \mathrm{b}*)^2 \\ +4c * (1-a)]^{1/2}\} + \alpha_c\end{aligned} \tag{4.11}$$

And Equation 4.5 can be written as:

$$\alpha_{f2} = \frac{\alpha - \alpha_c}{\eta} + \alpha_c \tag{4.12}$$

Let η change from 0 to 1, and α' from -2 to 2 to build a look up table for Equation 4.11 and Equation 4.12, thus:

$$\left.\begin{aligned}(\eta^1, \alpha'^1) = \min(\alpha_{f1} - \alpha_{f2}) \\ \\ {\alpha_f}^1 = \tfrac{\alpha - \alpha_c}{\eta^1} + \alpha_c\end{aligned}\right\} \tag{4.13}$$

Where η^1, α'^1 and ${\alpha_f}^1$ are uncorrected estimate of η, α' and α_f. Finally, through α' bias error correction (Appendix A1) and the mean of extreme (MOE) modification (Appendix A2, same as SDA Version 4.1), η can be obtained.

4.2.3 AOT and AE retrieval from remote sensing data

AOT and AE are two key parameters for LUT-SDA, which can be directly influence FMF outcome. Bilal et al. (2013) proposed a Simplified Aerosol Retrieval Algorithm (SARA), and was successful applied and validated in Beijing (Bilal, Nichol, and Chan, 2014). SARA for calculating AOT as showed:

$$\tau_a = \frac{4\mu_s\mu_v}{\omega_0 P_a}\left[\rho_{_{TOA}} - \rho_{Ray} - \frac{e^{-(\tau_R+\tau_a)/\mu_s}e^{-(\tau_R+\tau_a)/\mu_v}\rho_s}{1-\rho_s(0.92\tau_R+(1-g)\tau_a)exp[-(\tau_R+\tau_a)]}\right] \tag{4.14}$$

Where τ_a is AOT, τ_R is the Rayleigh optical depth, $\rho_{_{TOA}}$ is satellite measured top of the atmosphere (TOA) reflectance, ρ_{Ray} is Rayleigh reflectance, ρ_s is surface reflectance (MOD09), μ_s is cosine of solar zenith angle, μ_v is cosine of sensor zenith angle, g is the asymmetry factor (AF). ω_0 is the single scattering albedo (SSA), P_a is the aerosol scattering phase function. Finally, AOT is obtained and AE can be calculated by Equation 4.10.

4.2.4 MODIS data

The MODIS Terra level 1B (MOD02HKM calibrated radiances and MOD03) and MODIS surface reflectance product (MOD09) were acquired from December 2013 to July 2015 in cloud free day. The obtained data MOD02HKM was for estimation TOA reflectance, MOD03 provided satellite and solar angles. MODIS MOD04 Collection 6 (C6) aerosol product was also obtained for comparison purpose. Dark-target (DT) algorithm based AOT at 550 nm and FMF were extracted from MOD04 C6. The C6 updates of the DT algorithm include refinements and code bug fixes, but they are based on the same principles as the C5 version (Sayer et al., 2014). The C6 still uses the VISvs2.1 surface reflectance parameterization with NDVIswir dependence (Levy et al., 2013), which is described in Levy et al. (2007).

4.2.5 AERONET

The AERONET program is a federation of ground-based remote sensing aerosol networks (Holben et al., 2001). AERONET collaboration provides globally distributed observations of spectral AOT, inversion products, and other AOT-dependent products. Aerosol optical depth data are computed for three data quality levels: Level 1.0 (unscreened), Level 1.5 (cloud-screened), and Level 2.0 (cloud-screened and quality-assured). In this study, three AERONET stations were used as showed in Figure 1, they were located in Beijing city area (Beijing, CAMS and RADI). AOT and FMF were obtained by these AERONET site Beijing (level 2), CAMS and RADI (level 1.5).

4.3 Results and discussion

4.3.1 LUT-SDA and optimal for satellite images

The LUT used in the LUT-SDA is shown in Figure 4.2. The solid line represents the FMF (η) , with constant values (0.1 to 1, scale = 0.2). The dashed line represents the AE derivative, with constant values (-2 to 2, scale = 1, the dashed line of the AE derivative with 1 and 2 is short, and very close to 0, and therefore the solid line is not annotated in Figure 4.2). Utilizing the LUT-SDA, we found that the AE derivative (α') had a great influence on the retrieved FMF. The range and scale of the AE derivative in the LUT are key factors for the FMF. Of course, the finer the scale, the more accurate the AE derivative is. However, for satellite images, a fine scale and large range of the AE derivative will substantially increase the calculation time. Thus, for the satellite data, a reliable method with less running time is necessary. In AERONET, the daily AE derivative from 2009 to 2012 was obtained (Figure 4.3). It can be found that the daily AE derivative ranges from -1.2 to 1.2 accounting for most phenomenon in Beijing. Thus, in this study, the AE derivative is set the range from -1.2 to 1.2 with scale 0.001 for LUT to calculate satellite FMF (η is set the range from 0 to 1 with scale 0.01). To validate the LUT-SDA performance, we used the AERONET 500 nm AOT and AE from January 2013 to June 2013 as input data to calculate the FMF, and the outcomes were then compared with the AERONET FMF (500 nm). Figure 4.4 shows the comparison of the LUT-SDA FMF, it can be found that the LUT-SDA FMF matched the AERONET FMF well, and can provide accurate and reliable outcomes.

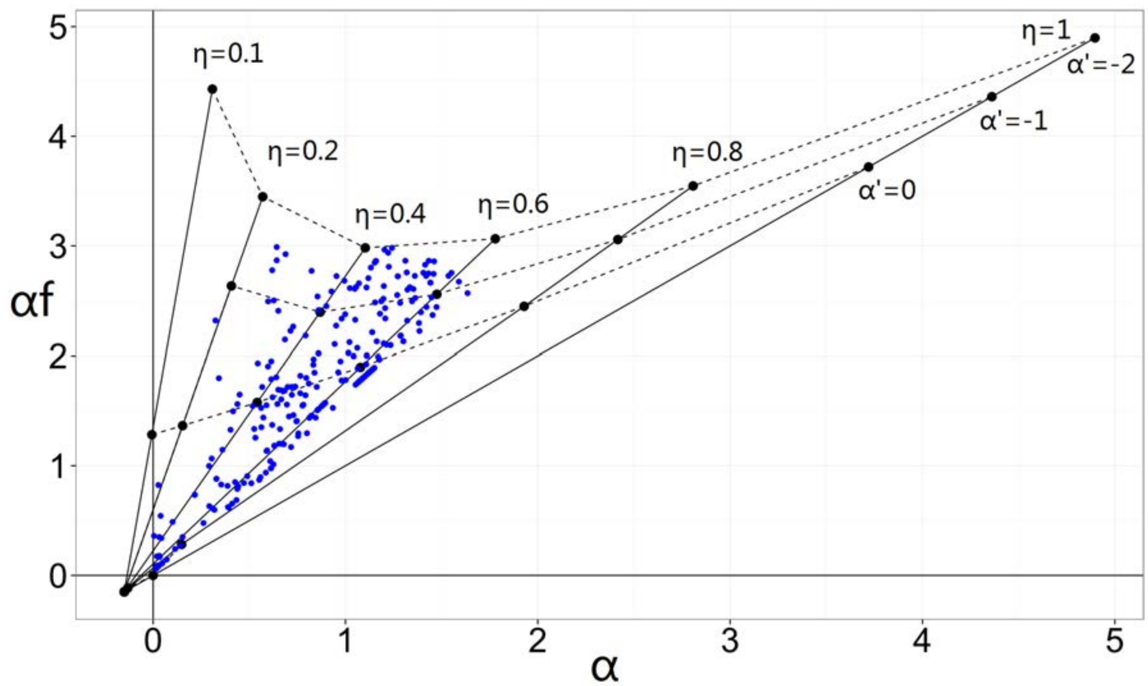

Figure 4.2: Lookup table (LUT) used in the LUT-based spectral deconvolution algorithm (LUT-SDA)

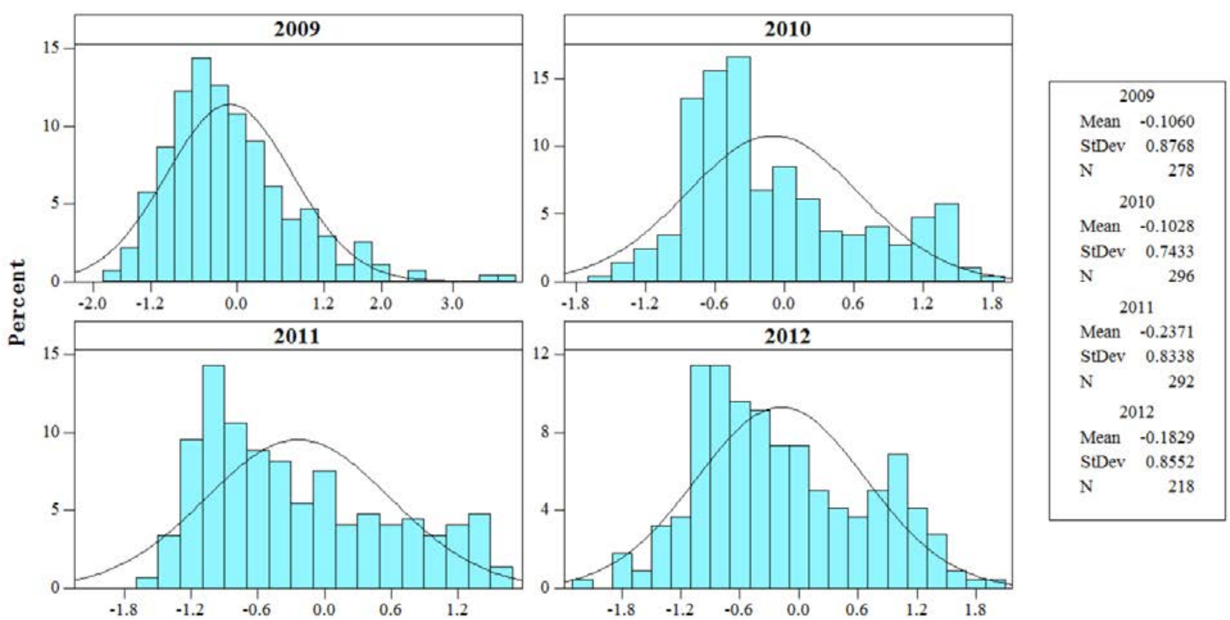

Figure 4.3: Histogram of the AE derivative from 2009 to 2012

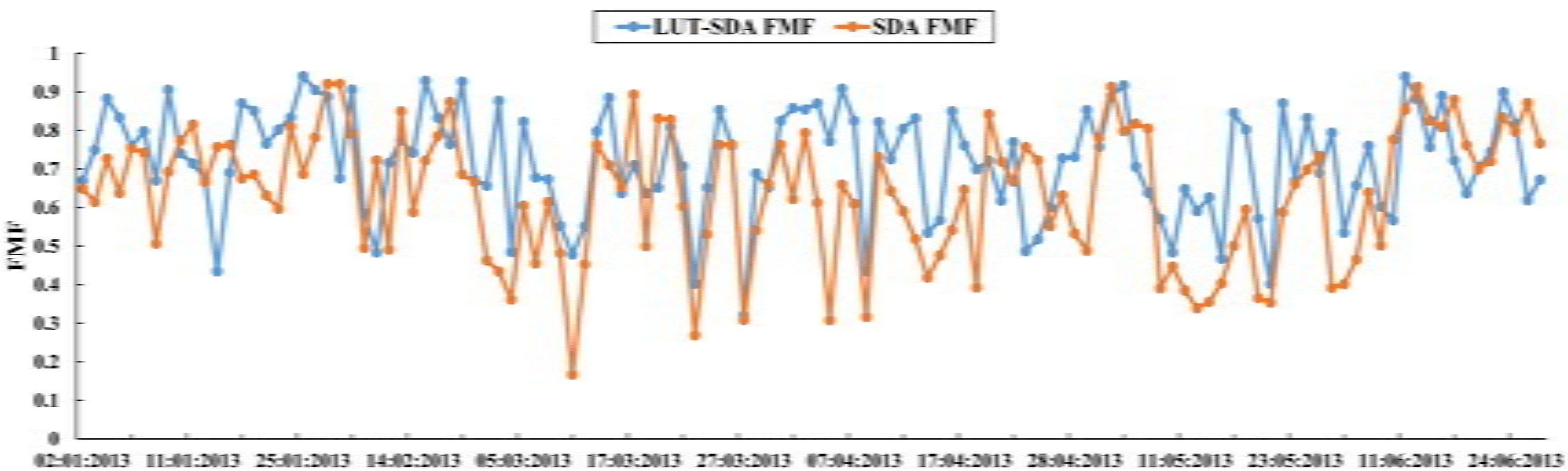

Figure 4.4: Comparison of the LUT-SDA FMF against the AERONET FMF

4.3.2 Satellite FMF validation

The simplified high resolution MODIS aerosol retrieval algorithm (SARA)-retrieved AOT at 500 m resolution was validated with the AERONET AOT (Figure 4.5 A). The linear regression of SARA AOT values against the AERONET observations yielded an R of 0.95 (N = 130). SARA AOT values gave a low RMSE of 0.18, which indicated that the retrieved AOT values were of high quality, which agreed with Bilal, Nichol, and Chan (2014). However, the SARA AOT-retrieved AE had a relatively low correlation coefficient (R = 0.30) with AERONET AE (Figure 4.5 B). Levy et al. (2010) indicated that the MODIS cannot capture the variability of the ground-truth AE due to it not being a multi-viewing angle measurement. The validation of FMF is shown in Figure 4.5 C and shows a fairly good correlation coefficient (R = 0.32) and RMSE (0.16). Although there were some errors in the retrieved FMF, it was much better than the MODIS FMF and was comparable with the AERONET FMF, as shown in Figure 6 of Zhang and Li (2015) and Figure 1 (right) of Jethva et al. (2010). We further studied the dependence of the FMF error using the retrieved AE, which was based on $\Delta\alpha$[1] being less than 0.2 in good comparisons. The results are shown in Figure 4.6 and clearly indicate that the error of the retrieved FMF decreased significantly as the AE was retrieved with a higher accuracy. The correlation coefficient improved from 0.32 to 0.8.

[1] $\Delta\alpha = abs(\alpha_{SARA} - \alpha_{AERONET})$

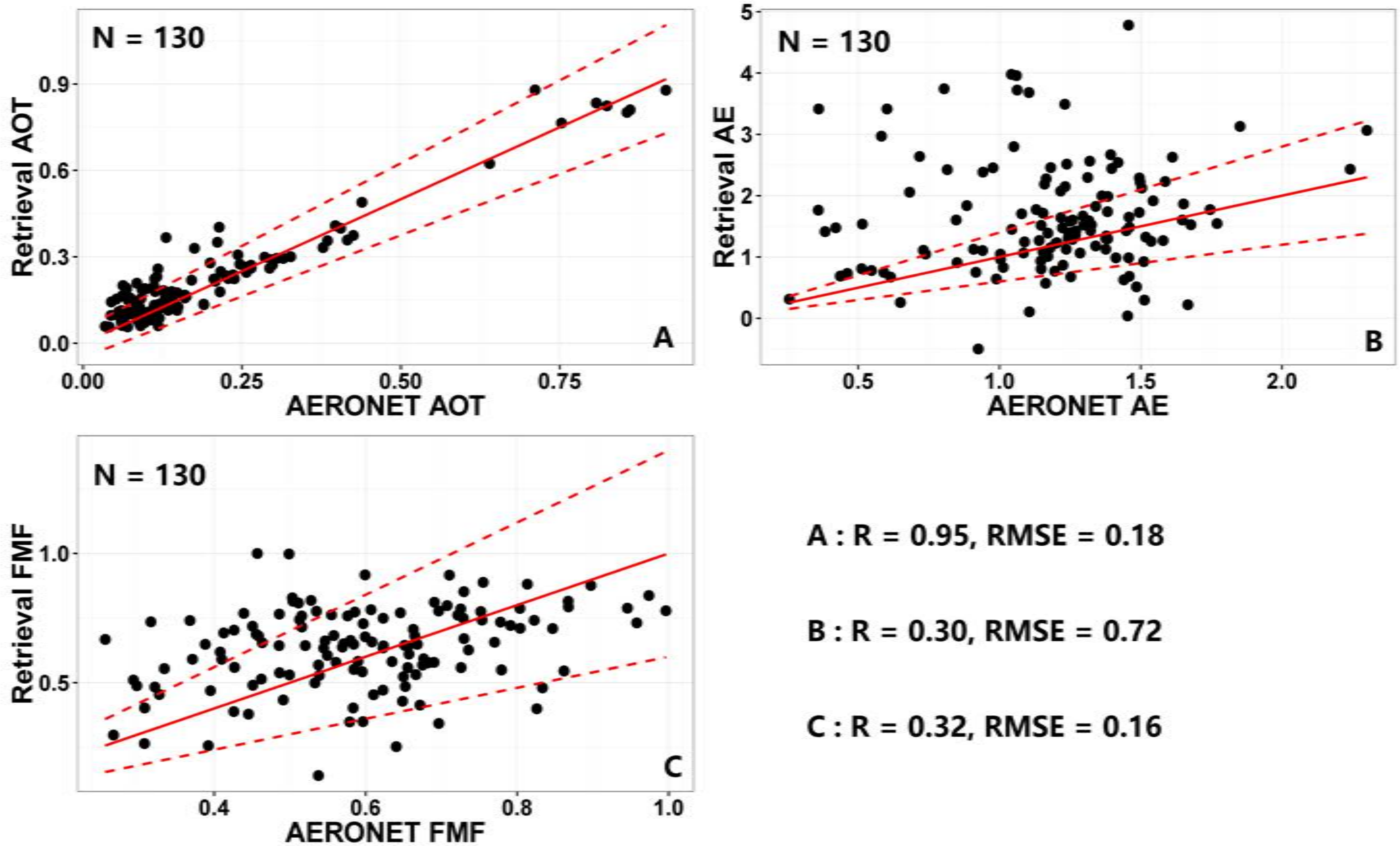

Figure 4.5: Validation using the Aerosol Robotic Network (AERONET) (A: aerosol optical thickness (AOT); B: Angstrom exponent (AE); C: lookup table-based spectral deconvolution algorithm (LUT-SDA) fine mode fraction (FMF), error lines in A are $\Delta\tau = \pm\,(0.05 + 0.15_{AERONET\,AOT})$, error lines in B and C are ± 0.4, the red solid line is 1:1 line)

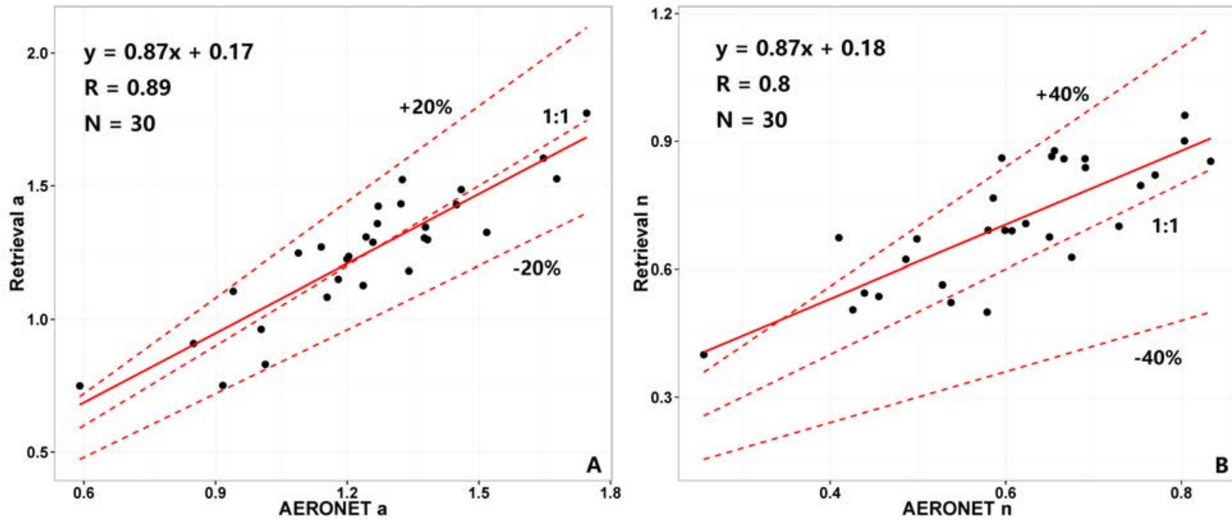

Figure 4.6: Comparison with the Aerosol Robotic Network (AERONET) (A: Angstrom exponent (AE) validation with $\Delta\alpha < 0.2$; B: lookup table-based spectral deconvolution algorithm (LUT-SDA) fine mode fraction (FMF) validation with improved AE)

4.3.3 Comparison with MODIS aerosol products

From Figure 4.7 A and B, it can be seen that the AOT retrieved by SARA agrees well with MOD04 AOT, which indicates there was a high AOT southeast of Beijing on this date (18 May 2014). This area includes the main city region where roads are crowded and the population is dense. In addition, many construction projects, such as a new subway station, are in progress, as described in Yan et al. (2015). The MODIS FMF is shown in Figure 4.7 C, where it can be seen that many pixel values are 0 and a high FMF was present west of Beijing. This result may not be realistic because a pure coarse mode (FMF = 0) AOT in an urban area seems impossible. The LUT-SDA FMF is shown in Figure 4.7 D, where it can be seen that a high FMF was also discovered west of Beijing, but in the city area, there was still a high FMF (0.6-0.7). By comparison, in Figure 4.7C and Figure 4.7D, the LUT-SDA FMF had a better spatial coverage than the MOD04

FMF, and there was no extreme value of 0, which seems more reasonable. From Figure 4.7 B and D, it can be seen that the FMF over land did not have a strong correlation with AOT, which was also found by Zhang and Li (2015).

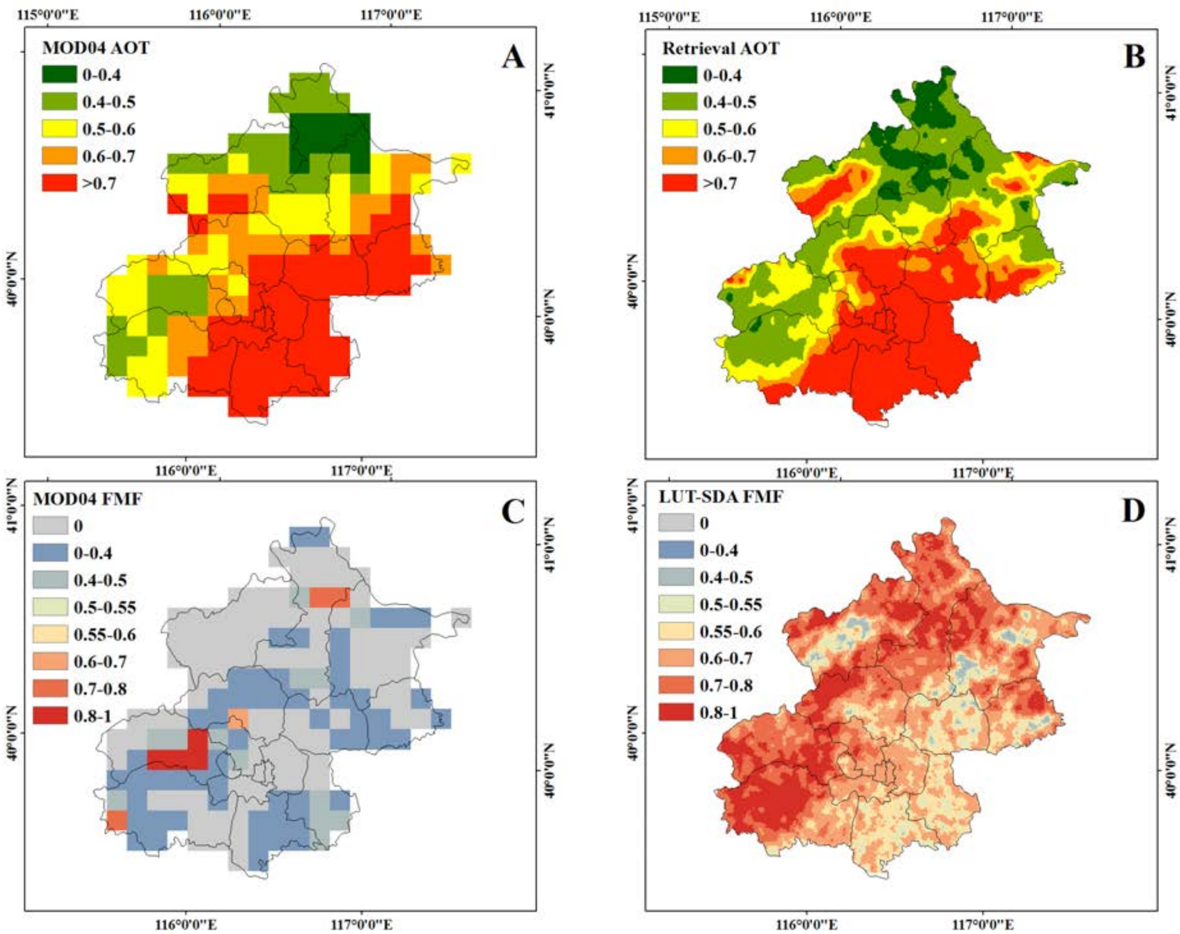

Figure 4.7: Comparison with MODerate resolution Imaging Spectroradiometer (MODIS) MOD04 products (A: MOD04 DT aerosol optical thickness (AOT); B: SARA AOT; C: MOD04 DT fine mode fraction (FMF); D: LUT-SDA FMF)

4.3.4 Seasonal average FMF in Beijing

The FMF retrieved with a high accuracy was selected to analyse its seasonal average spatial distribution in Beijing (Figure 4.8). The FMF was found to be around 0.6-0.65 over most of Beijing in March-April-May (MAM) (Figure 4.8 B). From a comparison of Figure 4.8 B with A and C, it can be seen that, in the spring, the FMF was lower than that in summer and winter. This is because Beijing experiences sand storms originating from the west of China and the Mongolian Gobi desert in spring (Zhang et al., 2014). These sand storms can lead to larger sized aerosols (dust) and result in a lower FMF (Ramachandran, 2007). However, the FMF was high during June-July-August (JJA) in Beijing, and exceeded 0.75 in most places. In JJA, Beijing typically experiences a summer monsoon, which can reduce the influence of sand storms in this region. Under these conditions, anthropogenic aerosol is the main contributor to the total AOT, which results in a high FMF. In December-January-February (DJF), the FMF was observed to be between 0.65-0.7 in most areas, which indicates the dominance of fine mode aerosols in winter. This is due to heating in winter, when coal combustion increases significantly and enhances the emission of anthropogenic aerosols (Zhao et al., 2014). From Figure 4.8, it can also be seen that the FMF was high in the urban centre of Beijing where there is always a high traffic flow and dense population. In these regions, Ramachandran (2007) reported that fine mode aerosols are mainly due to gas to particle conversion and automobile emissions. To validate the seasonal pattern of the FMF derived by the LUT-SDA, the FMF for the corresponding period from AERONET was obtained for comparison. As shown in Figure 4.9, the AERONET FMF displayed the same seasonal pattern as the LUT-SDA FMF.

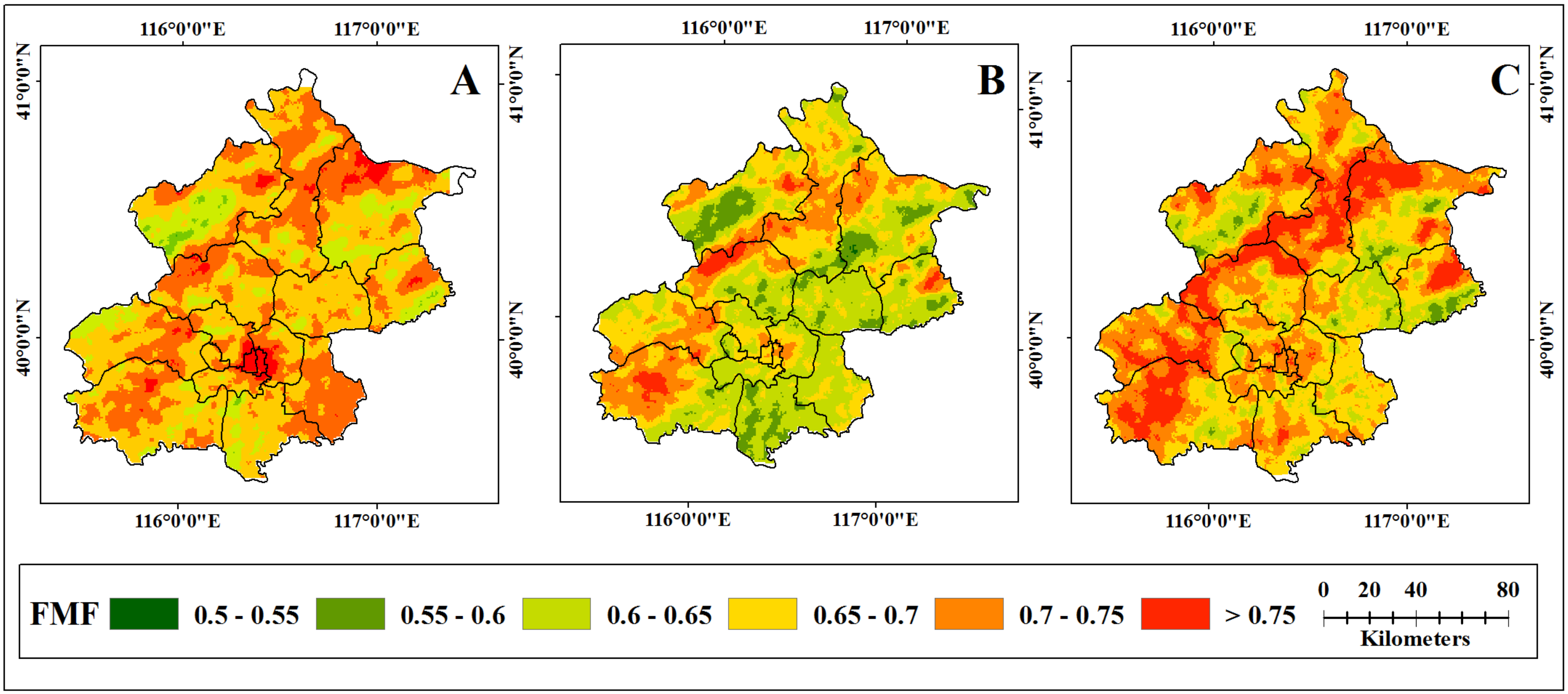

Figure 4.8: Seasonal average spatial distribution of the fine mode fraction (FMF) in Beijing (A: December-February (DJF), B: March-May (MAM) C: June-August (JJA))

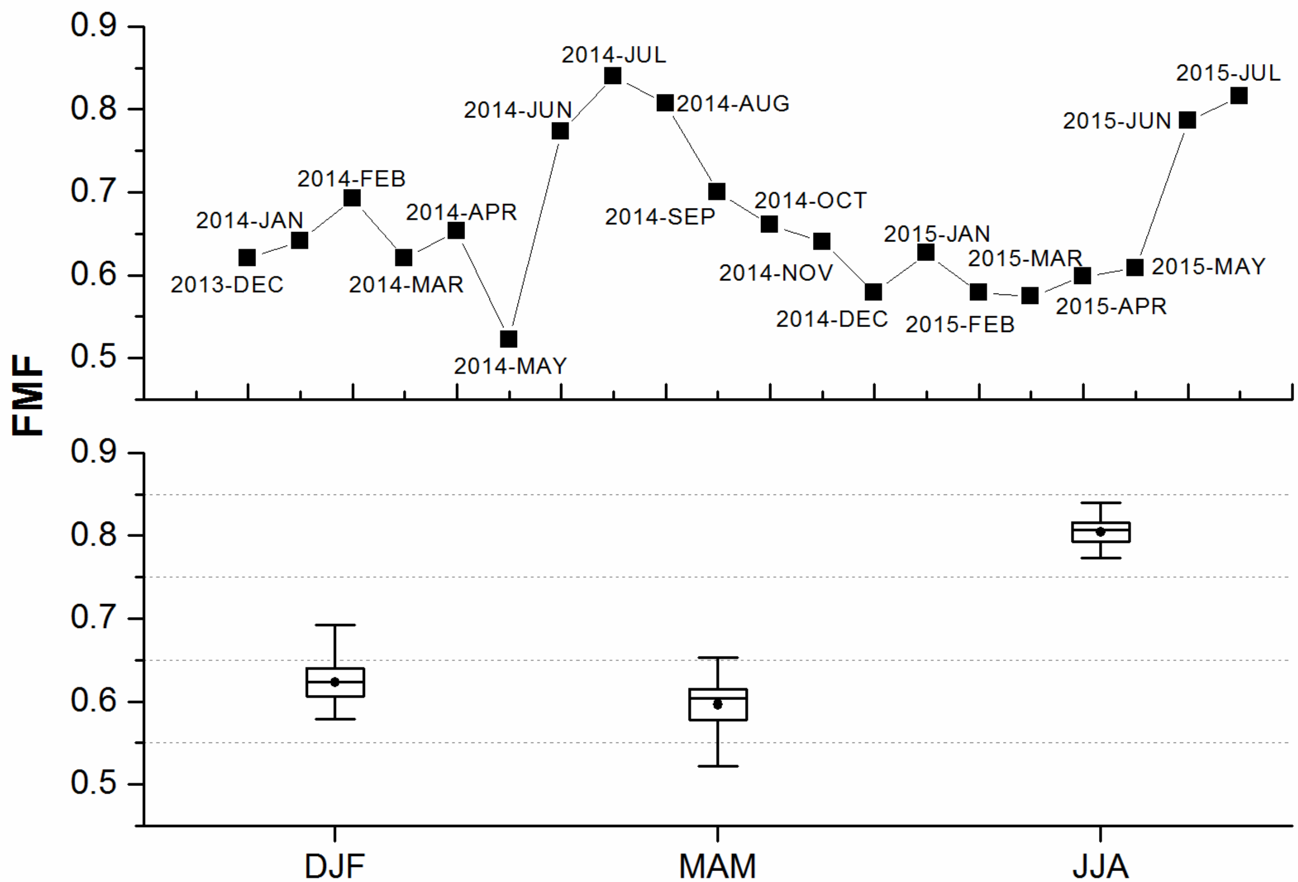

Figure 4.9: Aerosol Robotic Network (AERONET) fine mode fraction (FMF) from December 2013 to July 2015 (top: mean FMF in each month; bottom: boxplots of FMF in December-February (DJF), B: March-May (MAM) and C: June-August (JJA))

4.3.5 Expansion of the LUT-SDA to a large area

To test the ability of the LUT-SDA, we applied it to a large area. The results are shown in Figure 4.10. The test MODIS image was obtained on 16 October 2014; it was found that the FMF had a significant spatial pattern on this day. A large FMF was discovered in the North China Plain, including Beijing, Tianjin and Baoding. The North China Plain is one of the most populated and industrialized areas in China, and its rapid development of urbanized construction has led to severe PM2.5 pollution (Quan et al., 2011; Tao et al., 2012). Xin et al. (2014) reported a PM2.5 concentration distribution, which is similar to the retrieved FMF in this region. Datong, Shuozhou and Xinzhou are the other areas with a large FMF and are located in the Shanxi Provinces. The FMF values were mostly above 0.6 in these regions. Ma et al. (2014) reported that the Shanxi Provinces also experienced high levels of PM2.5 pollution. From Figure 10 it can be seen that the LUT-SDA can be successfully applied on a large-scale study, but further studies of its correlation with PM2.5 are required.

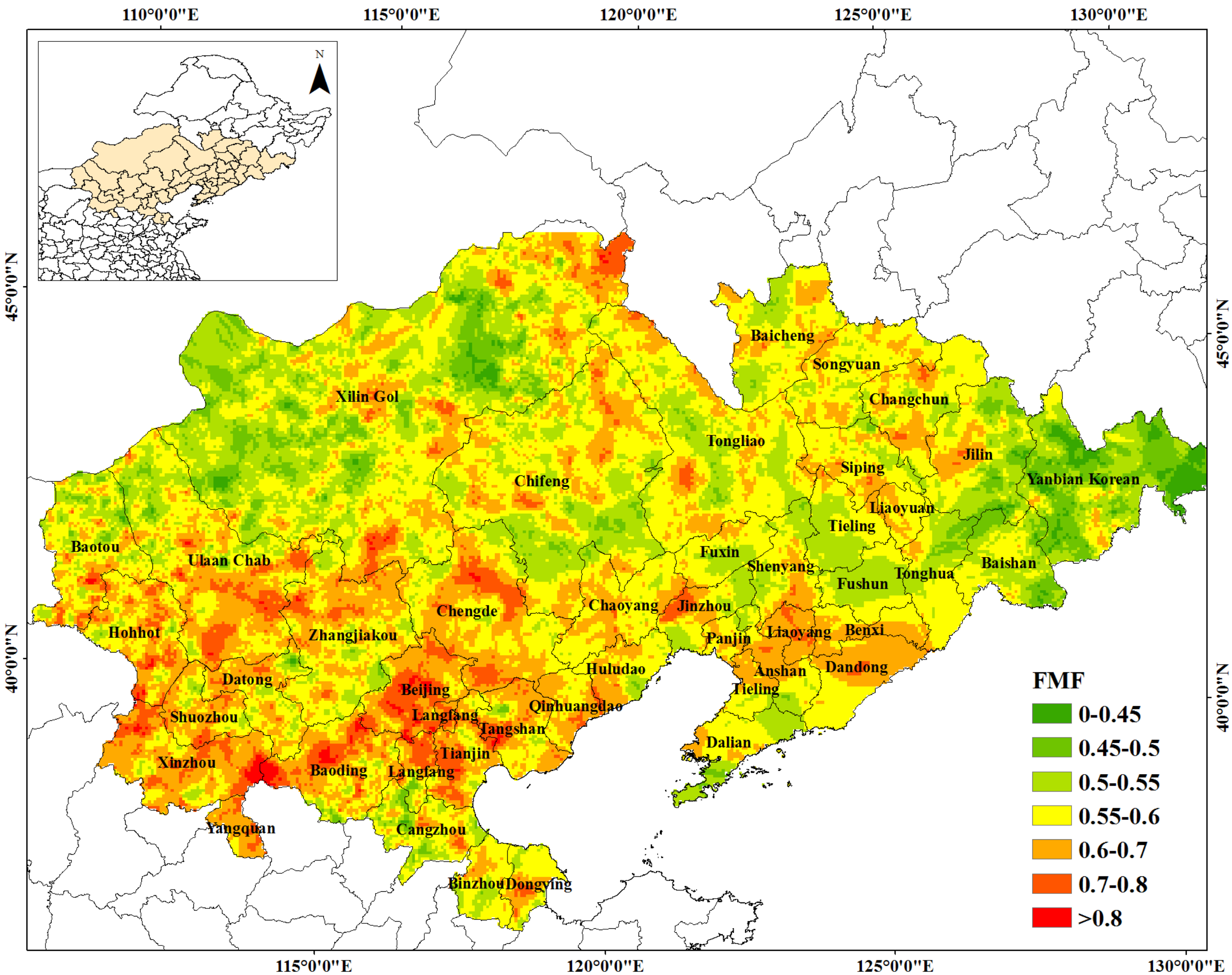

Figure 4.10: Fine mode fraction (FMF) retrieval northeast of China on 16 October 2014

4.3.6 Discussion

A high accuracy of FMF retrieval is very difficult to obtain for satellite images because AE, as the key parameter for FMF retrieval, has many uncertainties in satellite measurements. As shown in Figure 4.6, when the accuracy of AE is enhanced, the accuracy of the retrieved FMF is clearly improved. Although the derived AOT can have a high precision, the derived AE is generally imperfect. Hasekamp and Landgraf (2007) indicated that uncertainties in the surface reflectance that is used were one of the largest error sources in aerosol properties retrieved from MODIS. They also found that single-viewing angle measurements of intensity alone did not provide sufficient information regarding aerosol properties. Sayer et al. (2013) reported that the latest C6 MOD04 Deep Blue AOT has a strong correlation with the AERONET AOT (R = 0.93); however, the AE validation had a weaker correlation (R = 0.45). Levy et al. (2010) revealed that MODIS does not provide quantitative information about aerosol size over land, and recommend that users should not use size products quantitatively. In the latest MOD04 Collection 6 aerosol product, the AE over land (based on the dark target algorithm) has been deleted, and therefore users need to derive it themselves, making it difficult to obtain the AE (Levy et al., 2013). Therefore, to obtain an accurate FMF, a reliable method for AE retrieval needs to be developed. Due to MODIS not being a multi-viewing angle measurement, the use of ground-based data (e.g., AERONET) is a solution for improving the retrieval accuracy. Jethva et al. (2010) found that using the new absorbing aerosol model (SSA = 0.85), which is based on AERONET, for the Indian region could improve the retrieval accuracy of FMF.

4.4 Summary

In this chapter, MODIS measurements were used to develop a lookup table-based spectral deconvolution algorithm (LUT-SDA). This method was compared with ground-based data and had a high accuracy compared to the AERONET FMF. The LUT-SDA was then applied to MODIS data for the period of December 2013 to July 2015. The results showed that the Angstrom exponent (AE) had a significant impact on the derived FMF. When the accuracy of the AE was improved (R increased from 0.30 to 0.89), the errors in FMF outcomes were significantly reduced (R increased from 0.32 to 0.68). In comparison with the C6 MOD04 FMF, the LUT-SDA FMF had a better spatial coverage and there was no extreme value 0, which seems more reasonable. Based on the LUT-SDA, the seasonal average spatial distribution of FMF in Beijing was obtained. The FMF in Beijing was observed to have a seasonal pattern, which was in good agreement with the phenomenon obtained by AERONET. In addition, this study used the LUT-SDA to study large areas, with the outcomes showing that it could be feasibly used for further PM2.5 estimations.

Chapter 5

Monitoring surface PM2.5 based on fine mode aerosol optical thickness

5.1 Introduction

In recent years, air pollution, especially PM2.5 pollution has become a serious environmental problem all over the world. PM2.5 easily absorbs heavy metals and organic matters, thus negatively affects human health such as increasing mortality rates and aggravating respiratory symptoms. However, it is difficult to estimate the surface-level PM2.5 using satellite-based AOT because the relevant correlation is influenced by many factors, such as retrieval AOT algorithms and meteorological influence. As shown in Chapter 4, it proposed a LUT-SDA method for satellite FMF and the outcome which showed a high correlation with AERONET FMF. In addition, a Simplified Aerosol Retrieval Algorithm (SARA) was developed to derive AOT from MODIS by Bilal et al. (2013) , which could provide 500 m spatial resolution AOT and has been validated in Hong Kong and Beijing (Bilal, Nichol, and Chan, 2014). Therefore, the objective of this chapter is to develop a ground-level PM2.5 retrieval model based on FM-AOT, which is incorporated with LUT-SDA, SARA and the physical method of PM2.5 remote sensing method.

5.2 Data and methods

5.2.1 AERONET

In this study, AOT and FMF were collected by AERONET site Beijing (level 2), CAMS and RADI (level 1.5) from December 2013 to June 2015.

5.2.2 SARA-retrieved AOT

The MODIS MOD02HKM, MOD03 and MOD09 cloud free data were acquired (https://ladsweb.nascom.nasa.gov) for AOT retrieval as shown in Table 5.1. The SARA was applied in this study due to its effective and high accuracy. AOT derived by SARA was validated in Beijing and the results showed a very good correlation with AERONET AOT (0.97-0.99) and low Root Mean Square Error (RMSE) 0.067-0.133 (Bilal, Nichol, and Chan, 2014).

Table 5.1: The MODIS data used in Chpater 5

Date	Month	Year	Date	Month	Year
11	12	2013	16	10	2014
12	12	2013	17	10	2014
14	12	2013	13	11	2014
26	12	2013	17	11	2014
28	12	2013	22	11	2014
30	12	2013	1	12	2014
1	1	2014	3	12	2014
3	1	2014	17	12	2014
13	1	2014	24	12	2014
22	1	2014	31	12	2014
3	2	2014	2	1	2015
4	2	2014	6	1	2015
27	2	2014	11	1	2015
2	3	2014	27	1	2015
14	3	2014	30	1	2015
22	3	2014	5	2	2015
7	4	2014	17	2	2015
2	5	2014	26	2	2015
7	5	2014	3	3	2015
16	5	2014	11	3	2015
18	5	2014	21	3	2015
3	6	2014	23	3	2015
12	6	2014	21	4	2015
27	6	2014	22	4	2015
28	6	2014	24	4	2015
10	7	2014	26	4	2015
12	7	2014	4	5	2015
15	8	2014	7	5	2015
25	8	2014	19	5	2015
3	9	2014	26	5	2015
8	9	2014	2	6	2015
9	9	2014	8	6	2015
15	9	2014	18	6	2015

5.2.3 Ground-measured PM2.5

The hourly ground-measured PM2.5 data over Beijing region from December 2013 to June 2015 were acquired from the Beijing Municipal Environmental Monitoring Center (http://zx.bjmemc.com.cn). PM2.5 monitoring sites are plotted in Figure 5.1, which shows that the majority of monitoring sites are located in urban areas and a few are in rural areas. The PM2.5 measurement is based on the Chinese National Ambient Air Quality Standard (GB3095-2012) by the tapered element oscillating microbalance method (TEOM) or the beta-attenuation method (Li et al., 2015).

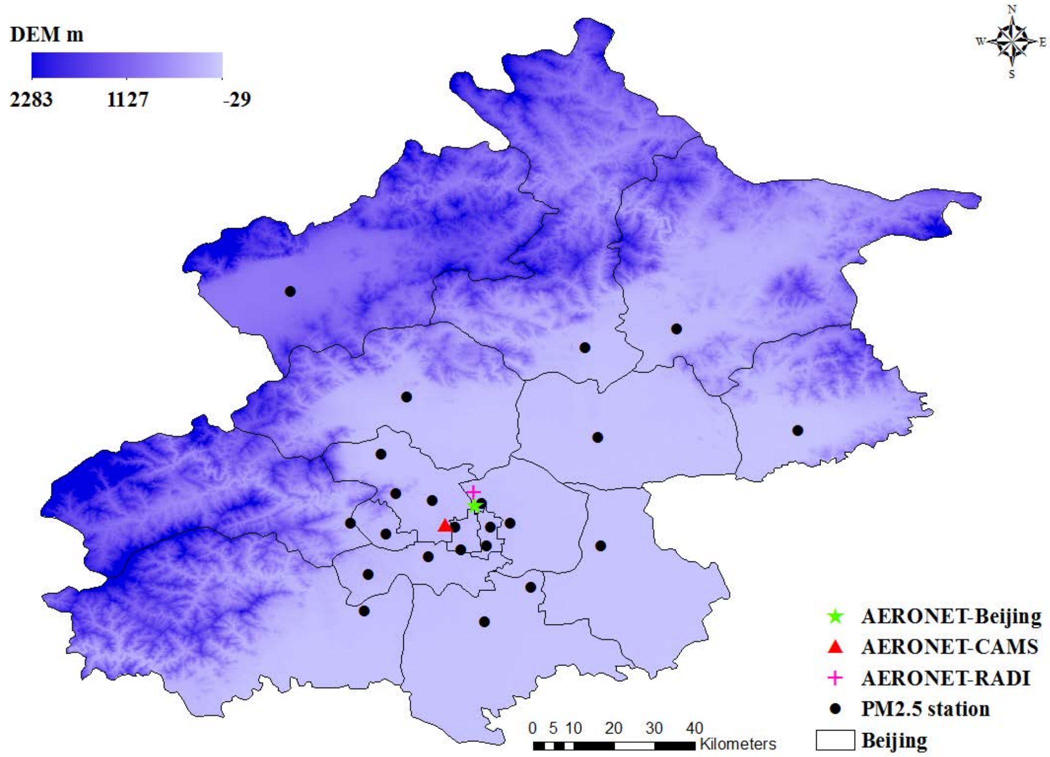

Figure 5.1: Study area

5.2.4 LUT-SDA FMF

As shown in Chapter 4, the LUT-SDA is developed for satellite images based on only two wavelengths of AOT to solve the FMF problem. This method is based on SDA which is currently used in the AERONET. Thus, the outcome of LUT-SDA can match AERONET's well and can be properly used as an input parameter for the AERONET FMF-based model. The successful use of the LUT-SDA applied to MODIS data not only verified the application of this method to the urban scale (Beijing), but also verified its application to a large area (northeast China). The retrieved FMF images are able to represent the spatial distribution of the fine aerosol contribution to the total AOT with complex surface types. Therefore, in this study we used LUT-SDA to retrieval FMF and further correlated with PM2.5 estimation.

5.2.5 PBLH and RH

Weather Research and Forecasting (WRF) model 3.6.1 was applied to produce the needed PBLH and RH. WRF model is a next-generation mesoscale numerical weather prediction system that was validated as a good performance for simulation of meteorological data (Ying et al., 2009; Grgurić et al., 2014). Initial and boundary conditions stemmed from the National Centers for Environmental Prediction (NCEP) Final (FNL) Operational Global Analysis data (http://rda.ucar.edu/datasets/ds083.2/). NCEP FNL is provided globally 1 degree resolution every 6 hours. The physics options selected for the WRF simulation for this research are same as Zheng et al. (2016).

5.2.6 Ground-level PM2.5 retrieval model

Zhang and Li (2015) developed a PM2.5 remote sensing method for the ground-level PM2.5 estimation and validated it at Jinhua city of China (Li et al., 2016). This method proposed a relationship between AOT and PM2.5 concentration based on AERONET data, which including FM-AOT conversion, fine particle volume calculation, PBLH and RH correction. The surface PM2.5 concentration can be obtained by:

$$PM_{2.5} = AOT \cdot \frac{FMF \cdot VE_f \cdot \rho_{f \cdot dry}}{PBLH \cdot f(RH)} \tag{5.1}$$

Where FMF is fine mode fraction, VE_f is columnar volume-to-extinction ratio of fine particulates, $\rho_{f \cdot dry}$ is density of dry PM2.5, PBLH is the planetary boundary layer height and $f(RH)$ is optical hydroscopic growth function. And VE_f can be calculated by:

$$VE_f = 0.2887FMF^2 - 0.4663FMF + 0.356 \quad (0.1 \leq FMF \leq 1.0) \tag{5.2}$$

In this study, $f(RH)$ is based on Chen et al. (2015):

$$f(RH) = \begin{cases} 1.02 \times (1 - RH/100)^{-0.21 \times RH/100} & (RH/100 < 0.6) \\ 1.08 \times (1 - RH/100)^{-0.26 \times RH/100} & (RH/100 \geq 0.6) \end{cases} \tag{5.3}$$

$\rho_{f \cdot dry}$ is assumed as a constant value 1.5 g/cm^3 in Zhang and Li (2015) and Li et al. (2016). However, in this study we deemed that $\rho_{f \cdot dry}$ may differ for each day and the detail of this issue will be described in Section 5.3.3. Thus, this study proposed a pseudo density of PM2.5 (ρ_{pseudo}) which can be calculated by:

$$\rho_{pseudo} = AOT \cdot \frac{FMF \cdot VE_f \cdot PM_{2.5}^{V}}{PBLH \cdot f(RH)} \tag{5.4}$$

Where AOT and FMF are obtained by AERONET corresponding to satellite overpass, PBLH and f (RH) are produced by WRF.

In Equation 5.4, PM2.5 is calculated by visibility. Previous studies had been indicated that PM2.5 can be calculated by visibility from the power function (Leung, Wu, and Yeung, 2009):

$$PM_{2.5}^{V} = A \cdot x^{B} \tag{5.5}$$

Where x is visibility (km) which is obtained from weather station for Beijing (https://www.wunderground.com/). A and B are parameters for this equation which are discussed in Section 5.3.3.

Therefore, the schematic diagram of ground-level PM2.5 retrieval method for this research is shown in Figure 5.2. There are mainly two steps: (i) calculate ρ_{pseudo} assistant by visibility data using Equation 5.5; (ii) incorporate ρ_{pseudo} to Equation 5.1 with SARA-AOT (500 m), LUT-SDA FMF, PBLH and RH correction for surface PM2.5 retrieval.

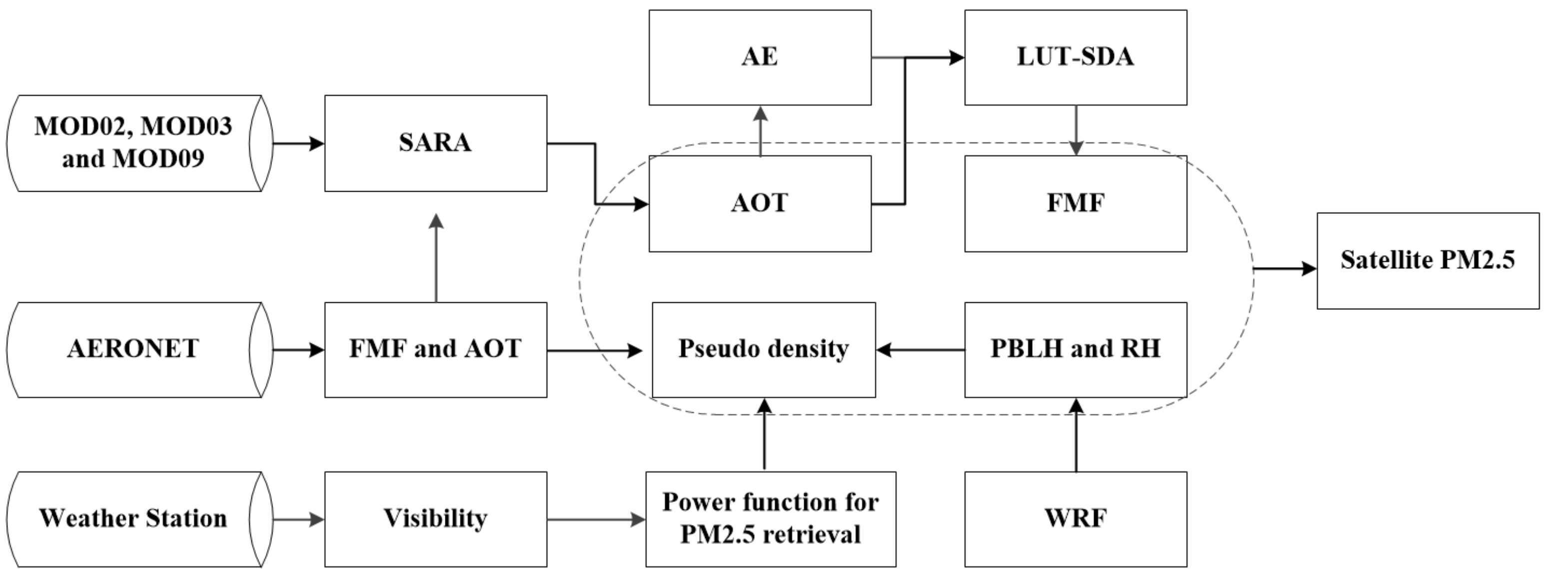

Figure 5.2: Schematic diagram for the ground-level PM2.5 retrieval model

5.3 Result and discussion

5.3.1 Comparison FM-AOT and AOT for PM2.5 estimation

Comparison between retrieval PM2.5 by total AOT and FM-AOT is shown in Figure 5.3. This comparison was divided into two groups based on normal and haze weather conditions. There were 778 samples collected for statistical regression analysis in the normal days. The correlation between total AOT and PM2.5 with $R^2 = 0.43$ and $r = 0.66$ is shown in Figure 5.3A. However, the correlation is reduced using the FM-AOT instead of total AOT as presented in 5.3B ($R^2 = 0.35$ and $r = 0.6$). Boyouk et al. (2010) also found that R^2 was decreased significantly from 0.73 to 0.65 when the total AOT was replaced by FM-AOT. Nevertheless, as shown in Figure 5.3C and Figure 5.3D, when the PBLH and RH correction was incorporated, the correlation between FM-AOT and PM2.5 had an obvious improvement (R^2 from 0.35 to 0.46 and r from 0.6 to 0.68), and some improvements could also be observed in total AOT's (R^2 from 0.43 to 0.45 and r from 0.66 to 0.67).

As for in haze condition, Figure 5.3E and Figure 5.3F showed that FM-AOT had a slight better relationship with PM2.5 ($R^2 = 0.33$ and $r = 0.58$) than total AOT's ($R^2 = 0.31$ and $r = 0.55$). The similar phenomenon is also found by Zhang and Li (2013), but the improvement by FM-AOT in this research is not as significant as theirs. This is because the test data in Zhang and Li (2013) were in winter (January) while in this study was nearly 2 years. Di Nicolantonio et al. (2007) indicated that different months could have distinct impact on the correlation of total AOT and FM-AOT with PM2.5 concentration. From Figure 5.3G and Figure 5.3H, we cannot observe any improvement when the PBLH and RH correction are accounted. This is because the relationship between aerosol extinction coefficient and height does not follow exponential attenuation model under haze condition (Lv et al., 2013), which makes the PBLH correction unsatisfactory. In addition, when PM2.5 < 200 μg/m^3 and RH < 80%, RH correction can achieve a good outcome (Zhang and Li, 2013). However, in haze days the PM2.5 is frequent more than 200 μg/m^3, which makes the RH correction inapplicable since the relationship between aerosol scattering coefficient and RH does not obey the hygroscopic growth.

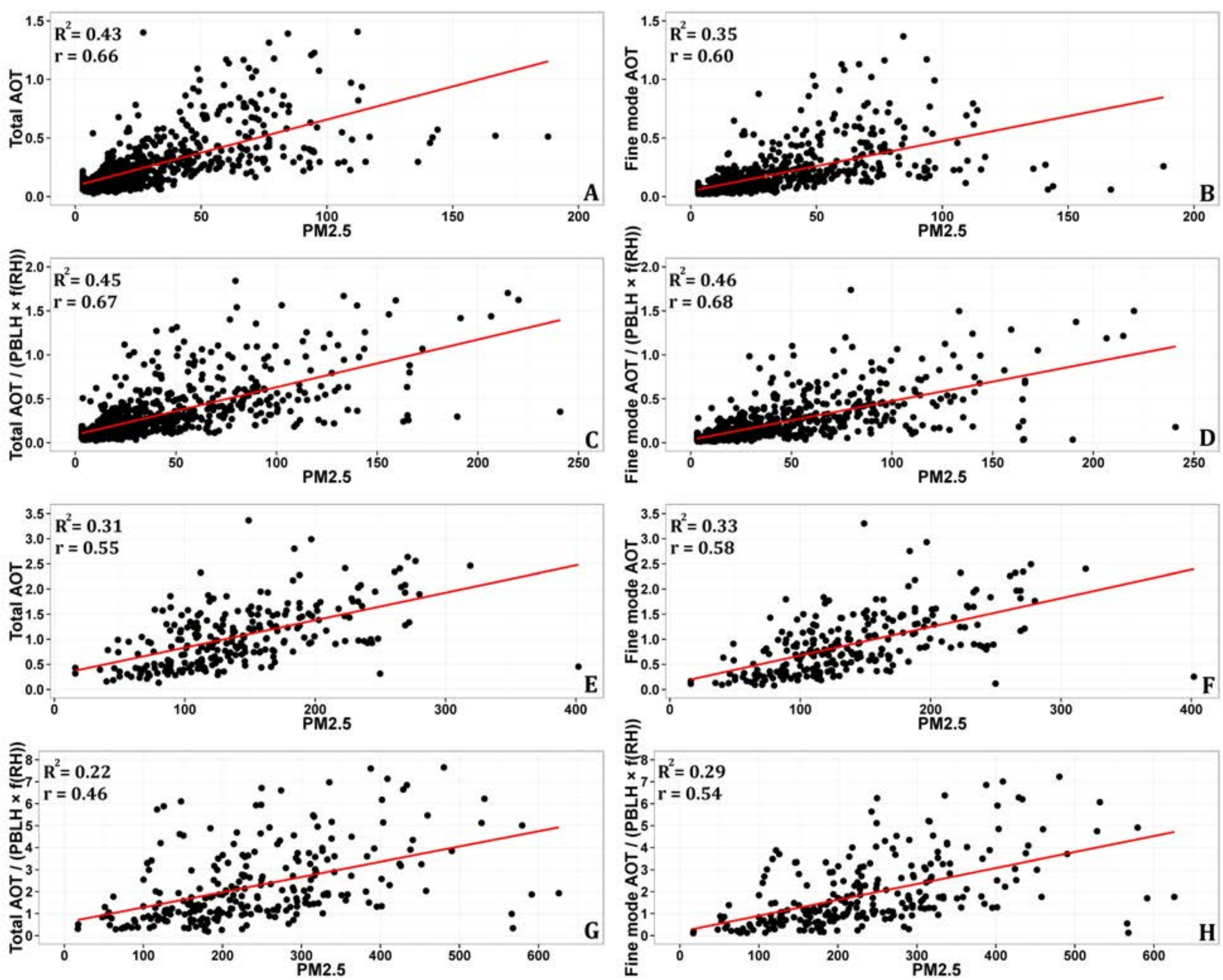

Figure 5.3: Comparison between total AOT and FM-AOT for PM2.5 (A, B, C and D are in the normal weather days, N=778; E, F, G and H are in haze days, N = 248)

5.3.2 LUT-SDA FMF

As shown in Equation 5.1 and Equation 5.2, FMF is a very important parameter which can directly affect not only VE_f but also final PM2.5 outcomes. Thus, a reliable FMF is necessary for the PM2.5 retrieval. In this study, FMF was calculated by LUT-SDA and comparison between AERONRT and MODIS FMF was presented in Figure 5.4. From the series FMF plots, it is obvious that LUT-SDA FMF has a good agreement with AERONET FMF. However, MODIS FMF missed most of data in this study period. Levy et al. (2010) indicated that MODIS-retrieved FMF over land is still an experimental product and has little physical validity. Li et al. (2016) also mentioned that the accuracy of MODIS retrieval FMF limits the Equation 5.1 application and validation. From Figure 5.4, it shows that LUT-SDA FMF is a good choice instead of MODIS FMF, which can achieve widely covered FMF. Although LUT-SDA FMF is not accurate as field measurement, it can provide a better spatial view of FMF while the field measurement only has point-scale values.

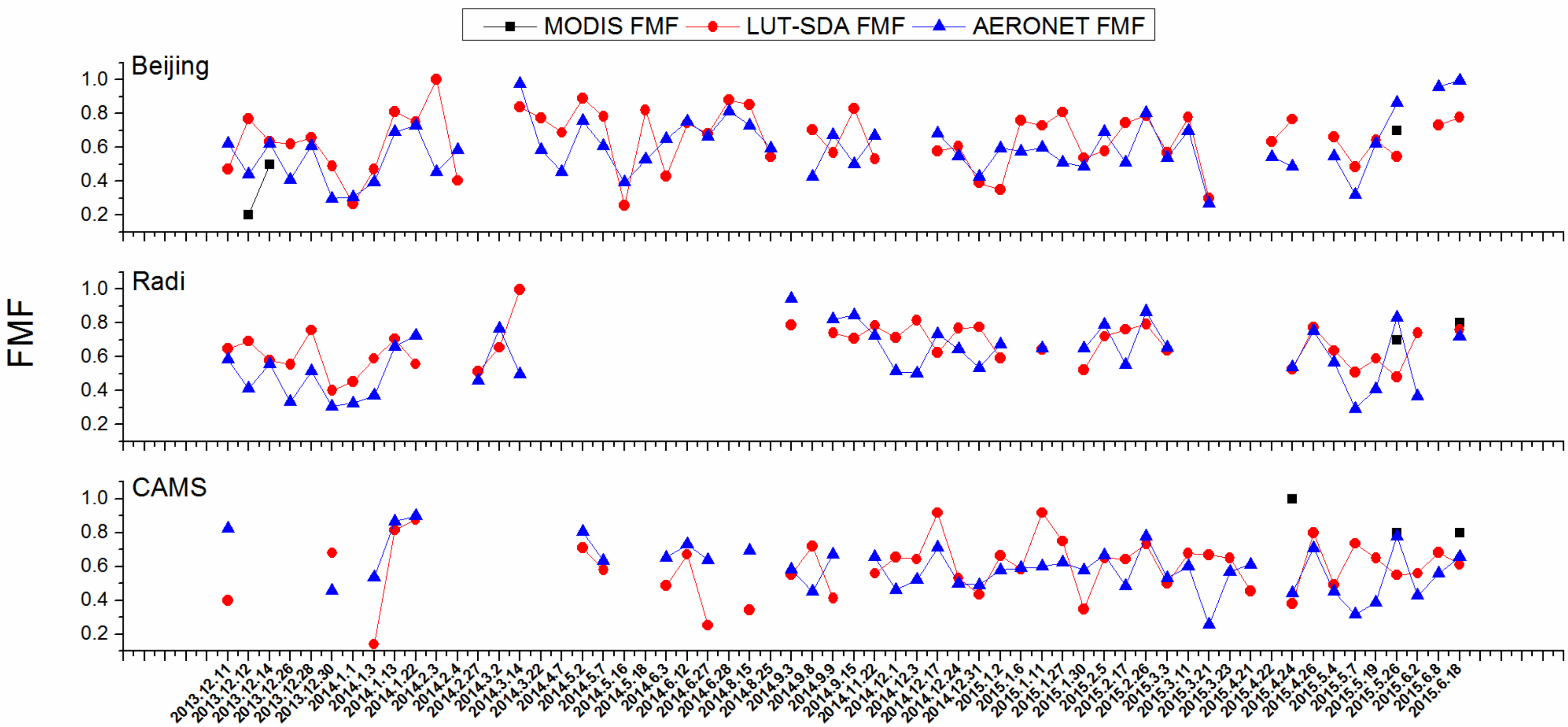

Figure 5.4: Comparison FMF between MODIS, LUT-SDA and AERONET

5.3.3 Pseudo density for PM2.5

Many studies had been presented that particle density of PM2.5 has strong seasonal and diurnal variations (Zhao et al., 2013; Wang et al., 2014; Liu et al., 2015). As shown in Table 5.2, density of PM2.5 in the warm season is always higher than the cold seasons. On average, the density of PM2.5 can increase from 1.68 g/cm^3 in the cold season to 1.81 g/cm^3 in the warm season due to the organic matter contribution during the cold season in Beijing (Liu et al., 2015). Thus, it is difficult to use a constant empirical PM2.5 density value in Beijing. Because of this issue, a rough estimate of ambient particle density for PM2.5 is necessary for improving accuracy of surface PM2.5 retrieval. Therefore, in this study, a pseudo density was proposed to solve this challenge. Based on Chen et al. (2015), PM2.5 can be directly calculated by the visibility through the power functions under different relative humidity conditions, as shown in Table 5.3. Then, by Equation 5.4 and Equation 5.5, the daily pseudo density of PM2.5 was calculated in this study period. As shown in Figure 5.5, the pseudo density of PM2.5 has significant changes in each day due to different weather and pollution conditions. The daily PM2.5 pseudo density is up to 2.5 g/cm^3 or low to 0.23 g/cm^3 for the specific days. The statistics for PM2.5 pseudo density is showed in Figure 5.6, the mean value is 1.02 g/cm^3 with confidence interval from 0.97 to 1.06 g/cm^3 and the standard deviation is up to 0.62. By Figure 5.5 and Figure 5.6, assuming a variable PM2.5 density in the retrieval model for each day seems more suitable than the constant density assumption.

Table 5.2: Density of PM2.5 in Beijing from literature

Reference	Density(g/cm^3)	Sampling time
Liu et al. (2015)	1.60 ± 0.43	July to September 2014
Zhao et al. (2013)	1.66 ± 0.74	January to February 2010
	1.82 ± 0.33	July to August 2009
Gao et al. (2007)	1.5	April to August 2005
Cao et al. (2012)	1.79 ± 0.23	June to July 2003
	1.65 ± 0.37	January 2003
Wang et al. (2014)	1.72 ± 0.94	December 2002 to February 2003
	1.82 ± 0.47	July to August 2002

Table 5.3: Power function for PM2.5 in Beijing

Relative humidity	Power function for PM2.5 (mg/m^3)
RH<70%	$PM_{2.5} = 0.6977x^{-0.9517}$
70%⩽RH⩽80%	$PM_{2.5} = 0.3628x^{-1.028}$
80%<RH⩽90%	$PM_{2.5} = 0.2957x^{-0.9463}$

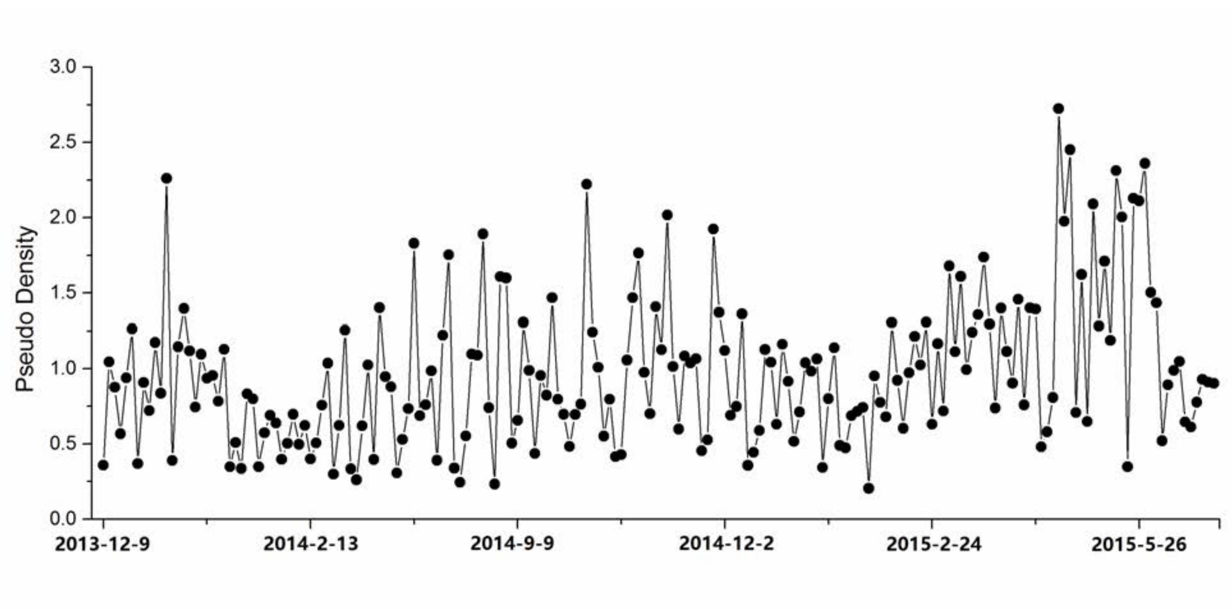

Figure 5.5: Variation of PM2.5 pseudo density (unit: g/cm^3) from December 2015 to June 2015

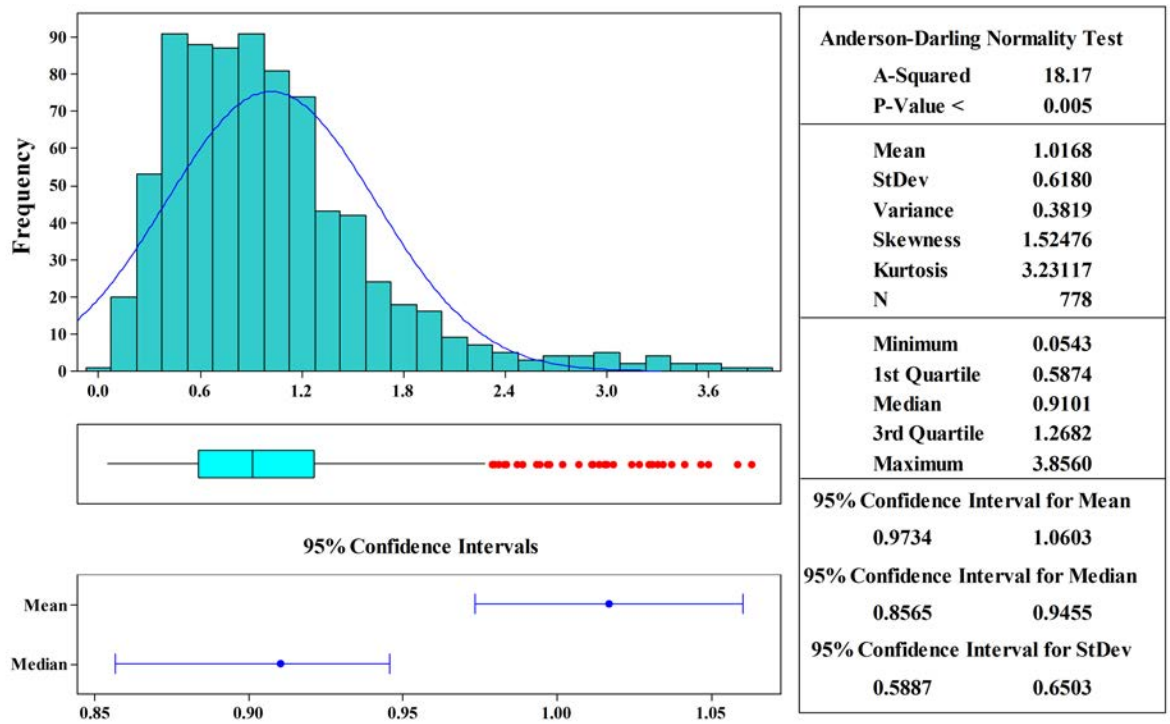

Figure 5.6: Statistics of PM2.5 pseudo density in this study period

5.3.4 PM2.5 retrieval results and validation

To evaluate the performance of the PM2.5 retrieval model proposed in this study, we took two retrieval results as example. Figure 5.7 shows the PM2.5 estimation on 6 January 2015. We can see that AOT by SARA ranges from 0.05 to 0.27 and its the highest value is always centered in the south of Beijing (Figure 5.7A), while the FMF derived by LUT-SDA presents the highest value in the center and south east of urban area that always has high traffic and dense population (Figure 5.7B). These areas with high FMF indicate that contribution of fine particles to total AOT is large. The PBLH and RH produced by WRF are showed in Figure 5.7C and Figure 5.7E. The PBLH presents an obviously different spatial coverage on this day. In the north of Beijing, PBLH reaches up to 605-746 m and more than 474 m in the most of center areas. However, in the east and west of Beijing, the PBLH is always around 366-417 m. Figure 5.7E shows that the RH decreases gradually from northwest (0.29-0.33) to southeast (0.18-0.21) of Beijing. Corresponding to RH, the $f(RH)$ is showed in Figure 5.7D and we can see that its spatial pattern is similar to Figure 5.7E. Finally, the derived PM2.5 is presented in Figure 5.7F, and the results show that PM2.5 spatial pattern is slightly different with the AOT shown in Figure 5.7A. High-level PM2.5 in the southern and eastern urban is clearly seen, which indicates anthropogenic pollution is heavy in these areas. However, the PM2.5 mass concentration is low in the northern rural regions which is around 6-23 μg/m^3.

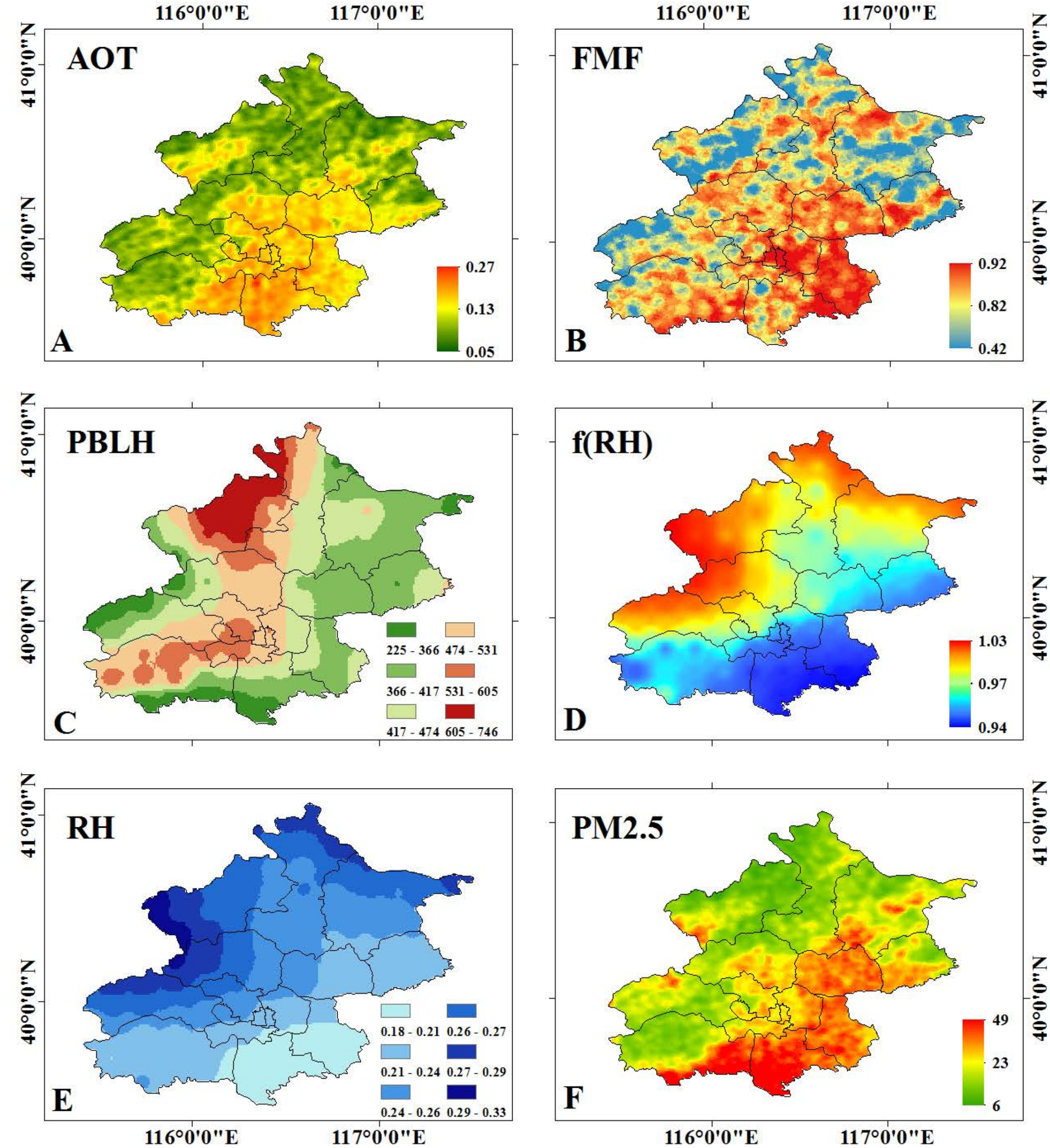

Figure 5.7: PM2.5 estimation on 6 January 2015 (unit: PBLH is m, PM2.5 is μg/m^3)

In order to further test the PM2.5 retrieval model, we extend the study area to Beijing nearby cities. The test data was obtained on 16 October 2014 and the derived results are showed in Figure 5.8. The highest AOT is located in the south of Beijing, east of Tianjin, southwest and east of Hebei (Figure 5.8A). From Figure 5.8B, it is observed that FMF value is high in the center of Beijing, south of Hebei and east of Tianjin. The PM2.5 retrieval result is showed in Figure 5.8C, we can see that high PM2.5 polluted regions are the south part of Beijing and Hebei, and also in the east part of Tianjin. This result is consistent with the findings by Zhang and Li (2015), Ma et al. (2014) and Zheng et al. (2016). Comparing Figure 5.8A and Figure 5.8C, the derived PM2.5 has similar spatial pattern with AOT, but with some differences due to FMF, RH and PBLH correction, such as the west of Hebei where the AOT is high, but the PM2.5 is medium.

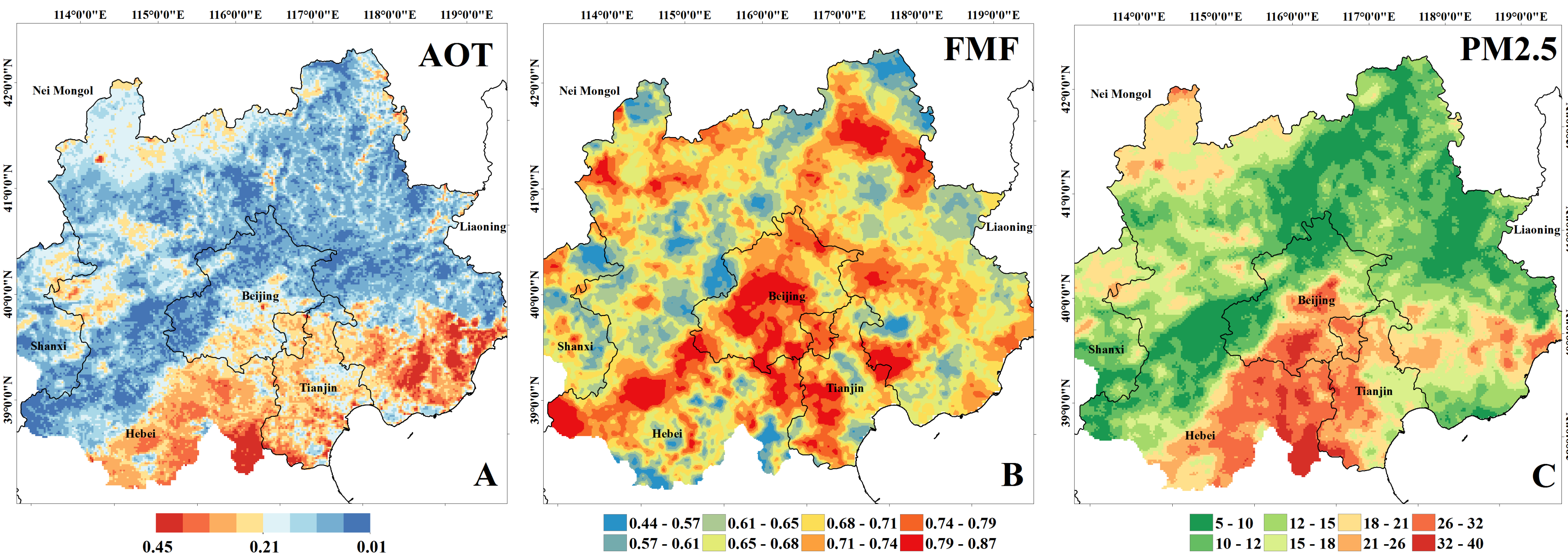

Figure 5.8: Extend the PM2.5 retrieval to large areas (PM2.5 unit: $\mu g/m^3$)

Figure 5.9A shows the mean values of PM2.5 for satellite retrieved and ground-based measurements from December 2013 to June 2015. High-level PM2.5 in the southern urban area can be clearly seen where the concentration is 42-44 μg/m^3 for satellite retrieval and 42-48 μg/m^3 for ground-based measurements. In contrast, the level of PM2.5 is much lower in the north and west of Beijing where the population is sparser and vehicle is less in these rural areas. From Figure 5.9A, a good agreement is found between the satellite retrieval and in situ measurements, and the spatial distribution of derived PM2.5 is similar to previous study by Li et al. (2015). Figure 5.9B presents the validation results of derived PM2.5 with in situ PM2.5. A total of 921 in situ measurements were collected. The dotted red lines are the estimated error envelope line $\pm 0.4 \cdot PM2.5_{in\,situ}$ and the 1:1 line, respectively. Linear regression shows a slope 0.67 and an intercept 9.5 with coefficient of determination R^2 = 0.67 (N = 921), root mean square error (RMSE) is 18.9 μg/m^3. From the result of validation, it can be found that derived PM2.5 well matches in situ observations, indicating that the retrieval model achieves a good performance.

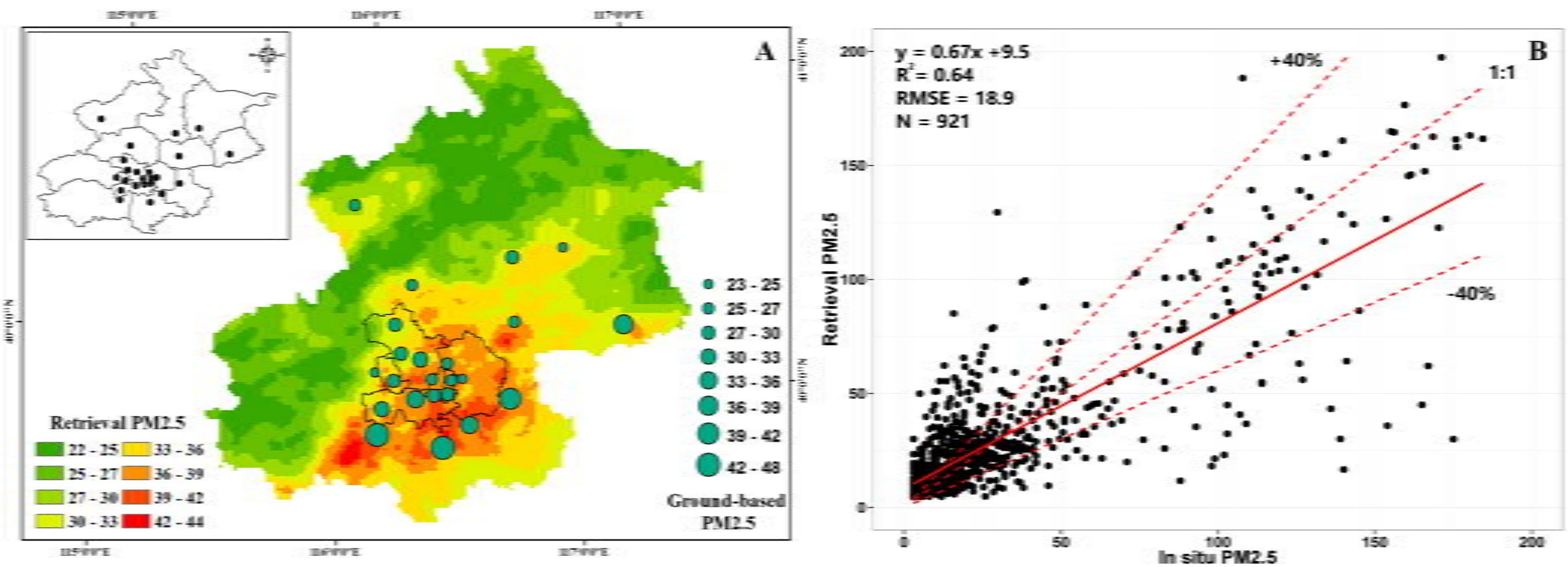

Figure 5.9: Mean PM2.5 in this study period (A) and validation (B), unit: μg/m^3

5.3.5 Discussion

In this study, we found that FM-AOT may have a better correlation with ground-level PM2.5 concentration than the total AOT's. However, it requests PBLH and RH information to correct the data from the space to the ground. If we do not have PBLH and RH information, it is fine to use total AOT to estimate PM2.5. As for haze days, since the aerosol properties have obvious differences with normal days' (Yan et al., 2016) and its relationship with PBLH and RH is not clear (Lv et al., 2013), we suggest using FM-AOT to retrieval ground-level PM2.5 without PBLH and RH correction. From the FMF comparison between MODIS, LUT-SDA and AERONET, the MODIS FMF is observed with a great uncertainty and a lot of data are not available. Because of this issue, Zhang and Li (2015) also mentioned that the mean absolute error of the PM2.5 retrieval is 64 μg/m^3 by using MODIS FMF which seems large. One possible reason is that the relationship between VE_f and FMF is based on AERONET inversion method data for Equation 5.1, however, the FMF from MODIS C6 product is derived by different method and has different definition. It could exist huge uncertainties for VE_f calculation by MODIS C6 FMF instead of AERONET FMF. Therefore, this can be a huge limitation for Equation 5.1 and Equation 5.2 application. To alleviate this problem, we used LUT-SDA FMF in this study, which is more reliable and accuracy as showed in Figure 5.9. For another hand, a constant density assumption seems not suitable for the real time PM2.5 estimation due to distinct diurnal and seasonal variations (Liu et al., 2015). Hoff and Christopher (2009) suggested that satellite AOT should combine with ground-based measurement to improve PM estimation from space. Therefore, assistant by ground-based data, the intraday pseudo density is calculated for each satellite image. By these means, the derived PM2.5 has a good performance with RMSE 18.9 μg/m^3.

5.4 Summary

This chapter presents a ground-level PM2.5 retrieval model based on fine mode AOT (FM-AOT), which incorporates SARA, LUT-SDA and the PM2.5 remote sensing method. In comparison, the meteorological factor can improve correlation between FM-AOT with surface PM2.5 (R^2 increased from 0.35 to 0.46, r increased from 0.6 to 0.68) larger than total AOT (R^2 increased from 0.43 to 0.45, r increased from 0.66 to 0.67). And the LUT-SDA FMF is found to be more available and accurate than the MODIS FMF. In order to improve the estimation accuracy, this chapter proposed a pseudo density for PM2.5 retrieval aided by the real time visibility data. Finally, the developed model was applied to retrieval surface PM2.5 over Beijing from December 2013 to June 2015 in cloud free day. The derived results were compared with the ground-based values with $R^2 = 0.64$ and RMSE $= 18.9$ μg/m^3 ($N = 921$). This validation shows that the model exhibits a good performance with a high accuracy.

Chapter 6

Conclusion

In summary, monitoring the spatial distribution of particles is of significant importance to the assessment of public health and the control of environmental population. Therefore, this thesis comprehensively describes the different retrieval algorithms of suspended particulate matters ranging from large to small sizes, including dustfall, haze aerosol, fine-mode aerosol and PM2.5.

6.1 Concluding summary

(1) Dustfall is found having a significant impact on leaf spectral features, especially in the near-infrared band (780-1300 nm), where dusty leaves have lower reflectance values than clean leaves. Specifically, r(865) and r(1240) are most closely related to dustfall, with the correlation coefficients reaching -0.48 and -0.47, respectively. Through a BP neural network model, Beijing city's dustfall distribution was estimated. The results revealed that dustfall easily accumulated and increased in the south of the city. The concentrations of dustfall in the city conformed more to the circular zonation pattern. The validation of the results showed a satisfactory perfor-

mance compared with the actual sampling bottles dustfall weight (RMSE = 3.6 g/m^2). Using dustfall images, two main sources of dustfall were found: construction sites and low-rise building with old and inappropriate land use, which corroborates earlier observations (Tsang, 1996; Weng and Yang, 2006). This study illustrates that using remote sensing to detect dustfall can be an effective and appropriate method of monitoring air pollution levels.

(2) The EHARA is developed to retrieve haze aerosol and compare the outcomes with the latest MODIS C6 aerosol products. Based on 12 years of AERONET data, it was proposed empirical SSA and AF values for haze aerosol retrieval: 0.9 (SSA) and 0.71 (AF) for the blue band, and 0.92 (SSA) and 0.67 (AF) for the red band. Comparison with ground-based AERONET data showed that EHARA-derived AOT had a fine spatial resolution of 1-km and a high level of accuracy (73% within error range and 3.4% missed value), which is higher than MODIS C6 DT 10-km (66% within error range and 43% missed value) and 3-km (53% within error range and 38% missed value) aerosol products. In this study, the C6 DB also has a good performance under haze or normal weather days (68% within error range and 9% missed value). The main reasons for the high accuracy of the EHARA are thought to be the use of real time AERONET data to determine the aerosol model (SSA and AF values) and the differences in assumptions regarding surface reflectance. Additionally, because of its haze detection, the EHARA can assign an appropriate aerosol model for haze pixels, and successfully retrieve more AOT values on hazy days. This thesis also discussed the differences between the EHARA and MODIS C6 DT land algorithm in detail. The main limitations for the MODIS C6 DT aerosol products are related to null data and negative AOT values. This study offers a fast and effective method

for investigating aerosol spatial distributions at large scales, especially for haze aerosol monitoring. Environmental authorities can use this method for aerosol distribution mapping and air quality assessment in large areas.

(3) An FMF retrieval algorithm for fine mode aerosol is proposed in this thesis. The successful use of the LUT-SDA applied to MODIS data not only verified the application of this method to the urban scale (Beijing), but verified its expansion to large areas. The retrieved FMF images were able to represent the spatial distribution of the fine aerosol contribution to the total AOT with complex surface types. The ground-based LUT-SDA validation demonstrated a high level of accuracy compared with AERONET measurements. In comparison with the C6 MOD04 DT FMF product, the LUT-SDA FMF had better spatial coverage and there was no extreme value 0, which seems more reasonable. Using the LUT-SDA, the seasonal average FMF in Beijing had a clear seasonal pattern, where the FMF was highest in summer and lowest in spring. This result was in good agreement with the phenomenon obtained by AERONET. This study shows that the LUT-SDA can be used as an effective and appropriate method to derive the FMF using MODIS. In addition, the LUT-SDA provides an alternative solution for the estimation of PM2.5 when FMF is used as a parameter, and can be further modified and applied to other satellite images (e.g., Landsat or the National Polar-orbiting Partnership (NPP)/Joint Polar Satellite System (JPSS) satellites).

(4) A ground-level PM2.5 retrieval model is developed by MODIS satellite instrument and FM-AOT. This model includes LUT-SDA, SARA and the PM2.5 remote sensing method, which is examined by the surface PM2.5 over Beijing from December 2013 to June 2015. Compared with AERONET

data, the LUT-SDA FMF was found to be more reliable and accurate than MODIS FMF. Then, a pseudo density was proposed for improving PM2.5 estimation based on real time visibility data. The pseudo density of PM2.5 showed a significant variation (standard deviation is 0.62). The PM2.5 retrieval model exhibits a good performance with $R^2 = 0.64$ and RMSE = $18.9\ \mu g/m^3$ (N = 921).

6.2 Main contributions

Main contributions of this thesis comprise four parts, being located in Chapter 2 to Chapter 5, which apply MODIS imagery for different sizes of suspended particulate matter retrieval.

(i) Dustfall Retrieval: Since the spectral information of the dustfall is very difficult to gain, there are few studies that retrieve the spatial distribution of dustfall based on satellites. Chapter 2 proposed the concept of "Clean Day"and extracted the spectral features of the dustfall through the comparison of the "Dust Day"remote sensing data. Furthermore, a neural network was built by the ground-measured spectrum of the dustfall to improve the retrieval accuracy.

(ii) Haze aerosol: There is a significant difference in properties between the haze aerosol and the normal aerosol, which makes the traditional methods inapplicable to the aerosol retrieval in haze weather. In order to solve this issue, Chapter 3 extracted the haze pixels by the thresholds of the haze and integrated the measured data of the haze aerosol properties to improve the accuracy.

(iii) Fine mode aerosol: So far it is still a challenging to compute the fine-mode aerosol based on satellites due to the difficult acquisition of the FMF. Although the traditional SDA can calculate the FMF precisely, it needs multiple bands of AOT. Therefore, it is very difficult to apply SDA to the satellite images. Chapter 4 proposed a LUT-SDA, which used only two bands of AOT to calculate the FMF. This improvement can make the SDA applicable to the satellites and get a whole spatial scale of FMF.

(iv) PM2.5: The traditional method to retrieve the ground PM2.5 based on remote sensing is to build the relationship between the total AOT and PM2.5; however, it is widely known that PM2.5 is mainly contributed by the fine mode particles. Thus, retrieving the FMF of the total AOT is of significant importance to the PM2.5 retrieval. Chapter 5 presented a new model of PM2.5 based on the fine mode aerosol and improved the model accuracy by the aid of the real-time ground-measured pseudo density of PM2.5 and WRF data.

Appendix A

A.1 AE derivative bias error correction

O'Neill et al. (2003) proposed AE derivative bias error correction in SDA. This study used the same method to correct AE derivative which is calculated by LUT-SDA. The method is as below:

$$\alpha'_{error} = 0.65 \times exp[-(\eta^1 - 0.78)^2/(2 \times 0.18^2)] \tag{A.1}$$

Where η^1 is uncorrected estimate of η as showed in Equation 4.13. Then:

$$\alpha'_{corrected} = \alpha'^1 + \alpha'_{error} \tag{A.2}$$

$$t_{corrected} = \alpha - \alpha_c - \frac{\alpha'_{corrected} - \alpha_c{}'}{\alpha - \alpha_c} \tag{A.3}$$

$$\mathrm{D_{corrected}} = \sqrt{(\mathrm{t_{corrected}} + \mathrm{b}*)^2 + 4(1 - \mathrm{a})\mathrm{c}*} \tag{A.4}$$

$$\alpha_{f_{\mathrm{corrected}}} = \frac{1}{2(1 - \mathrm{a})}(\mathrm{t_{corrected}} + \mathrm{b}* + \mathrm{D_{corrected}}) + \alpha_c \tag{A.5}$$

$$\eta_{\mathrm{corrected}} = \frac{\alpha - \alpha_c}{\alpha_{f_{\mathrm{corrected}}} - \alpha_c} \tag{A.6}$$

A.2 Mean of extreme (MOE) modification

The error of α_f can be expressed as:

$$\Delta\alpha_{\mathrm{f}}^{2} = \left(\mathrm{k}_1\frac{\partial\alpha_{\mathrm{f}}}{\partial\alpha'} + \mathrm{k}_2\frac{\partial\alpha_{\mathrm{f}}}{\partial\alpha}\right)^2\left(\frac{\Delta\tau_{\mathrm{a}}}{\tau_{\mathrm{a}}}\right)^2 + \left(\frac{\partial\alpha_{\mathrm{f}}}{\partial\mathrm{a}}\Delta\mathrm{a}\right)^2 + \left(\frac{\partial\alpha_{\mathrm{f}}}{\partial\mathrm{b}}\Delta\mathrm{b}\right)^2 + \left(\frac{\partial\alpha_{\mathrm{f}}}{\partial\mathrm{c}}\Delta\mathrm{c}\right)^2 + \left(\frac{\partial\alpha_{\mathrm{f}}}{\partial\alpha'_{\mathrm{c}}}\Delta\alpha'_{\mathrm{c}}\right)^2 + \left(\frac{\partial\alpha_{\mathrm{f}}}{\partial\alpha_{\mathrm{c}}}\Delta\alpha_{\mathrm{c}}\right)^2 \tag{A.7}$$

Where $\mathrm{k}_1 = 10$, $\mathrm{k}_2 = -2.5$, $\Delta\tau_{\mathrm{a}}$ is nominal RMS error of AOT at the reference wavelength, τ_{a} is AOT at the reference wavelength, $\Delta\alpha'_{\mathrm{c}} = 0.15$, $\Delta\alpha_{\mathrm{c}} = 0.15$, $\Delta\mathrm{a} = (\mathrm{a_{upper}} - \mathrm{a_{lower}})/2$, $\Delta\mathrm{b} = (\mathrm{b_{upper}} - \mathrm{b_{lower}})/2$, $\Delta\mathrm{c} = (\mathrm{c_{upper}} - \mathrm{c_{lower}})/2$. And:

$$\frac{\partial\alpha_f}{\partial\alpha'} = \frac{-1}{\eta_{corrected}\mathrm{D}_{corrected}} \tag{A.8}$$

$$\frac{\partial\alpha_f}{\partial\alpha} = \frac{\mathrm{t}_+}{\eta_{corrected}\mathrm{D}_{corrected}} \tag{A.9}$$

$$\mathrm{t}_+ = \alpha - \alpha_c - \frac{\alpha'_{corrected} - \alpha_c{}'}{\alpha - \alpha_c} \tag{A.10}$$

$$\frac{\partial\alpha_f}{\partial\mathrm{a}} = \frac{(\alpha_{f_{corrected}} - \alpha_{\mathrm{c}})}{(1-\mathrm{a})} + \frac{1}{\mathrm{D}_{corrected}}\left(\alpha_{\mathrm{c}}(2\alpha_{f_{corrected}} - \alpha_{\mathrm{c}}) - \frac{\mathrm{c}*}{(1-\mathrm{a})}\right) \tag{A.11}$$

$$\frac{\partial\alpha_f}{\partial\mathrm{b}} = \frac{\alpha_{f_{corrected}}}{\mathrm{D}_{corrected}} \tag{A.12}$$

$$\frac{\partial\alpha_f}{\partial\mathrm{c}} = \frac{1}{\mathrm{D}_{corrected}} \tag{A.13}$$

$$\frac{\partial\alpha_f}{\partial\alpha'_{\mathrm{c}}} = \frac{1}{\mathrm{D}_{corrected}}\left(\frac{1}{\eta_{corrected}} - 1\right) \tag{A.14}$$

$$\frac{\partial \alpha_f}{\partial \alpha_{\mathrm{c}}} = \frac{\mathrm{t}_{corrected}}{\mathrm{D}_{corrected}}(\frac{1}{\eta_{corrected}} - 1) \tag{A.15}$$

Thus, $\Delta\alpha_f$ can be computed as:

$$\Delta\alpha_f = \sqrt{\Delta{\alpha_f}^2} \tag{A.16}$$

Then, set the theoretical max of α_f is:

$$\alpha_{\mathrm{f}MAX} = min(4, 10^{(0.18*log10(\lambda)+0.57)}) \tag{A.17}$$

If $\alpha_{f_{corrected}} + \Delta\alpha_f > \alpha_{f\,MAX}$, $\alpha_{f_{corrected}} + \Delta\alpha_f = \alpha_{f\,MAX}$.
If $\alpha_{f_{corrected}} - \Delta\alpha_f > \alpha_{f\,MAX}$, $\alpha_{f_{corrected}} - \Delta\alpha_f = \alpha_{f\,MAX}$.

Finally, η correction can be as follow procedures:

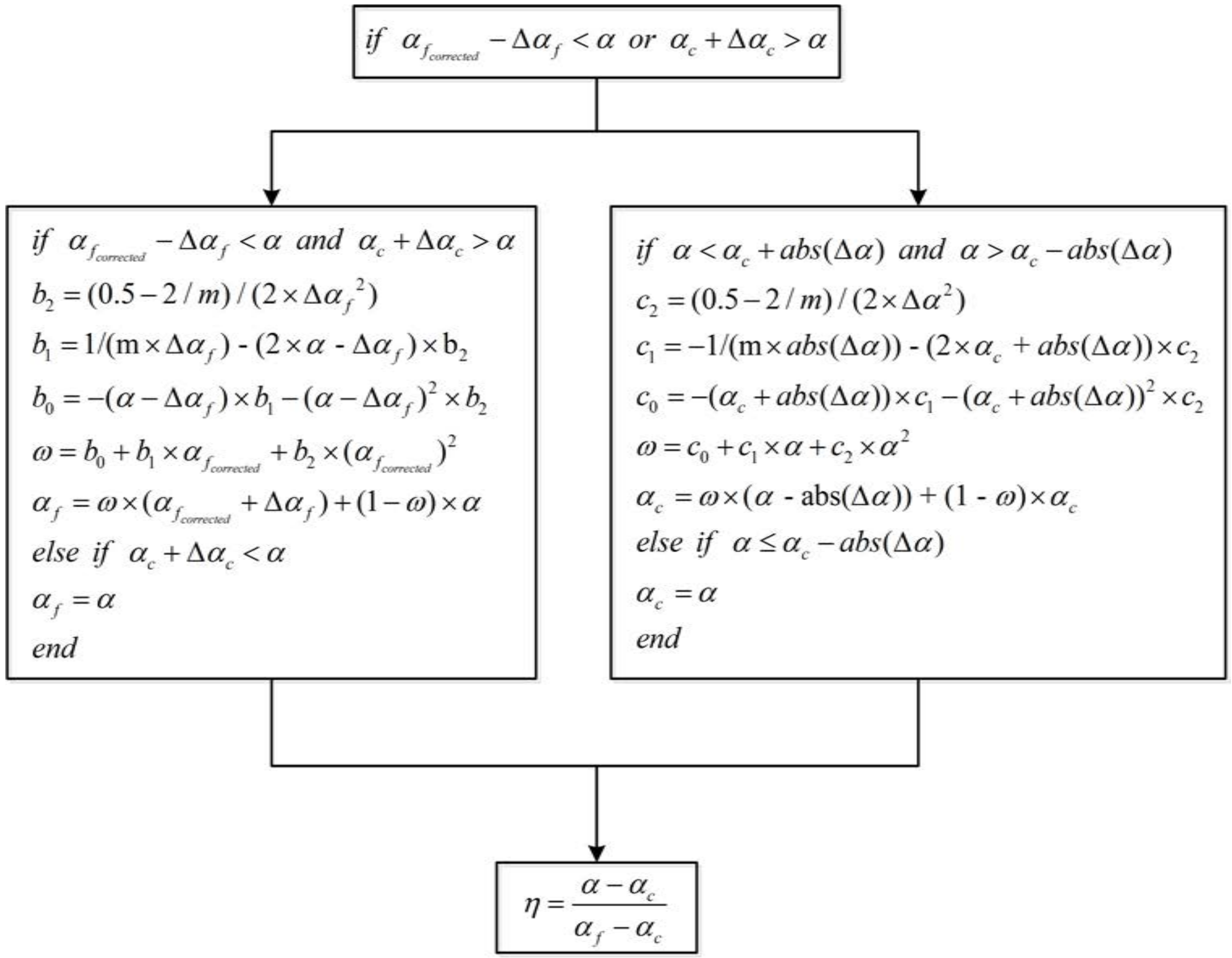

Figure A.1: FMF correction

Where $m = 8$, $\Delta\alpha = \mathrm{k}_2 \frac{\Delta\tau_\mathrm{a}}{\tau_\mathrm{a}}$.

References

Anderson, J. O., J. G. Thundiyil, and A. Stolbach (2012). "Clearing the air: a review of the effects of particulate matter air pollution on human health". *Journal of Medical Toxicology Official Journal of the American College of Medical Toxicology* 8 (8), pp. 166–75.

Antoine, D. and A. Morel (1998). "Relative importance of multiple scattering by air molecules and aerosols in forming the atmospheric path radiance in the visible and near-infrared parts of the spectrum". *Applied Optics* 37 (12), pp. 2245–2259.

Bell, M. L., K Ebisu, and R. D. Peng (2011). "Community-level spatial heterogeneity of chemical constituent levels of fine particulates and implications for epidemiological research". *Journal of Exposure Science and Environmental Epidemiology* 21 (4), pp. 372–84.

Bellouin, N. et al. (2005). "Global estimate of aerosol direct radiative forcing from satellite measurements". *Nature* 438 (7071), pp. 1138–1141.

Bergin, M. et al. (2001). "Aerosol radiative, physical, and chemical properties in Beijing during June 1999". *Journal of Geophysical Research: Atmospheres* 106 (D16), pp. 17969–17980.

Bilal, M., J. E. Nichol, and P. W. Chan (2014). "Validation and accuracy assessment of a Simplified Aerosol Retrieval Algorithm (SARA) over Beijing under low and high aerosol loadings and dust storms". *Remote Sensing of Environment* 153, pp. 50–60.

Bilal, M. et al. (2013). "A Simplified high resolution MODIS Aerosol Retrieval Algorithm (SARA) for use over mixed surfaces". *Remote Sensing of Environment* 136, pp. 135–145.

Boyouk, N. et al. (2010). "Impact of the mixing boundary layer on the relationship between PM2. 5 and aerosol optical thickness". *Atmospheric Environment* 44 (2), pp. 271–277.

Brook, R. D. et al. (2010). "Particulate matter air pollution and cardiovascular disease: An update to the scientific statement from the American Heart Association". *Circulation* 121 (21), pp. 2331–2378.

Cao, J.-J. et al. (2012). "Winter and summer PM2. 5 chemical compositions in fourteen Chinese cities". *Journal of the Air & Waste Management Association* 62 (10), pp. 1214–1226.

Che, H. et al. (2009). "Haze trends over the capital cities of 31 provinces in China, 1981–2005". *Theoretical and Applied Climatology* 97 (3-4), pp. 235–242.

Chen, Y. et al. (2015). "Characteristics and Parameterization for Atmospheric Extinction Coefficient in Beijing". *Environmental Science* 36 (10), pp. 3582–3589.

Chu, D. A. et al. (2003). "Global monitoring of air pollution over land from the Earth Observing System-Terra Moderate Resolution Imaging Spectroradiometer (MODIS)". *Journal of Geophysical Research: Atmospheres* 108 (D21).

Chudnovsky, A. and E. Ben-Dor (2008). "Application of visible, near-infrared, and short-wave infrared (400–2500 nm) reflectance spectroscopy in quantitatively assessing settled dust in the indoor environment. Case study in dwellings and office environments". *Science of the total environment* 393 (2), pp. 198–213.

Chudnovsky, A., E. Ben-Dor, and H. Saaroni (2007). "Reflectance spectroscopy of indoor settled dust in Tel Aviv, Israel: comparison between the spring and the summer seasons". *Advances in Geosciences* 12, pp. 51–57.

Chudnovsky, A. A. et al. (2013). "Spatial scales of pollution from variable resolution satellite imaging". *Environmental Pollution* 172, pp. 131–138.

Chudnovsky, A. A. et al. (2014). "Fine particulate matter predictions using high resolution Aerosol Optical Depth (AOD) retrievals". *Atmospheric Environment* 89, pp. 189–198.

Di Nicolantonio, W. et al. (2007). "MODIS aerosol optical properties over North Italy for estimating surface-level PM2.5". *Proceedings of Envisat Symposium*, pp. 3–27.

Diner, D. J. et al. (2005). "Using angular and spectral shape similarity constraints to improve MISR aerosol and surface retrievals over land". *Remote Sensing of Environment* 94 (2), pp. 155–171.

Drury, E. et al. (2008). "Improved algorithm for MODIS satellite retrievals of aerosol optical depths over western North America". *Journal of Geophysical Research: Atmospheres* 113 (D16).

Eeftens, M. et al. (2012). "Development of land use regression models for PM2. 5, PM2. 5 absorbance, PM10 and PMcoarse in 20 European study areas; results of the ESCAPE project". *Environmental Science & Technology* 46 (20), pp. 11195–11205.

Engel-Cox, J. A. et al. (2004). "Qualitative and quantitative evaluation of MODIS satellite sensor data for regional and urban scale air quality". *Atmospheric Environment* 38 (16), pp. 2495–2509.

Gao, J. et al. (2007). "Inter-comparison of WPS-TEOM-MOUDI and investigation on particle density". *Environmental Science* 28 (9), pp. 1929–1934.

Gassó, S. and N. O'Neill (2006). "Comparisons of remote sensing retrievals and in situ measurements of aerosol fine mode fraction during ACE-Asia". *Geophysical Research Letters* 33 (5), pp. 151–162.

Ghulam, A. et al. (2008). "Estimating crop water stress with ETM+ NIR and SWIR data". *Agricultural and Forest Meteorology* 148 (11), pp. 1679–1695.

Grgurić, S. et al. (2014). "Relationship between MODIS based aerosol optical depth and PM10 over Croatia". *Open Geosciences* 6 (1), pp. 2–16.

Guo, Y. et al. (2012). "Spatial distributions and temporal variations of atmospheric aerosols and the affecting factors: a case study for a region in central China". *International journal of remote sensing* 33 (12), pp. 3672–3692.

Guo, Y. et al. (2014). "Satellite remote sensing of fine particulate matter (PM2.5) air quality over Beijing using MODIS". *International Journal of Remote Sensing* 35 (17), pp. 6522–6544.

Gupta, P. and S. A. Christopher (2009). “Particulate matter air quality assessment using integrated surface, satellite, and meteorological products: Multiple regression approach”. *Journal of Geophysical Research: Atmospheres* 114 (D14).

Gupta, P. et al. (2006). “Satellite remote sensing of particulate matter and air quality assessment over global cities”. *Atmospheric Environment* 40 (30), pp. 5880–5892.

Haboudane, D. et al. (2004). “Hyperspectral vegetation indices and novel algorithms for predicting green LAI of crop canopies: Modeling and validation in the context of precision agriculture”. *Remote Sensing of Environment* 90 (3), pp. 337–352.

Han, L. et al. (2013). “An enhanced dust index for Asian dust detection with MODIS images”. *International Journal of Remote Sensing* 34 (19), pp. 6484–6495.

Han, Y. et al. (2015). “Impacts of elevated-aerosol-layer and aerosol type on the correlation of AOD and particulate matter with ground-based and satellite measurements in Nanjing, southeast China”. *Science of The Total Environment* 532, pp. 195–207.

Hansen, P. and J. Schjoerring (2003). “Reflectance measurement of canopy biomass and nitrogen status in wheat crops using normalized difference vegetation indices and partial least squares regression”. *Remote Sensing of Environment* 86 (4), pp. 542–553.

Hasekamp, O. P. and J. Landgraf (2007). “Retrieval of aerosol properties over land surfaces: capabilities of multiple-viewing-angle intensity and polarization measurements”. *Applied Optics* 46 (16), pp. 3332–3344.

Hauser, A. et al. (2005). “NOAA AVHRR derived aerosol optical depth over land”. *Journal of Geophysical Research: Atmospheres* 110 (D8).

Hoek, G. et al. (2010). “Concentration response functions for ultrafine particles and all-cause mortality and hospital admissions: results of a European expert panel elicitation”. *Environmental Science & Technology* 44 (1), pp. 476–482.

Hoff, R. M. and S. A. Christopher (2009). “Remote sensing of particulate pollution from space: have we reached the promised land?” *Journal of the Air & Waste Management Association* 59 (6), pp. 645–675.

Holben, B. et al. (2001). "An emerging ground-based aerosol climatology: Aerosol optical depth from AERONET". *Journal of Geophysical Research: Atmospheres* 106 (D11), pp. 12067–12097.

Hsu, N. et al. (2013). "Enhanced Deep Blue aerosol retrieval algorithm: The second generation". *Journal of Geophysical Research: Atmospheres* 118 (16), pp. 9296–9315.

Huang, K. et al. (2011a). "Typical types and formation mechanisms of haze in an Eastern Asia megacity, Shanghai". *Atmospheric Chemistry & Physics Discussions* 12 (1), pp. 105–124.

Huang, L. et al. (2011b). "Chemical characteristics and source apportionment of PM 10 during a brown haze episode in Harbin, China". *Particuology* 9 (1), pp. 32–38.

Hyer, E. J., J. S. Reid, and J. Zhang (2011). "An over-land aerosol optical depth data set for data assimilation by filtering, correction, and aggregation of MODIS Collection 5 optical depth retrievals". *Atmospheric Measurement Techniques* 4 (3), pp. 379–408.

Itai, K. et al. (2013). "Long- and short-term exposure to PM2.5 and mortality: using novel exposure models". *Epidemiology* 24 (4), pp. 555–61.

Jerrett, M. et al. (2005). "A review and evaluation of intraurban air pollution exposure models". *Journal of Exposure Science and Environmental Epidemiology* 15 (2), pp. 185–204.

Jethva, H. et al. (2010). "Improved retrieval of aerosol size-resolved properties from moderate resolution imaging spectroradiometer over India: Role of aerosol model and surface reflectance". *Journal of Geophysical Research: Atmospheres* 115 (D18).

Kaufman, Y. et al. (1997). "Passive remote sensing of tropospheric aerosol and atmospheric correction for the aerosol effect". *Journal of Geophysical Research: Atmospheres* 102 (D14).

Kloog, I. et al. (2015). "Estimating daily PM 2.5 and PM 10 across the complex geo-climate region of Israel using MAIAC satellite-based AOD data". *Atmospheric Environment* 122, pp. 409–416.

Kokhanovsky, A. et al. (2009). "Determination of particulate matter vertical columns using satellite observations". *Atmospheric Measurement Techniques* 2 (2), pp. 327–335.

Kokhanovsky, A. et al. (2010). "The inter-comparison of major satellite aerosol retrieval algorithms using simulated intensity and polarization characteristics of reflected light". *Atmospheric Measurement Techniques* 3 (4), pp. 909–932.

Lee, H. et al. (2011). "A novel calibration approach of MODIS AOD data to predict PM 2.5 concentrations". *Atmospheric Chemistry and Physics Discussions* 11 (3), pp. 9769–9795.

Lee, H. J. et al. (2012). "Use of satellite-based aerosol optical depth and spatial clustering to predict ambient PM 2.5 concentrations". *Environmental Research* 118, pp. 8–15.

Lee, K. H., Y. J. Kim, and M. J. Kim (2006). "Characteristics of aerosol observed during two severe haze events over Korea in June and October 2004". *Atmospheric Environment* 40 (27), pp. 5146–5155.

Lee, K. H. et al. (2006). "Influence of land surface effects on MODIS aerosol retrieval using the BAER method over Korea". *International Journal of Remote Sensing* 27 (22), pp. 5125–5125.

Lee, K. and C. E. Chung (2013). "Observationally-constrained estimates of global fine-mode AOD". *Atmospheric Chemistry and Physics* 13 (5), pp. 2907–2921.

Leung, Y.-k., M.-c. Wu, and K.-k. Yeung (2009). "A Study on the Relationship among Visibility, Atmospheric Suspended Particulate Concentration, and Meteorological Conditions in Hong Kong". *Journal of Meteorological Research* 23 (2), pp. 250–260.

Levy, R. C. et al. (2007). "Second-generation operational algorithm: Retrieval of aerosol properties over land from inversion of Moderate Resolution Imaging Spectroradiometer spectral reflectance". *Journal of Geophysical Research: Atmospheres* 112 (D13).

Levy, R. C. et al. (2010). "Global evaluation of the Collection 5 MODIS dark-target aerosol products over land". *Atmospheric Chemistry and Physics* 10 (21), pp. 10399–10420.

Levy, R. C. et al. (2013). "The Collection 6 MODIS aerosol products over land and ocean". *Atmospheric Measurement Techniques* 6 (11), pp. 2989–3034.

Li, C. et al. (2005). "Retrieval, validation, and application of the 1-km aerosol optical depth from MODIS measurements over Hong Kong". *IEEE Transactions on Geoscience and Remote Sensing* 43 (11), pp. 2650–2658.

Li, R. et al. (2015). "Estimating Ground-Level PM 2.5 Using Fine-Resolution Satellite Data in the Megacity of Beijing, China". *Aerosol and Air Quality Research* 15 (4), pp. 1347–1356.

Li, S. et al. (2013). "Retrieval of the haze optical thickness in North China Plain using MODIS data". *IEEE Transactions on Geoscience and Remote Sensing* 51 (5), pp. 2528–2540.

Li, Z. et al. (2016). "Remote sensing of atmospheric particulate mass of dry PM 2.5 near the ground: Method validation using ground-based measurements". *Remote Sensing of Environment* 173, pp. 59–68.

Liang, S., B. Zhong, and H. Fang (2006). "Improved estimation of aerosol optical depth from MODIS imagery over land surfaces". *Remote Sensing of Environment* 104 (4), pp. 416–425.

Likuku, A. S., G. K. Gaboutloeloe, and K. B. Mmolawa (2013). "Determination and source apportionment of selected heavy metals in aerosol samples collected from Sebele". *American Journal of Environmental Sciences* 9 (2), p. 188.

Lin, C. et al. (2015). "Using satellite remote sensing data to estimate the high-resolution distribution of ground-level PM 2.5". *Remote Sensing of Environment* 156, pp. 117–128.

Liu, C. and G. Liu (2009). "Aerosol optical depth retrieval for SPOT HRV images". *Journal of Marine Science and Technology* 17 (4), pp. 300–305.

Liu, Y., C. J. Paciorek, and P. Koutrakis (2009). "Estimating Regional Spatial and Temporal Variability of PM2. 5 Concentrations Using Satellite Data, Meteorology, and Land Use Information". *Environmental Health Perspectives* 117 (6), p. 887.

Liu, Y. et al. (2011). "The effect of aerosol vertical profiles on satellite-estimated surface particle sulfate concentrations". *Remote Sensing of Environment* 115 (2), pp. 508–513.

Liu, Z. et al. (2015). "Diurnal and seasonal variation of the PM 2.5 apparent particle density in Beijing, China". *Atmospheric Environment* 120, pp. 328–338.

Lu, S., Y. Zheng, and S. Bai (2008). “A HRTEM/EDX approach to identification of the source of dust particles on urban tree leaves”. *Atmospheric Environment* 42 (26), pp. 6431–6441.

Lue, Y. et al. (2010). “Characteristics and provenance of dustfall during an unusual floating dust event”. *Atmospheric Environment* 44 (29), pp. 3477–3484.

Luo, N., W. Zhao, and X. Yan (2014). “Integrated aerosol optical thickness, gaseous pollutants and meteorological parameters to estimate ground PM2.5 concentration”. *Fresenius Environmental Bulletin* 23 (10A), pp. 2567–2577.

Luo, N. et al. (2015). “Improved aerosol retrieval algorithm using Landsat images and its application for PM 10 monitoring over urban areas”. *Atmospheric Research* 153, pp. 264–275.

Luo, N., W. Zhao, and X. Yan (2013). “Impact of Dust-Fall on Spectral Features of Plant Leaves”. *Spectroscopy and Spectral Analysis* 33 (10), pp. 2715–2720.

Lv, Y. et al. (2013). “Joint use of ground-based Lidar and sun-sky radiometer for observation of aerosol vertical distribution”. *Journal of Remote Sensing* 17 (4), pp. 1008–1020.

Ma, Z. et al. (2014). “Estimating ground-level PM2.5 in China using satellite remote sensing”. *Environmental Science & Technology* 48 (13), pp. 7436–7444.

Mao, J. and C. Li (2006). “Observation Study of Aerosol Radiative Properities over China”. *Acta Meteorologica Sinica* 20 (3), pp. 306–321.

Mielonen, T. et al. (2011). “Evaluating the assumptions of surface reflectance and aerosol type selection within the MODIS aerosol retrieval over land: the problem of dust type selection”. *Atmospheric Measurement Techniques* 4 (2), pp. 201–214.

Mishchenko, M. I. and I. V. Geogdzhayev (2007). “Satellite remote sensing reveals regional tropospheric aerosol trends”. *Optics Express* 15 (12), pp. 7423–7438.

Munchak, L. A. et al. (2013). “MODIS 3 km aerosol product: applications over land in an urban/suburban region”. *Atmospheric Measurement Techniques* 6 (7), pp. 1747–1759.

Noh, Y. M. et al. (2009). "Optical and microphysical properties of severe haze and smoke aerosol measured by integrated remote sensing techniques in Gwangju, Korea". *Atmospheric Environment* 43 (4), pp. 879–888.

O'Neill, N. T., O. Dubovik, and T. F. Eck (2001). "Modified Ångström exponent for the characterization of submicrometer aerosols". *Applied Optics* 40 (15), pp. 2368–2375.

O'Neill, N. et al. (2003). "Spectral discrimination of coarse and fine mode optical depth". *Journal of Geophysical Research: Atmospheres* 108 (D17).

Ong, C. et al. (2001). "Quantifying dust loading on mangroves using hyperspectral techniques". *Geoscience and Remote Sensing Symposium, 2001. IGARSS '01. IEEE 2001 International*, 296–298 vol.1.

Paciorek, C. J. et al. (2008). "Spatiotemporal associations between GOES aerosol optical depth retrievals and ground-level PM2.5". *Environmental Science & Technology* 42 (15), pp. 5800–5806.

Pal, N. R. et al. (2003). "SOFM-MLP: A hybrid neural network for atmospheric temperature prediction". *IEEE Transactions on Geoscience and Remote Sensing* 41 (12), pp. 2783–2791.

Peng, J. et al. (2013). "Quantitative model of foliar dustfall content using hyperspectral remote sensing". *Journal of Infrared & Millimeter Waves* 32 (4), pp. 313–319.

Pope III, C. A., M. Ezzati, and D. W. Dockery (2009). "Fine-particulate air pollution and life expectancy in the United States". *New England Journal of Medicine* 360 (4), pp. 376–386.

Pope III, C. A. et al. (2002). "Lung cancer, cardiopulmonary mortality, and long-term exposure to fine particulate air pollution". *JAMA* 287 (9), pp. 1132–1141.

Prusty, B., P. Mishra, and P. Azeez (2005). "Dust accumulation and leaf pigment content in vegetation near the national highway at Sambalpur, Orissa, India". *Ecotoxicology and Environmental Safety* 60 (2), pp. 228–235.

Przybysz, A et al. (2014). "Accumulation of particulate matter and trace elements on vegetation as affected by pollution level, rainfall and the passage of time". *Science of the Total Environment* 481, pp. 360–369.

Qu, W. et al. (2016). “Opposite seasonality of the aerosol optical depth and the surface particulate matter concentration over the north China Plain”. *Atmospheric Environment* 127, pp. 90–99.

Quan, J. et al. (2011). “Analysis of the formation of fog and haze in North China Plain (NCP)”. *Atmospheric Chemistry and Physics* 11 (15), pp. 8205–8214.

Rahman, H., B. Pinty, and M. M. Verstraete (1993). “Coupled surface-atmosphere reflectance (CSAR) model: 2. Semiempirical surface model usable with NOAA advanced very high resolution radiometer data”. *Journal of Geophysical Research: Atmospheres* 98 (D11).

Rai, P. K. (2013). “Environmental magnetic studies of particulates with special reference to biomagnetic monitoring using roadside plant leaves”. *Atmospheric Environment* 72, pp. 113–129.

Ram, S. et al. (2014). “Physico-chemical characterization of street dust and re-suspended dust on plant canopies: An approach for finger printing the urban environment”. *Ecological Indicators* 36, pp. 334–338.

Ramachandran, S. (2007). “Aerosol optical depth and fine mode fraction variations deduced from Moderate Resolution Imaging Spectroradiometer (MODIS) over four urban areas in India”. *Journal of Geophysical Research: Atmospheres* 112 (D16).

Remer, L. A. et al. (2013). “MODIS 3 km aerosol product: algorithm and global perspective”. *Atmospheric Measurement Techniques* 6 (7), pp. 1829–1844.

Roujean, J. L., M. Leroy, and P. Y. Deschamps (1992). “A bidirectional reflectance model of the Earth’s surface for the correction of remote sensing data”. *Journal of Geophysical Research* 97 (972), pp. 20455–20468.

Şahin, M. (2012). “Modelling of air temperature using remote sensing and artificial neural network in Turkey”. *Advances in Space Research* 50 (7), pp. 973–985.

Sayer, A. et al. (2013). “Validation and uncertainty estimates for MODIS Collection 6 Deep Blue aerosol data”. *Journal of Geophysical Research: Atmospheres* 118 (14), pp. 7864–7872.

Sayer, A. et al. (2014). "MODIS Collection 6 aerosol products: Comparison between Aqua's e-Deep Blue, Dark Target, and merged data sets, and usage recommendations". *Journal of Geophysical Research: Atmospheres* 119, pp. 13965–13989.

Schaap, M et al. (2009). "Exploring the relation between aerosol optical depth and PM 2.5 at Cabauw, the Netherlands". *Atmospheric Chemistry and Physics* 9 (3), pp. 909–925.

Shu, J. et al. (2001). "Determining the sources of atmospheric particles in Shanghai, China, from magnetic and geochemical properties". *Atmospheric Environment* 35 (15), pp. 2615–2625.

Soni, K. et al. (2011). "Wavelength dependence of the aerosol Angstrom exponent and its implications over Delhi, India". *Aerosol Science and Technology* 45 (12), pp. 1488–1498.

Sun, Y. et al. (2006). "Chemical characteristics of PM2. 5 and PM10 in haze-fog episodes in Beijing". *Environmental Science & Technology* 40 (10), pp. 3148–3155.

Tang, J. et al. (2005). "Aerosol optical thickness determination by exploiting the synergy of TERRA and AQUA MODIS". *Remote Sensing of Environment* 94 (3), pp. 327–334.

Tanré, D. et al. (1979). "Atmospheric modeling for space measurements of ground reflectances, including bidirectional properties". *Applied Optics* 18 (21), pp. 3587–3594.

Tao, M. et al. (2012). "Satellite observation of regional haze pollution over the North China Plain". *Journal of Geophysical Research: Atmospheres* 117 (D12).

Tao, M. et al. (2013). "Satellite observation of abnormal yellow haze clouds over East China during summer agricultural burning season". *Atmospheric Environment* 79, pp. 632–640.

Tao, M. et al. (2014). "Formation process of the widespread extreme haze pollution over northern China in January 2013: Implications for regional air quality and climate". *Atmospheric Environment* 98, pp. 417–425.

Tsang, F. Y. (1996). "To improve air quality through land use planning: a case study in Western District: urban planning in Hong Kong". *HKU Theses Online (HKUTO).*

Tumbo, S. D., D. G. Wagner, and P. H. Heinemann (2002). "Hyperspectral-based neural network for predicting chlorophyll status in corn". *Transactions of the ASAE* 45 (3), pp. 825–832.

Urbat, M, E Lehndorff, and L Schwark (2004). "Biomonitoring of air quality in the Cologne conurbation using pine needles as a passive samplerPart I: magnetic properties". *Atmospheric Environment* 38 (23), pp. 3781–3792.

Valipour, M, M. Banihabib, and S. Behbahani (2012). "Monthly inflow forecasting using autoregressive artificial neural network". *Journal of Applied Sciences* 12 (20), p. 2139.

Valipour, M., M. E. Banihabib, and S. M. R. Behbahani (2013). "Comparison of the ARMA, ARIMA, and the autoregressive artificial neural network models in forecasting the monthly inflow of Dez dam reservoir". *Journal of Hydrology* 476, pp. 433–441.

Van Donkelaar, A. et al. (2010). "Global estimates of ambient fine particulate matter concentrations from satellite-based aerosol optical depth: development and application". *Environmental Health Perspectives* 118 (6), p. 847.

Van Donkelaar, A. et al. (2011). "Satellite-based estimates of ground-level fine particulate matter during extreme events: A case study of the Moscow fires in 2010". *Atmospheric Environment* 45 (34), pp. 6225–6232.

Wang, J. and S. A. Christopher (2003). "Intercomparison between satellitederived aerosol optical thickness and PM2.5 mass: Implications for air quality studies". *Geophysical Research Letters* 30 (21), pp. 267–283.

Wang, J. et al. (2010a). "Improved algorithm for MODIS satellite retrievals of aerosol optical thickness over land in dusty atmosphere: Implications for air quality monitoring in China". *Remote Sensing of Environment* 114 (11), pp. 2575–2583.

Wang, T et al. (2012). "Influence of foliar dust on crop reflectance spectrum and nitrogen monitoring". *Spectroscopy and Spectral Analysis* 32 (7), pp. 1895–1898.

Wang, W. et al. (2014). "One–year aerosol characterization study for PM 2.5 and PM 10 in Beijing". *Atmospheric Pollution Research* 5 (3), pp. 554–562.

Wang, Z. et al. (2013). "Analyses on Spatial and Temporal Characteristics of AOD in Guanzhong Region of Shaanxi Province Using Long Term MODIS Data". *Plateau Meteorology* 32, pp. 234–242.

Wang, Z. et al. (2010b). “Satellite-based estimation of regional particulate matter (PM) in Beijing using vertical-and-RH correcting method”. *Remote Sensing of Environment* 114 (1), pp. 50–63.

Weng, Q. and S. Yang (2006). “Urban air pollution patterns, land use, and thermal landscape: an examination of the linkage using GIS”. *Environmental Monitoring and Assessment* 117 (1-3), pp. 463–489.

Wong, M. S., J. E. Nichol, and K. H. Lee (2011). “An operational MODIS aerosol retrieval algorithm at high spatial resolution, and its application over a complex urban region”. *Atmospheric Research* 99 (3), pp. 579–589.

Xin, J. et al. (2014). “The empirical relationship between the PM 2.5 concentration and aerosol optical depth over the background of North China from 2009 to 2011”. *Atmospheric Research* 138 (3), pp. 179–188.

Xu, X. et al. (2013). “Constraints on aerosol sources using GEOS-Chem adjoint and MODIS radiances, and evaluation with multisensor (OMI, MISR) data”. *Journal of Geophysical Research: Atmospheres* 118 (12), pp. 6396–6413.

Yan, P. et al. (2008). “The measurement of aerosol optical properties at a rural site in Northern China”. *Atmospheric Chemistry and Physics* 8 (8), pp. 2229–2242.

Yan, X. et al. (2014a). “Estimation of atmospheric dust deposition on plant leaves based on spectral features”. *Spectroscopy Letters* 47 (7), pp. 536–542.

Yan, X. et al. (2014b). “Impact of aerosols and atmospheric particles on plant leaf proteins”. *Atmospheric Environment* 88 (5), pp. 115–122.

Yan, X. et al. (2015). “Mapping dustfall distribution in urban areas using remote sensing and ground spectral data”. *Science of the Total Environment* 506, pp. 604–612.

Yan, X. et al. (2016). “A new method of satellite-based haze aerosol monitoring over the North China Plain and a comparison with MODIS Collection 6 aerosol products”. *Atmospheric Research* 171, pp. 31–40.

Yang, J. et al. (2005). “The urban forest in Beijing and its role in air pollution reduction”. *Urban Forestry & Urban Greening* 3 (2), pp. 65–78.

Yang, T. et al. (2011). “Magnetic properties of the road dusts from two parks in Wuhan city, China: implications for mapping urban environment”. *Environmental Monitoring and Assessment* 177 (1-4), pp. 637–648.

Ying, Z. et al. (2009). “Role of black carbon-induced changes in snow albedo in predictions of temperature and precipitation during a snowstorm”. *Atmospheric and Oceanic Science Letters* 2 (4), pp. 230–236.

Yu, X. et al. (2012). “Optical properties of aerosol during haze-fog episodes in Beijing”. *Environmental Science* 33 (4), pp. 1057–1062.

Zha, Y. et al. (2011). “Improved retrieval of aerosol optical thickness from MODIS measurements through derived surface reflectance over Nanjing, China”. *Tellus B* 63 (5), pp. 952–958.

Zhang, Y. and Z. Li (2013). “Estimation of PM2.5 from fine-mode aerosol optical depth”. *Journal of Remote Sensing* 17, pp. 929–943.

Zhang, Y. and Z. Li (2015). “Remote sensing of atmospheric fine particulate matter (PM 2.5) mass concentration near the ground from satellite observation”. *Remote Sensing of Environment* 160, pp. 252–262.

Zhang, Z. et al. (2014). “Analysis and comparison of the aerosol microphysical properties at three AERONET sites in China”. *China Environmental Science* 34, pp. 1927–1937.

Zhao, C. X. et al. (2014). “Temporal and Spatial Distribution of PM2.5 and PM10 Pollution Status and the Correlation of Particulate Matters and Meteorological Factors During Winter and Spring in Beijing”. *Environmental Science* 35 (2), pp. 418–27.

Zhao, P. et al. (2013). “Characteristics of concentrations and chemical compositions for PM 2.5 in the region of Beijing, Tianjin, and Hebei, China”. *Atmospheric Chemistry and Physics* 13 (9), pp. 4631–4644.

Zheng, Y. et al. (2016). “Estimating ground-level PM 2.5 concentrations over three megalopolises in China using satellite-derived aerosol optical depth measurements”. *Atmospheric Environment* 124, pp. 232–242.